Molecular Approaches to Solar Fuel Production

by

Edgar Alejandro Reyes Cruz

A Dissertation Presented in Partial Fulfillment
of the Requirements for the Degree
Doctor of Philosophy

Approved July 2023 by the
Graduate Supervisory Committee:

Gary F. Moore, Chair
Ryan J. Trovitch
Scott G. Sayres

ARIZONA STATE UNIVERSITY

August 2023

ABSTRACT

The conversion of water to hydrogen and of carbon dioxide to industrially relevant chemical precursors are examples of reactions that can be used to store renewable energy as fuels or chemical building blocks for creating sustainable chemical manufacturing cycles. Unfortunately, current industrial catalysts for these transformations are reliant on relatively expensive and/or rare materials, such as platinum in the case of hydrogen generation, or lack selectivity towards producing a desired chemical product. Such drawbacks prevent global-scale applications. Although replacing such catalysts with more efficient and earth-abundant catalysts could improve this situation, the fundamental science required for this is lacking. In the first part of this dissertation, the synthesis and characterization of a novel binuclear iron fused porphyrin designed to break traditional scaling relationships in electrocatalysis is presented. Key features of the fused porphyrin include: 1) bimetallic sites, 2) a π-extended ligand that delocalizes electrons across the multimetallic scaffold, and 3) the ability to store up to six reducing equivalents. In the second part of this thesis, the electrochemical characterization of benzimidazole-phenols as "proton wires" is described. These bioinspired assemblies model the tyrosine-histidine pair of photosystem II, which serves as a redox mediator between the light-harvesting reaction center P680 and the oxygen evolution complex that enables production of molecular oxygen from water in cyanobacteria, algae, and higher plants. Results show that as the length of the hydrogen-bond network increases across a series of benzimidazole-phenols, the midpoint potential of the phenoxyl/phenol redox couple becomes less oxidizing. However, benzimidazole-phenols containing electron-withdrawing trifluoromethyl substituents enable access to potentials that are

thermodynamically sufficient for oxidative processes relevant to artificial photosynthesis, including the oxidation of water, while translocating protons over ~11 Å.

DEDICATION

Para mi madre y mi padre,

Por ser mis ángeles aquí y allá

ACKNOWLEDGMENTS

To Prof. Gary F. Moore, for his guidance towards the completion of this dissertation, for sharing his knowledge and experience, improving my critical and analytical thinking, and inspiring me to be a better scientist and to always aim for excellence.

To Prof. Ana Moore, for giving me the very first opportunity to experience academic research 12 years ago, and then leaving the doors open to do two more summer internships. It was because of them that I decided to come to graduate school. And now during the last three years, she and Prof. Tom Moore allowed me to collaborate with their group. To Prof. Ryan Trovitch and Prof. Scott Sayres, for serving as part of my committee. Their support, encouragement, and insight has always been appreciated.

To my past and present colleagues of the GFM group: Dr. Anna Beiler, Dr. Diana Khusnutdinova, and Dr. Brain Wadsworth, Dr. Nghi Nguyen, Daiki Nishiori, and Lillian Hensleigh. Anna, Diana, and Brian welcomed me to the GFM lab, helped me so much during my first years, and taught me all the basics of how to work in this group – especially Diana as my synthetic organic chemist peer. Daiki, Nghi, and Lillian, their cheerfulness always was a great balance to my seriousness. I'm deeply grateful for the time I shared in and out of lab with every one of them, and I appreciate so much they were able to deal with my music!

To my innermost circle of friends: Dra. Marely Tejeda, necesitaría otra tesis completa

para eso agradecer su ayuda en tantas cosas. No puedo negar que es una parte elemental de la persona que soy hoy. Also, extra points for finding a very nice Steven for us to share lol. Dr. Rafael Alcalá #vvzuhky, por la infinidad de risas ayer y hoy, y por sus invaluables consejos sobre la vida y sobre research. Dr. Jake Garcia and Dr. Lauren Heald, I'm beyond happy to have walked this PhD path with you since day one, and for sharing a lot of moments, parties, beers, and talks. In-Hye Han, for being an awesome friend, for the random and last-minute plans, and for being a great concert pal even when she still doesn't want to go into the mosh pits. Maybe one point off for so many IPAs.

A mis primeros colaboradores del grupo de los Moore y que rápidamente se volvieron mis amigos: Dra. Jimena Mora, Dr. Emmanuel Odella, Dr. Walter Guerra, y Dr. Martin Faillace. To all the wonderful friends I have met during my time here and now have a permanent place in my heart: Trygve, Ryan B., Sthitadhi, Kirstie, Pritha, Sanchari, Soma, Jordyn, Jesse, John, Rose, Ryan M., Lina, Rodrigo, Edwin, Dani. A mis viejos amigos que se han mantenido a mi lado a pesar del tiempo y la distancia: Betty, Vicky, Cris, Dinorah, Karla, Adolfo, Tavo, Esteban, Kike, Miguel.

A mis tíos, primos, y sobrinos: por hacerme sentir feliz y de nuevo en casa en cada visita. No me da el espacio para nombrarlos a todos, pero cada uno es infinitamente importante para mí. Especialmente, para mis tíos que me apoyaron desde el día que empecé, estuvieron constantemente presentes en visitas o llamadas, y sin embargo no fue posible compartir este triunfo con ellos el día de hoy.

A mi madre, Amelia: por arriesgarse una vez más conmigo en otra aventura aún más larga y aún a más distancia. Por ser el principal pilar de mi vida y la persona que más amo y admiro. Sin duda uno de los mejores seres humanos que haya existido.

v

TABLE OF CONTENTS

LIST OF TABLES

LIST OF FIGURES

LIST OF ABBREVIATIONS

Abbreviation	Meaning
2DEV	Two-dimensional Electronic-vibrational
2PT	Double Proton Transfer
ATP	Adenosine Triphosphate
BIP	Benzimidazole-phenol
CE	Counter Electrode
CLS	Center Line Slope
C_3H_7CN	Butyronitrile
C_6H_5CN	Benzonitrile
CH_2Cl_2	Dichloromethane
CO_2RR	CO_2 Reduction Reaction
Cyt b_6f	Cytochrome Plastoquinol-plastocyanin-oxidoreductase
DMF	*N,N*-Dimethylformamide
$E_{1/2}$	Midpoint Potential
E1PT	One-electron, One-proton Transfer
E2PT	One-electron, Two-proton Transfer
E3PT	One-electron, Three-proton Transfer

ET	Electron Transfer
FTIR	Fourier Transform Infrared
G3P	Glyceraldehyde-3-phosphate
η	Overpotential
H_{AB}	Electronic Matrix Element
HER	Hydrogen Evolution Reaction
IR-SEC	Infrared Spectroelectrochemistry
k_B	Boltzmann Constant
k_{et}	Rate Constant for Electron Transfer
λ	Reorganization Energy
MALDI-TOF MS	Matrix-assisted Laser Desorption/Ionization Time-of-flight Mass Spectrometry
NADPH	Reduced Nicotinamide Adenine Dinucleotide Phosphate
NMR	Nuclear Magnetic Resonance
OEC	Oxygen Evolution Complex
ORR	Oxygen Reduction Reaction
PCET	Proton-coupled Electron Transfer
PIA	Photoinduced Absorptions

PMF	Proton-motive Force
PSI	Photosystem I
PSII	Photosystem II
RE	Pseudoreference Electrode
SCE	Standard Calomel Electrode
T	Temperature
TBAPF$_6$	Tetrabutylammonium Hexafluorophosphate
TPA	Terminal Proton Acceptor
UV-Vis	Ultraviolet-visible
UV-Vis-NIR-SEC	UV-Vis-near Infrared Spectroelectrochemistry
XPS	X-ray Photoelectron Spectroscopy
XANES	X-ray Absorption Near-edge Spectroscopy
WE	Working Electrode

CHAPTER 1

INTRODUCTION

Portions of this chapter are excerpted and reprinted with permission from:

Reyes Cruz, E. A.; Nishiori, D.; Wadsworth, B. L.; Nguyen, N. P.; Hensleigh, L. K.;

Khusnutdinova, D.; Beiler, A. M.; Moore, G. F. Molecular-Modified Photocathodes for

Applications in Artificial Photosynthesis and Solar-Fuel Technologies. *Chem. Rev.*, **2022**,

122 (21), 16051–16109.

and

Khusnutdinova, D.; Wadsworth, B. L.; Flores, M.; Beiler, A. M.; Reyes Cruz, E. A.;

Zenkov, Y.; Moore, G. F. Electrocatalytic Properties of Binuclear Cu(II) Fused

Porphyrins for Hydrogen Evolution. *ACS Catal.*, **2018**, *8* (10), 9888–9898.

Copyright 2018 and 2022 American Chemical Society.

1.1 Increasing Population and Greenhouse Emissions

The world's population reached 8 billion people by the end of 2022. The current projections now estimate that it will increase to 9 billion people by 2037, and then peak at 10.4 billion by mid-2080's.[1] Energy demands increase along with this growth. During 2021, 79% of the total 624×10^{18} J used in the world came from fossil fuels (coal, natural gas, and oil), while the rest came mainly from nuclear power and renewable sources (wind, solar PV, hydropower, bioenergy, geothermal, etc.).[2] At the same time, the total energy-related CO_2 emissions amounted to 36.6×10^9 tons, the largest annual increase in history. At the end of July 2023, the average concentration of CO_2 in the atmosphere was 419 ppm[3] – 50% higher than it was during the Industrial Age, 30% higher than in 1958 when scientists started measuring consistently the atmospheric CO_2, and 11% higher than in 2000. Besides these rapid increases over the last centuries and decades, it is also worth noting that the concentration of CO_2 fluctuated between 180 and 290 ppm during the last 800,000 years.[4] Additionally, it is estimated that the last time the Earth had concentrations between 300 and 400 ppm was probably during the mid-Pliocene around 3 million years ago, and the last time concentrations were consistently above 400 ppm, it was probably during the Miocene, 16 million years ago. In order to avoid the further increases in the atmospheric levels of this greenhouse gas and the concomitant environmental consequences, it is necessary to keep working on increasing the use of the aforementioned renewable sources and decrease our dependence on fossil fuels.

1.2 Renewable Energies and Technologies

The use of renewable-energy sources to produce carbon-free or neutral fuels provides a promising alternative to using conventional petroleum-based, fossil resources.

Renewable-energy sources, such as wind and solar, can easily provide the total energy demands of modern societies. For example, Earth receives approximately 120×10^{15} J every second from sunlight.[5,6] In other words, one hour and a half of sunlight would be more than the total energy used in the world in 2021. However, this energy is diluted (considering the total surface of Earth) and intermittent (the sun eventually sets). Therefore, such technologies would require the development of materials capable of efficiently storing energy so they can be distributed later at different times and places.

One promising approach is to store electrical power generated from renewable sources in the form of chemical bonds. Such processes are inspired by biological energy transduction schemes, including the process of photosynthesis that occurs in plants, where solar energy is initially converted to electrical forms of energy and then ultimately transformed to chemical forms that provide the foods and fuels for powering the planet. Such technologies, whether biological or human-engineered, ultimately require the use of materials known as catalysts, which appropriately direct the energetics and timing of the overall fuel-forming reactions.

Artificial photosynthesis applies the fundamental principles of the natural/biological process including the capture, conversion, and storage of solar energy, to develop human-engineered counterparts.[5,7-11] Natural photosynthesis is currently the largest-scale process for storing light energy in the form of chemical bonds,[12,13] but the overall solar-to-fuel conversion efficiency is limited to a few percent and its products are already appropriated for powering the biosphere.[15] Although natural photosynthesis is a product of continued evolution stemming from environmental pressures and opportunities,[14] it is not designed to satiate the material and fuel-consumption demands of modern societies.[15] Conversely,

3

if the associated technological and policy challenges can be surmounted, artificial photosynthesis offers a route to meeting global human energy demands with minimal environmental impact.[5,9,10,16-18] In this context, designing artificial photosynthetic assemblies that use "just the best bits" of the biological counterpart is a promising approach.[19,20]

1.3 Natural Photosynthesis

Nature utilizes an array of pigments to harvest solar energy including chlorophylls, bacteriochlorophylls, carotenoids, and phycobilins. These molecules can be arranged in antenna complexes, where the absorption of light triggers spatial and energetic funneling of photonic energy to chlorophyll-based reaction centers that initiate a cascade of photoinduced electron-transfer events.[21] The pigments in the antenna enable use of a larger cross section of the solar spectrum compared to what can be directly absorbed via chlorophyll-based reaction centers.[21-23] For example, in Photosystem I (PSI) (Figure 1.1), the modified chlorophyll *a* reaction center, P700, has relatively intense absorption bands in the blue (Soret bands) and red (Q bands) regions of the solar spectrum, but the surrounding antenna complex enables utilization of photons at wavelengths where the light harvesting efficiency of P700 is relatively low.[22] Although high light fluxes can result in photodamage, nature has evolved elaborate protection, regulation, and repair mechanisms.[24,25] These include the rapid quenching of chlorophyll triplet states via energy transfer to surrounding carotenoids, thereby avoiding the generation and damaging effects of singlet oxygen.[26]

Following the transfer of energy to a reaction center, the resulting excited state is transformed to charge-separated states. In biological photosynthetic assemblies, multistep

4
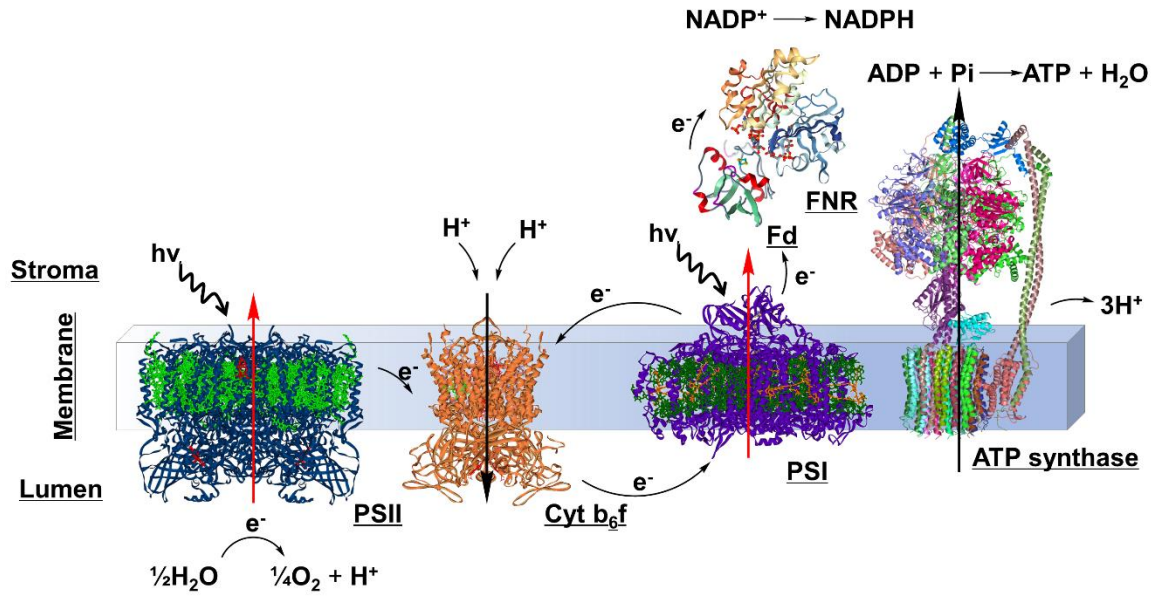
Figure 1.1 A diagrammatic scheme highlighting the light-induced electron- and proton-transfer reactions occurring within and across the thylakoid membrane of oxygenic photosynthetic organisms. Four major intramembranous protein complexes are shown, including Photosystem II (PSII; water-plastoquinone oxidoreductase), cytochrome (Cyt) b_6f (plastoquinol-plastocyanin-oxidoreductase), Photosystem I (PSI; plastocyanin-ferredoxin-oxidoreductase), and ATP synthase.

electron-transfer reactions involving molecular cofactors spatially separate charges, resulting in relatively long lifetimes of the final charge-separated state and an electron motive force that is appropriate for meeting the thermodynamic demands of water splitting.[22,23] As an example, initiation of photoinduced charge transfer reactions from the excited-state reaction center of PSI to neighboring chlorophyll a (A_0) is followed by a series of subsequent electron-transfer steps involving phylloquinone (A_1), three iron-sulfur protein clusters (F_x, F_A, and F_B) (Figure 1.2), and ferredoxin, which shuttles electrons to ferredoxin–$NADP^+$ reductase.[23,27] Each electron-transfer step increases the

5
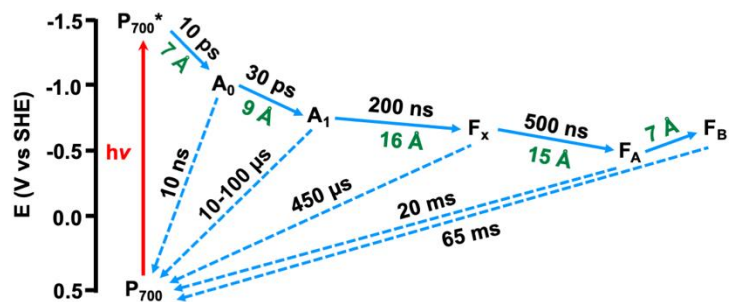
Figure 1.2 Energy-kinetic diagram showing the photochemistry and electron-transfer events associated with PSI. In this diagram, chlorophyll A_0 serves as a redox mediator between the excited state P700* reaction center and phylloquinone A_1.

physical distance between the resulting electron–hole pair (~7–16 Å per electron transfer (ET)), thereby reducing the rates of charge recombination.[22] However, each electron-transfer step occurs at the thermodynamic expense of utilizing a fraction of the initially absorbed photonic energy and therefore limits the energy that can be stored in chemical products.

As shown in Figure 1.3, the electron-transfer kinetics associated with photosynthetic complexes, including PSI, have been modeled using the Marcus-Hush-Levich equation, where the rate constant for ET (k_{et}) in the adiabatic regime is described by Equation 1.1:[28-30]

$$k_{et} = \sqrt{\left(\frac{\pi}{\hbar^2 \lambda k_B T}\right)} |H_{AB}|^2 e^{\left[-\frac{(\Delta G° + \lambda)^2}{4\lambda k_B T}\right]} \tag{1.1}$$

In Equation 1.1, the pre-exponential factor includes the reduced Planck constant ($\hbar = 1.054571 \times 10^{-34}$ J s), the reorganization energy (λ) (describing the energy required for structural adjustments to distort the nuclear configuration of the reactants into the nuclear
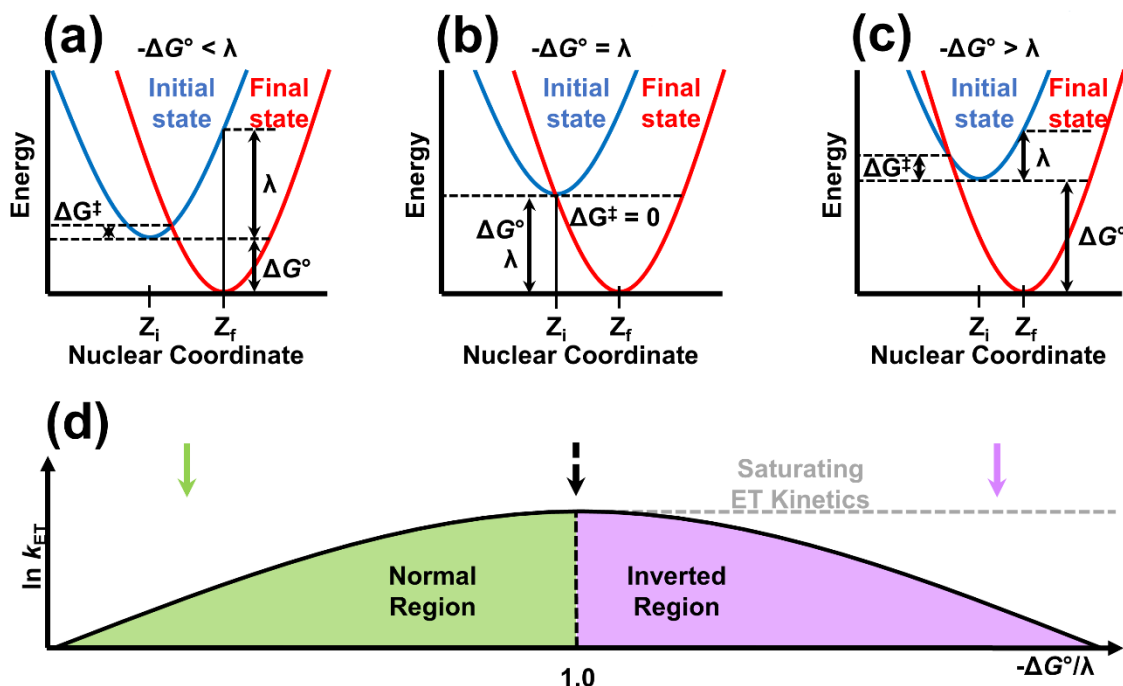
Figure 1.3 (a-c) Marcusian diagrams with potential energy surfaces for electron transfer from an initial state (blue) to a final state (red). Each case represents one of three different scenarios in the (d) Marcus curve: normal region (green), the activationless point (dashed black line), the inverted region (pink), and saturating electron-transfer kinetics (dashed gray line).

configuration of the products without charge transfer occurring), the Boltzmann constant ($k_B = 1.380649$ x 10^{-23} J K^{-1}), temperature (T), and the electronic matrix element (H_{AB}) (describing the overlap of donor and acceptor orbitals between the reactants and products). The exponential term is the Frank-Condon factor, which includes $\Delta G°$ for the electron-transfer reaction and λ. Equation 1.1 is essentially a nonlinearized version of the Butler-Volmer expression,[31,32] where the charge-transfer coefficient changes as a function of the driving force. In general, there are three distinct regimes of ET kinetics associated

with Marcus-Hush-Levich theory. In the normal region, where the negative standard

Gibbs free energy change for ET is less than λ (*i.e.*, $-\Delta G° < \lambda$), the rate of ET increases as

a function of increasing thermodynamic driving force (Figure 1.3a). When the negative

standard Gibbs free energy change for ET is equal in value to λ ($-\Delta G° = \lambda$) ET becomes

activationless and the rate of ET is thus maximized (Figure 1.3b). Further increasing the

driving force to conditions where the negative standard Gibbs free energy change for ET

is greater than λ ($-\Delta G° > \lambda$) results in inverted region kinetics where the rate of ET

decreases as the thermodynamic driving force increases (Figure 1.3c). Inverted region

behavior has been invoked to rationalize the relatively sluggish kinetics associated with

charge recombination pathways in biological photosynthesis (indicated with dashed blue

arrows in Figure 1.2) as compared to the relatively fast rates of forward electron-transfer

steps (indicated with solid blue arrows in Figure 1.2). Similar inverted region behavior is

generally not observed in electron-transfer reactions involving electrode materials (as

indicated by the dashed gray line of Figure 1.3d). In this case, the relatively high density

of states associated with conductive materials favors overlap of initial and final states

with activationless electron-transfer kinetics.

An overall equation for natural photosynthesis is shown in Equation 1.2.

$$6CO_2 + 12H_2O + h\nu \rightarrow C_6H_{12}O_6 + 6O_2 + 6H_2O \qquad (1.2)$$
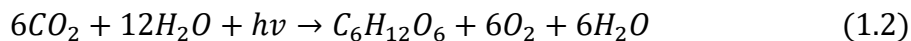
Consistent with this equation, Ruben and coworkers have shown via ^{18}O isotope labeling

experiments that oxygen atoms of the product O_2 are derived from oxygen atoms of

reactant H_2O, and the oxygen atoms of the reactant CO_2 are used to form additional

molecules of H_2O in the product state.[33] By utilizing photoinduced charge-separation

reactions, photosynthetic organisms are capable of extracting electrons from water at the

oxygen evolving complex (OEC) of Photosystem II (PSII) and storing them in the form of relatively high energy chemical reducing equivalents. In this process PSII and PSI act in series, with PSII handling the oxidative chemistry (Equation 1.3a) and PSI handling the reductive chemistry (Equation 1.3b) via a 'wireless' process that achieves overall splitting of water.

$$2H_2O \longrightarrow O_2 + 4H^+ + 4e^- \qquad (1.3a)$$

$E^{\circ'}$ = -0.81 V vs NHE (pH 7)

$$2NADP^+ + 4H^+ + 4e^- \longrightarrow 2NADPH + 2H^+ \qquad (1.3b)$$

$E^{\circ'}$ = -0.32 V vs NHE (pH 7)

In PSI, electrons are transferred to the ferredoxin–NADP$^+$ reductase enzyme and used to facilitate light-driven formation of reduced nicotinamide adenine dinucleotide phosphate (NADPH) (Figure 1.1). NADPH can also be generated along with CO_2 by the breakdown of glucose ($C_6H_{12}O_6$) via the pentose phosphate pathway. NADPH is then utilized as a chemical reductant in the Calvin-Benson-Bassham cycle, sometimes referred to as the reductive pentose phosphate pathway, where CO_2 fixation occurs to form glyceraldehyde-3-phosphate (G3P), which is used to form carbohydrates, including glucose.[34,35] Unlike the light-driven processes occurring at PSII and PSI, the Calvin Cycle occurs in the dark. As shown in Equation 1.4, this cycle involves proton- as well as electron-transfer reactions that are powered by the hydrolysis of adenosine triphosphate (ATP), a molecule which stores as well as intracellularly transports energy in chemical form and is also a product of photosynthesis (*vide infra*).

$$3CO_2 + 6NADPH + 6H^+ + 9ATP \rightarrow G3P + 6NADP^+ + 9ADP + 3H_2O + 8P_i \quad (1.4)$$
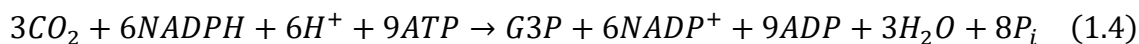
Electron-transfer reactions in biology are often coupled to proton-transfer reactions.

As an example involving oxygenic photosynthesis, the cytochrome plastoquinol-plastocyanin-oxidoreductase (Cyt b_6f) complex shuttles electrons between plastoquinol, which forms upon the reduction of plastoquinone at the Q_B site of PSII, to plastocyanin, which in turn transfers electrons to the P700 cofactor of PSI, while also pumping protons from the stromal side of the membrane protein to its luminal side. This results in the formation of a proton-motive force (PMF) that ultimately powers the synthesis of ATP (Figure 1.1).[36-39] Thus, a fraction of the initially absorbed photonic energy is used to drive the formation of electron as well as proton gradients and the generation of NADPH as well as ATP. Proton-coupled electron transfer (PCET) processes found in biology have inspired the design of synthetic assemblies.[40-49] Ultimately, the ability to incorporate and control PCET processes is essential to designing artificial photosynthetic systems that effectively couple the inherent one-photon to one-electron chemistry of light absorption with the multielectron, multiproton chemistry required for nearly all fuel-forming reactions relevant to solar photochemistry (Table 1.1).[50-56]

1.4 From Enzymes to Human-engineered Catalysts

Nature employs myriad of enzymes for catalyzing various redox half-reactions, including oxygen evolution, hydrogen evolution, carbon dioxide reduction, nitrogen reduction, and oxygen reduction reactions.[57-61] These enzymes feature active sites containing earth-abundant metal centers coordinated to soft-material frameworks (in the case of proteins, amino acid residues) which are proposed to provide primary, secondary, and further extended coordination environments that promote effective catalysis.[59,62-65] In this context, the three-dimensional chemical environments of enzymes are the product of four billion years of evolution that have amplified their catalytic activity and selectivity by

Table 1.1 Formal ($E°$' at pH 7) and standard[a] ($E°$ at pH 0) potentials written as reduction half-reactions by convention.

Half-reactions relevant to Solar Photochemistry	
Half-reactions	Potential (V vs NHE)
$N_2 + e^- \rightarrow N_2^-$	$E°' = -4.2$
$N_2 + H^+ + e^- \rightarrow N_2H$	$E° = -3.2^a$
$CO_2 + e^- \rightarrow CO_2^{•-}$	$E°' = -1.90$
$CO_2 + 2H^+ + 2e^- \rightarrow HCO_2H$	$E°' = -0.61$
$CO_2 + 2H^+ + 2e^- \rightarrow CO + H_2O$	$E°' = -0.53$
$2CO_2 + 2H^+ + 2e^- \rightarrow H_2C_2O_4$	$E°' = -0.49$
$CO_2 + 4H^+ + 4e^- \rightarrow HCHO + H_2O$	$E°' = -0.48$
$2H^+ + 2e^- \rightarrow H_2$	$E°' = -0.41$
$CO_2 + 6H^+ + 6e^- \rightarrow CH_3OH + H_2O$	$E°' = -0.38$
$CO_2 + 8H^+ + 8e^- \rightarrow CH_4 + 2H_2O$	$E°' = -0.24$
$N_2 + 5H^+ + 4e^- \rightarrow N_2H_5^+$	$E° = -0.23^a$
$N_2 + 8H^+ + 6e^- \rightarrow 2NH_4^+$	$E° = +0.28^a$
$O_2 + 4H^+ + 4e^- \rightarrow 2H_2O$	$E°' = +0.81$
$HOO^• + 3H^+ + 3e^- \rightarrow 2H_2O$	$E°' = +1.26$
$HOOH + 2H^+ + 2e^- \rightarrow 2H_2O$	$E°' = +1.37$
$HO^• + H^+ + e^- \rightarrow H_2O$	$E°' = +2.39$

[a] In these selected examples, where the chemical form of the product depends on the pH of the solution, standard reduction potentials (at pH 0) are reported instead of

promoting favorable binding of substrates, selective formation of transition states, stabilization of intermediates, favorable release of products, and tuning as well as leveling of the redox potentials encountered across a reaction coordinate.[63] In one example of redox tuning, the metal centers of Fe-containing complexes in biological assemblies span over a 1 Volt range in their midpoint potential (Figure 1.4).[66-70]
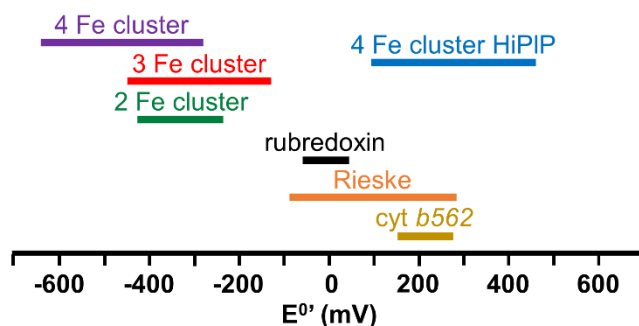
Figure 1.4. The redox span of iron complexes in biological systems.

The favorable properties of enzymes have made them targets for integration with solid-state electrode materials, and the process of mediating current flow between biological complexes and conductive surfaces has led to applications in sensor technologies, fuel cells, and electrocatalysis.[61,71-77] However, in the context of solar-to-fuels technologies, the relatively large molecular footprint and fragility of enzymes restricts several industrial applications. As an example, one mole of *D. desulfuricans* hydrogenase enzyme, which can produce 9,000 hydrogen molecules per second per enzyme,[78] could fill the airship *Graf Zeppelin* in ~10 min or the main liquid-hydrogen tank of a space shuttle in ~2 h,[79] but given its molecular weight of ~53 kDa, one mole of

12

hydrogenase equates to ~120 lbs. (~55 kg). Such characteristics have prompted researchers to investigate the design of more streamlined assemblies including the pursuit of both *top-down* and *bottom-up* strategies.[59,74,80]

The well-defined structures of enzymes have been modulated to investigate and better understand structure-function relationships. In addition to amino acid mutations within the biological toolbox, strategies to incorporate chemical functionalities not found in nature have also been explored including the use of unnatural amino acids, development of chimeric proteins, and de novo protein synthesis.[81-91] For example, synthetic functional models of the [Fe-Fe] site of hydrogenase have been effectively incorporated into the protein apo-HydA.[92] In a related vein, the rubredoxin scaffold has been used to coordinate Ni in place of its native Fe metal center, resulting in a hydrogen evolution catalyst that is oxygen tolerant.[93] The development of human-engineered molecular catalysts, which are often inspired by the active sites of enzymes, also continues to be an active area of research. In one particular example, Ni catalysts containing diphosphine ligands developed by DuBois and coworkers[94] have been studied as homogeneous electrocatalysts as well as components in heterogeneous electrocatalytic assemblies and in photoelectrosynthetic cells.[95-97] Shaw and coworkers have further shown that synthetically adding amino acids to the outer coordination sphere of this class of catalysts can significantly enhance their performance by reducing the overpotential (η) required to achieve a given rate of H_2 production, improving their solubility, and enhancing their stability during catalytic operation. These examples highlight promising features of extended three-dimensional environments for controlling the reactivity of catalytic sites.[98-101]

1.5 Porphyrins as Catalytic Models

Catalysts are central to energy conversion in biology and technology.[22,91,102-108] They provide low-energy pathways for steering chemical transformations and are used in applications ranging from manufacturing fuels and fine chemicals to controlling the bioenergetic reactions essential to all living organisms. In technological processes, the solid-state form factors of heterogeneous electrocatalytic materials make them conducive to many industrial applications, including reactions where they provide a means of activating small molecules at electrified interfaces.[109] Conversely, the study of homogeneous molecular catalysts has provided researchers significant insights regarding mechanisms and active site structure-function relationships governing myriad catalytic processes.[62,63,110,111] Unlike traditional surface electrocatalysts, where the active sites are integral to the electrode, contribute to the Fermi level, and are structurally less well-defined, favorable features of homogeneous molecular electrocatalysts include enhanced synthetic control over their physical properties as dictated by their well-defined structures. Thus, they are distinct entities with their own electronic and chemical properties.

In this context, tetrapyrrolic macrocycles, including metalloporphyrins, have garnered significant attention[112-121] as they are essential to the function of biological systems and serve as molecular components in existing and emerging technologies. As electrocatalysts, metalloporphyrins are capable of chemically transforming protons into hydrogen as well as converting carbon dioxide into carbon monoxide and other reduced forms of carbon.[122-141]

The hydrogen evolution reaction (HER), for example, is a half reaction fundamental

to several chemical transformations with relevance to energy transduction, is among the simplest PCET reactions (Equation 1.5). The long-established industrial catalyst for activating this transformation is elemental platinum. However, concerns that future market demands for platinum and other rare-earth elements could outpace availability have prompted researchers to seek alternative materials and design principles to prepare catalysts for the production of hydrogen and other industrially relevant chemicals.[11,142,143] In the rapidly developing field of molecular electrocatalysis, researchers continue to explore the use of chemical coordination environments to control the catalytic properties of earth-abundant elements, facilitating mechanistic studies that can be prohibitive in more complex heterogeneous assemblies and thus aiding the design of better homogeneous as well as heterogeneous catalysts.[94,101,144-149]

$$2H^+ + 2e^- \rightarrow H_2 \tag{1.5}$$

Although fused bimetallic porphyrin architectures have been investigated for applications in optics, molecular wires, and organic conducting materials,[150-160] there is a dearth of reports on the catalytic properties of this class of compounds. It has been postulated that fused bimetallic porphyrins possess favorable properties for applications in electrocatalysis, including the ability to 1) store multiple redox equivalents, 2) delocalize electrons across an extended multi-metallic scaffold, 3) be reduced as well as oxidized at significantly less applied bias potentials compared to those required for analogous non-fused porphyrins, and 4) provide an alternative strategy, compared to the use of electron-withdrawing or electron-donating functional groups, to adjust the redox properties of molecular catalysts.[161,162]

15

1.6 Controlling Multi-Electron and Multi-Proton Reaction Networks

The water-plastoquinone oxidoreductase enzyme, better known as PSII, carries out the water oxidation reaction, using the energy of four photons to produce one molecular oxygen, four protons, and two reduced equivalents (quinones) (Equation 1.3a).[23,163,164] The protons obtained from water splitting contribute to the generation of PMF (the difference in electrochemical potential of protons across a membrane), which in turn drives myriad bioenergetic processes including the synthesis of ATP from ADP and inorganic phosphate.[23,36,165] For the water oxidation reaction, a cluster of chlorophyll *a*, collectively denominated P680, is photoexcited, and decays by an initial electron-transfer to the quinone cofactors Q_A and Q_B, generating $P680^{\bullet+}$. This oxidized species is then reduced by a tyrosine residue (Tyr_z) which loses its phenolic proton to a nearby histidine (His190), forming a neutral tyrosine radical (electrochemically poised at 0.9–1.0 V vs SCE). After this PCET reaction, the radical removes one electron from the OEC, and after four of these light-induced charge separations, OEC oxidizes two water molecules and returns to its initial oxidation state.[166] The Tyr_z-His190 pair appear fundamental to many biological energy transduction systems.[40-42,167,168] Beyond the single proton transfer just described, it has been postulated that a series of proton transfers can be associated with the oxidation of the phenol in the form of networks of hydrogen-bonded polar residues and water molecules, where protons can diffuse by a Grotthuss-type mechanism spanning the ~20 Å distance between the OEC and the lumen.[165,169,170]

In order to understand the functional principles of this sophisticated mechanism, different bioinspired artificial models involving phenol-based moieties have been extensively studied.[49,114,171-195] Particularly, benzimidazole-phenol (BIP) dyads (where

the benzimidazole models the His190 and the phenol models the Tyr$_z$) provides a minimalist construct demonstrating PCET.[49,114,174,181-187,190-196] The synthetic control of the benzimidazole's substituents, serving as terminal proton acceptors (TPA), allows to stimulate the hydrogen bond network and regulate multiple proton transfers upon a phenol oxidation.[185-187,190,191,194-196] As an example, the reversible movement of up to four protons was demonstrated, spanning a space of ~16 Å.[187] In another work, depending on the pK_a of the TPA moiety, the proton translocation was limited to E1PT even when the system was designed to do E2PT.[185] Additionally, the P680 can also be included into the model by incorporating photosensitizers such as porphyrins or organometallic complexes.[49,114,181-184,186,192,193,195,196]

Controlling the movement of electrons and protons is a fundamental tool for the development of better artificial bioinspired proton wires and energy coupling membranes, capable of performing a range of bioenergetic processes observed in nature. With this basic knowledge, natural photosynthesis can be re-imagined, re-engineered, improved, and ultimately, applied towards a more sustainable energy industry.

1.7 References

(1)   Zeifman, L.; Hertog, S.; Kantorova, V.; Wilmoth, J. *A World of 8 Billion*; UN Department of Economic and Social Affair, **2022**. https://www.un.org/development/desa/dpad/publication/un-desa-policy-brief-no-140-a-world-of-8-billion/

(2)   Cozzi, L.; Gould, T. *World Energy Outlook 2022*; International Energy Agency, **2022**. https://www.iea.org/reports/world-energy-outlook-2022

(3)   National Oceanic and Atmospheric Administration. *Global Monitoring Laboratory - Carbon Cycle Greenhouse Gases*.

(4)   Lüthi, D.; Le Floch, M.; Bereiter, B.; Blunier, T.; Barnola, J. M.; Siegenthaler, U.; Raynaud, D.; Jouzel, J.; Fischer, H.; Kawamura, K.; Stocker, T. F. High-

Resolution Carbon Dioxide Concentration Record 650,000-800,000 Years before Present. *Nature* **2008**, *453* (7193), 379–382.

(5)   Lewis, N. S.; Nocera, D. G. Powering the Planet: Chemical Challenges in Solar Energy Utilization. *Proc. Natl. Acad. Sci. U.S.A.* **2006**, *103* (43), 15729–15735.

(6)   Blankenship, R. E.; Tiede, D. M.; Barber, J.; Brudvig, G. W.; Fleming, G.; Ghirardi, M.; Gunner, M. R.; Junge, W.; Kramer, D. M.; Melis, A.; Moore, T. A.; Moser, C. C.; Nocera, D. G.; Nozik, A. J.; Ort, D. R.; Parson, W. W.; Prince, R. C.; Sayre, R. T. Comparing Photosynthetic and Photovoltaic Efficiencies and Recognizing the Potential for Improvement. *Science* **2011**, *332*, 805–809.

(7)   Gust, D.; Moore, T.; Moore, A. Solar Fuels via Artificial Photosynthesis. *Acc. Chem. Res.* **2009**, *42* (12), 1890–1898.

(8)   Listorti, A.; Durrant, J.; Barber, J. Artificial Photosynthesis: Solar to Fuel. *Nat. Mater.* **2009**, *8* (12), 929–930.

(9)   Faunce, T.; Styring, S.; Wasielewski, M. R.; Brudvig, G. W.; Rutherford, A. W.; Messinger, J.; Lee, A. F.; Hill, C. L.; Degroot, H.; Fontecave, M.; MacFarlane, D. R.; Hankamer, B.; Nocera, D. G.; Tiede, D. M.; Dau, H.; Hillier, W.; Wang, L.; Amal, R. Artificial Photosynthesis as a Frontier Technology for Energy Sustainability. *Energy Environ. Sci.* **2013**, *6* (4), 1074–1076.

(10)   Faunce, T. A.; Lubitz, W.; Rutherford, A. W.; MacFarlane, D.; Moore, G. F.; Yang, P.; Nocera, D. G.; Moore, T. A.; Gregory, D. H.; Fukuzumi, S.; Yoon, K. B.; Armstrong, F. A.; Wasielewski, M. R.; Styring, S. Energy and Environment Policy Case for a Global Project on Artificial Photosynthesis. *Energy Environ. Sci.* **2013**, *6* (3), 695–698.

(11)   Ardo, S.; Fernandez Rivas, D.; Modestino, M. A.; Schulze Greiving, V.; Abdi, F. F.; Alarcon Llado, E.; Artero, V.; Ayers, K.; Battaglia, C.; Becker, J. P.; Bederak, D.; Berger, A.; Buda, F.; Chinello, E.; Dam, B.; Di Palma, V.; Edvinsson, T.; Fujii, K.; Gardeniers, H.; Geerlings, H.; Hashemi, S. M.; Haussener, S.; Houle, F.; Huskens, J.; James, B. D.; Konrad, K.; Kudo, A.; Kunturu, P. P.; Lohse, D.; Mei, B.; Miller, E. L.; Moore, G. F.; Muller, J.; Orchard, K. L.; Rosser, T. E.; Saadi, F. H.; Schüttauf, J. W.; Seger, B.; Sheehan, S. W.; Smith, W. A.; Spurgeon, J.; Tang, M. H.; Van De Krol, R.; Vesborg, P. C. K.; Westerik, P. Pathways to Electrochemical Solar-Hydrogen Technologies. *Energy Environ. Sci.* **2018**, *11* (10), 2768–2783.

(12)   Archer, M. D.; Barber, J. *Series on Photoconversion of Solar Energy, Vol. 2: Molecular to Global Photosynthesis*; Imperial College Press: London, 2004.

(13)   120,000 TW Power of the Sun.

(14)   Fischer, W. W.; Hemp, J.; Johnson, J. E. Evolution of Oxygenic Photosynthesis. *Annu. Rev. Earth Planet. Sci.* **2016**, *44*, 647–683.

(15)   Gust, D.; Kramer, D.; Moore, A.; Moore, T. A.; Vermaas, W. Engineered and Artificial Photosynthesis: Human Ingenuity Enters the Game. *MRS Bull* **2008**, *33* (4), 383–387.

(16)   Faunce, T. Global Artificial Photosynthesis and Renewable Energy Storage and Policy for the Sustainocene. *Adv. Sustainable Syst.* **2018**, *2*, 1800035.

(17)   Tumas, B.; Dempsey, J. L.; Mallouk, T. E. *Basic Energy Sciences Roundtable on Liquid Solar Fuels*; 2019.

(18)   Thorp, H. H. Do Us a Favor. *Science* **2020**, *367* (6483), 1169.

(19)   Hemminger, J.; Fleming, G.; Ratner, M. *Directing Matter and Energy: Five Challenges for Science and the Imagination*; 2007.

(20)   Rutherford, A. W.; Moore, T. A. Mimicking Photosynthesis, but Just the Best Bits. *Nature* **2008**, *453* (7194), 449.

(21)   Green, B. R.; Parson, W. W. *Advances in Photosynthesis and Respiration, Vol. 13: Light-Harvesting Antennas in Photosynthesis*, 1st Ed.; Springer Netherlands: Dordrecht, 2003.

(22)   Moore, G. F.; Brudvig, G. W. Energy Conversion in Photosynthesis: A Paradigm for Solar Fuel Production. *Annu. Rev. Condens. Matter Phys.* **2011**, *2* (1), 303–327.

(23)   Blankenship, R. E. *Molecular Mechanisms of Photosynthesis*, 2nd Ed.; Wiley-Blackwell, 2014.

(24)   Long, S. P.; Humphries, S. Photoinhibition of Photosynthesis in Nature. *Annu. Rev. Plant Physiol. Plant Mol. Biol.* **1994**, *45*, 633–662.

(25)   Goh, C. H.; Ko, S. M.; Koh, S.; Kim, Y. J.; Bae, H. J. Photosynthesis and Environments: Photoinhibition and Repair Mechanisms in Plants. *J. Plant Biol.* **2012**, *55* (2), 93–101.

(26)   Durrant, J. R.; Giorgi, L. B.; Barber, J.; Klug, D. R.; Porter, G. Characterisation of Triplet States in Isolated Photosystem II Reaction Centres: Oxygen Quenching as a Mechanism for Photodamage. *Biochim. Biophys. Acta* **1990**, *1017* (2), 167–175.

(27)   Guergova-Kuras, M.; Boudreaux, B.; Joliot, A.; Joliot, P.; Redding, K. Evidence for Two Active Branches for Electron Transfer in Photosystem I. *Proc. Natl. Acad. Sci. U.S.A.* **2001**, *98* (8), 4437–4442.

(28)   Marcus, R. A.; Sutin, N. Electron Transfers in Chemistry and Biology. *Biochim Biophys Acta* **1985**, *811*, 265–322.

(29)   Moser, C. C.; Keske, J. M.; Warncke, K.; Farid, R. S.; Dutton, P. L. Nature of Biological Electron Transfer. *Nature* **1992**, *355*, 796–802.

(30)   Gray, H. B.; Winkler, J. R. Electron Transfer in Proteins. *Annu. Rev. Biochem.* **1996**, *65*, 537–561.

(31)   Bard, A. J.; Faulkner, L. R. *Electrochemical Methods: Fundamentals and Applications*, 2nd ed.; Wiley & Sons, 2001.

(32)   Savéant, J.-M.; Costentin, C. *Elements of Molecular and Biomolecular Electrochemistry: An Electrochemical Approach to Electron Transfer Chemistry*, 2nd Ed.; Wiley & Sons: Hoboken, 2019.

(33)   Ruben, S.; Randall, M.; Kamen, M.; Hyde, J. L. Heavy Oxygen (O^{18}) as a Tracer in the Study of Photosynthesis. *J. Am. Chem. Soc.* **1941**, *63* (3), 877–879.

(34)   Gontero, B.; Lebreton, S.; Graciet, E. Multienzyme Complexes Involved in the Benson-Calvin Cycle and in Fatty Acid Metabolism. In *Annual Plant Reviews, Volume 7: Protein-Protein Interactions in Plant Biology*; McManus, M. T., Laing, W. A., Allan, A. C., Eds.; Sheffield Academic Press: Sheffield, 2002; pp 125–157.

(35)   Raines, C. A. The Calvin Cycle Revisited. *Photosynth. Res.* **2003**, *75*, 1–10.

(36)   Mitchell, P. Coupling of Phosphorylation to Electron and Hydrogen Transfer by a Chemi-Osmotic Type of Mechanism. *Nature* **1961**, *191* (4784), 144–148.

(37)   Mitchell, P. Chemiosmotic Coupling in Oxidative and Photosynthetic Phosphorylation. *Biochim. Biophys. Acta* **2011**, *1807* (12), 1507–1538.

(38)   Martin, J. L.; Ishmukhametov, R.; Hornung, T.; Ahmad, Z.; Frasch, W. D. Anatomy of F_1-ATPase Powered Rotation. *Proc. Natl. Acad. Sci. U.S.A.* **2014**, *111* (10), 3715–3720.

(39)   Junge, W.; Nelson, N. ATP Synthase. *Annu. Rev. Biochem.* **2015**, *84*, 631–657.

(40)   Cukier, R. I.; Nocera, D. G. Proton-Coupled Electron Transfer. *Annu. Rev. Phys. Chem.* **1998**, *49*, 337–369.

(41) Mayer, J. M. Proton-Coupled Electron Transfer: A Reaction Chemist's View. *Annu. Rev. Phys. Chem.* **2004**, *55*, 363–390.

(42) Huynh, M. H. V.; Meyer, T. J. Proton-Coupled Electron Transfer. *Chem. Rev.* **2007**, *107* (11), 5004–5064.

(43) Hammarström, L.; Styring, S. Coupled Electron Transfers in Artificial Photosynthesis. *Philos. Trans. R. Soc. B: Biol. Sci.* **2008**, *363* (1494), 1283–1291.

(44) Hammes-Schiffer, S. Theory of Proton-Coupled Electron Transfer in Energy Conversion Processes. *Acc. Chem. Res.* **2009**, *42* (12), 1881–1889.

(45) Dempsey, J. L.; Winkler, J. R.; Gray, H. B. Proton-Coupled Electron Flow in Protein Redox Machines. *Chem. Rev.* **2010**, *110* (12), 7024–7039.

(46) Hammarström, L.; Styring, S. Proton-Coupled Electron Transfer of Tyrosines in Photosystem II and Model Systems for Artificial Photosynthesis: The Role of a Redox-Active Link between Catalyst and Photosensitizer. *Energy Environ. Sci.* **2011**, *4* (7), 2379–2388.

(47) Weinberg, D. R.; Gagliardi, C. J.; Hull, J. F.; Murphy, C. F.; Kent, C. A.; Westlake, B. C.; Paul, A.; Ess, D. H.; McCafferty, D. G.; Meyer, T. J. Proton-Coupled Electron Transfer. *Chem. Rev.* **2012**, *112* (7), 4016–4093.

(48) Hammes-Schiffer, S. Proton-Coupled Electron Transfer: Moving Together and Charging Forward. *J. Am. Chem. Soc.* **2015**, *137* (28), 8860–8871.

(49) Mora, S. J.; Odella, E.; Moore, G. F.; Gust, D.; Moore, T. A.; Moore, A. L. Proton-Coupled Electron Transfer in Artificial Photosynthetic Systems. *Acc. Chem. Res.* **2018**, *51* (2), 445–453.

(50) Chen, H. Y.; Ardo, S. Direct Observation of Sequential Oxidations of a Titania-Bound Molecular Proxy Catalyst Generated through Illumination of Molecular Sensitizers. *Nat. Chem.* **2018**, *10* (1), 17–23.

(51) Berardi, S.; Drouet, S.; Francàs, L.; Gimbert-Suriñach, C.; Guttentag, M.; Richmond, C.; Stoll, T.; Llobet, A. Molecular Artificial Photosynthesis. *Chem. Soc. Rev.* **2014**, *43* (22), 7501–7519.

(52) Hammarström, L. Accumulative Charge Separation for Solar Fuels Production: Coupling Light-Induced Single Electron Transfer to Multielectron Catalysis. *Acc. Chem. Res.* **2015**, *48* (3), 840–850.

(53) Lindley, B. M.; Appel, A. M.; Krogh-Jespersen, K.; Mayer, J. M.; Miller, A. J. M. Evaluating the Thermodynamics of Electrocatalytic N_2 Reduction in Acetonitrile. *ACS Energy Lett.* **2016**, *1* (4), 698–704.

(54) Li, H.; Li, J.; Ai, Z.; Jia, F.; Zhang, L. Oxygen Vacancy-Mediated Photocatalysis of BiOCl: Reactivity, Selectivity, and Perspectives. *Angew. Chem. Int. Ed.* **2018**, *57* (1), 122–138.

(55) Beiler, A. M.; Moore, G. F. Multi-Electron-Transfer Photochemistry: Caught in the Act. *Nat. Chem.* **2018**, *10* (1), 3–4.

(56) Chen, X.; Li, N.; Kong, Z.; Ong, W. J.; Zhao, X. Photocatalytic Fixation of Nitrogen to Ammonia: State-of-the-Art Advancements and Future Prospects. *Mater. Horiz.* **2018**, *5* (1), 9–27.

(57) Woodrow, I. E. Enzymatic Regulation Photosynthetic CO_2 Fixation in C_3 Plants. *Annu. Rev. Plant Physiol. Plant Mol. Biol.* **1988**, *39* (1009), 533–594.

(58) Evans, D. J.; Pickett, C. J. Chemistry and the Hydrogenases. *Chem. Soc. Rev.* **2003**, *32* (5), 268–275.

(59) Bachmeier, A.; Armstrong, F. A. Solar-Driven Proton and Carbon Dioxide Reduction to Fuels - Lessons from Metalloenzymes. *Curr. Opin. Chem. Biol.* **2015**, *25*, 141–151.

(60) Del Barrio, M.; Sensi, M.; Orain, C.; Baffert, C.; Dementin, S.; Fourmond, V.; Léger, C. Electrochemical Investigations of Hydrogenases and Other Enzymes That Produce and Use Solar Fuels. *Acc. Chem. Res.* **2018**, *51* (3), 769–777.

(61) Evans, R. M.; Siritanaratkul, B.; Megarity, C. F.; Pandey, K.; Esterle, T. F.; Badiani, S.; Armstrong, F. A. The Value of Enzymes in Solar Fuels Research - Efficient Electrocatalysts through Evolution. *Chem. Soc. Rev.* **2019**, *48*, 2039–2052.

(62) Cracknell, J. A.; Vincent, K. A.; Armstrong, F. A. Enzymes as Working or Inspirational Electrocatalysts for Fuel Cells and Electrolysis. *Chem. Rev.* **2008**, *108* (7), 2439–2461.

(63) Armstrong, F. A.; Hirst, J. Reversibility and Efficiency in Electrocatalytic Energy Conversion and Lessons from Enzymes. *Proc. Natl. Acad. Sci. U.S.A.* **2011**, *108* (34), 14049–14051.

(64) Shaw, W. J. The Outer-Coordination Sphere: Incorporating Amino Acids and Peptides as Ligands for Homogeneous Catalysts to Mimic Enzyme Function. *Catal. Rev. Sci. Eng.* **2012**, *54* (4), 489–550.

(65)   Zhao, M.; Wang, H. B.; Ji, L. N.; Mao, Z. W. Insights into Metalloenzyme Microenvironments: Biomimetic Metal Complexes with a Functional Second Coordination Sphere. *Chem. Soc. Rev.* **2013**, *42* (21), 8360–8375.

(66)   Gunner, M. R.; Honig, B. Electrostatic Control of Midpoint Potentials in the Cytochrome Subunit of the *Rhodopseudomonas Viridis* Reaction Center. *Proc. Natl. Acad. Sci. U.S.A.* **1991**, *88* (20), 9151–9155.

(67)   Mao, J.; Hauser, K.; Gunner, M. R. How Cytochromes with Different Folds Control Heme Redox Potentials. *Biochemistry* **2003**, *42* (33), 9829–9840.

(68)   Gray, H. B.; Stiefel, E. I.; Valentine, J. S.; Bertini, I. *Biological Inorganic Chemistry Structure and Reactivity*, 1st Ed.; University Science Books, 2007.

(69)   Zheng, Z.; Gunner, M. R. Analysis of the Electrochemistry of Hemes with E_ms Spanning 800 MV. *Proteins* **2009**, *75* (3), 719–734.

(70)   Liu, J.; Chakraborty, S.; Hosseinzadeh, P.; Yu, Y.; Tian, S.; Petrik, I.; Bhagi, A.; Lu, Y. Metalloproteins Containing Cytochrome, Iron-Sulfur, or Copper Redox Centers. *Chem. Rev.* **2014**, *114* (8), 4366–4369.

(71)   Zamost, B. L.; Nielsen, H. K.; Starnes, R. L. Thermostable Enzymes for Industrial Applications. *J. Ind. Microbiol. Biotechnol.* **1991**, *8*, 71–81.

(72)   Tye, J. W.; Hall, M. B.; Darensbourg, M. Y. Better than Platinum? Fuel Cells Energized by Enzymes. *Proc. Natl. Acad. Sci. U.S.A.* **2005**, *102* (47), 16911–16912.

(73)   Meredith, M. T.; Minteer, S. D. Biofuel Cells: Enhanced Enzymatic Bioelectrocatalysis. *Annu. Rev. Anal. Chem.* **2012**, *5*, 157–179.

(74)   Woolerton, T. W.; Sheard, S.; Chaudhary, Y. S.; Armstrong, F. A. Enzymes and Bio-Inspired Electrocatalysts in Solar Fuel Devices. *Energy Environ. Sci.* **2012**, *5* (6), 7470–7490.

(75)   Liese, A.; Hilterhaus, L. Evaluation of Immobilized Enzymes for Industrial Applications. *Chem. Soc. Rev.* **2013**, *42* (15), 6236–6249.

(76)   Rasmussen, M.; Abdellaoui, S.; Minteer, S. D. Enzymatic Biofuel Cells: 30 Years of Critical Advancements. *Biosens. Bioelectron.* **2016**, *76*, 91–102.

(77)   Porter, J. L.; Rusli, R. A.; Ollis, D. L. Directed Evolution of Enzymes for Industrial Biocatalysis. *ChemBioChem* **2016**, *17* (3), 197–203.

(78) Frey, M. Hydrogenases: Hydrogen-Activating Enzymes. *ChemBioChem* **2002**, *3*, 153–160.

(79) Cammack, R. Hydrogenase Sophistication. *Nature* **1999**, *397* (6716), 214–215.

(80) Lee, C. Y.; Park, H. S.; Fontecilla-Camps, J. C.; Reisner, E. Photoelectrochemical H_2 Evolution with a Hydrogenase Immobilized on a TiO_2-Protected Silicon Electrode. *Angew. Chem. Int. Ed.* **2016**, *55* (20), 5971–5974.

(81) Alfonta, L.; Zhang, Z.; Uryu, S.; Loo, J. A.; Schultz, P. G. Site-Specific Incorporation of a Redox-Active Amino Acid into Proteins. *J. Am. Chem. Soc.* **2003**, *125* (48), 14662–14663.

(82) Landwehr, M.; Carbone, M.; Otey, C. R.; Li, Y.; Arnold, F. H. Diversification of Catalytic Function in a Synthetic Family of Chimeric Cytochrome P450s. *Chem. Biol.* **2007**, *14* (3), 269–278.

(83) Jones, A. K.; Lichtenstein, B. R.; Dutta, A.; Gordon, G.; Dutton, P. L. Synthetic Hydrogenases: Incorporation of an Iron Carbonyl Thiolate into a Designed Peptide. *J. Am. Chem. Soc.* **2007**, *129*, 14844–14845.

(84) Ugwumba, I. N.; Ozawa, K.; Xu, Z. Q.; Ely, F.; Foo, J. L.; Herlt, A. J.; Coppin, C.; Brown, S.; Taylor, M. C.; Ollis, D. L.; Mander, L. N.; Schenk, G.; Dixon, N. E.; Otting, G.; Oakeshott, J. G.; Jackson, C. J. Improving a Natural Enzyme Activity through Incorporation of Unnatural Amino Acids. *J. Am. Chem. Soc.* **2011**, *133* (2), 326–333.

(85) Dong, Z.; Luo, Q.; Liu, J. Artificial Enzymes Based on Supramolecular Scaffolds. *Chem. Soc. Rev.* **2012**, *41* (23), 7890–7908.

(86) Faiella, M.; Roy, A.; Sommer, D.; Ghirlanda, G. De Novo Design of Functional Proteins: Toward Artificial Hydrogenases. *Biopolymers* **2013**, *100* (6), 558–571.

(87) Roy, S.; Nguyen, T. A. D.; Gan, L.; Jones, A. K. Biomimetic Peptide-Based Models of [FeFe]-Hydrogenases: Utilization of Phosphine-Containing Peptides. *Dalton Trans.* **2015**, *44* (33), 14865–14876.

(88) Mak, W. S.; Tran, S.; Marcheschi, R.; Bertolani, S.; Thompson, J.; Baker, D.; Liao, J. C.; Siegel, J. B. Integrative Genomic Mining for Enzyme Function to Enable Engineering of a Non-Natural Biosynthetic Pathway. *Nat. Commun.* **2015**, *6*, 1–9.

(89) Alcala-Torano, R.; Sommer, D. J.; Bahrami Dizicheh, Z.; Ghirlanda, G. Design Strategies for Redox Active Metalloenzymes: Applications in Hydrogen Production. In *Methods in Enzymology, Volume 580: Peptide, Protein and*

Enzyme Design; Pecoraro, V. L., Ed.; Academic Press: Cambridge, 2016; pp 389–416.

(90)   Sakimoto, K. K.; Kornienko, N.; Yang, P. Cyborgian Material Design for Solar Fuel Production: The Emerging Photosynthetic Biohybrid Systems. *Acc. Chem. Res.* **2017**, *50* (3), 476–481.

(91)   Nocera, D. G. Solar Fuels and Solar Chemicals Industry. *Acc. Chem. Res.* **2017**, *50* (3), 616–619.

(92)   Berggren, G.; Adamska, A.; Lambertz, C.; Simmons, T. R.; Esselborn, J.; Atta, M.; Gambarelli, S.; Mouesca, J. M.; Reijerse, E.; Lubitz, W.; Happe, T.; Artero, V.; Fontecave, M. Biomimetic Assembly and Activation of [FeFe]-Hydrogenases. *Nature* **2013**, *499* (7456), 66–69.

(93)   Slater, J. W.; Marguet, S. C.; Monaco, H. A.; Shafaat, H. S. Going beyond Structure: Nickel-Substituted Rubredoxin as a Mechanistic Model for the [NiFe] Hydrogenases. *J. Am. Chem. Soc.* **2018**, *140* (32), 10250–10262.

(94)   Helm, M. L.; Stewart, M. P.; Bullock, R. M.; Rakowski DuBois, M.; DuBois, D. L. A Synthetic Nickel Electrocatalyst with a Turnover Frequency Above 100,000 s^{-1} for H_2 Production. *Science* **2011**, *333* (6044), 863–866.

(95)   Gross, M. A.; Reynal, A.; Durrant, J. R.; Reisner, E. Versatile Photocatalytic Systems for H_2 Generation in Water Based on an Efficient DuBois-Type Nickel Catalyst. *J. Am. Chem. Soc.* **2014**, *136*, 356–366.

(96)   Das, A. K.; Engelhard, M. H.; Bullock, R. M.; Roberts, J. A. S. A Hydrogen-Evolving $Ni(P_2N_2)_2$ Electrocatalyst Covalently Attached to a Glassy Carbon Electrode: Preparation, Characterization, and Catalysis. Comparisons with the Homogeneous Analogue. *Inorg. Chem.* **2014**, *53* (13), 6875–6885.

(97)   Leung, J. J.; Warnan, J.; Nam, D. H.; Zhang, J. Z.; Willkomm, J.; Reisner, E. Photoelectrocatalytic H_2 Evolution in Water with Molecular Catalysts Immobilised on p-Si *via* a Stabilising Mesoporous TiO_2 Interlayer. *Chem. Sci.* **2017**, *8* (7), 5172–5180.

(98)   Jain, A.; Lense, S.; Linehan, J. C.; Raugei, S.; Cho, H.; Dubois, D. L.; Shaw, W. J. Incorporating Peptides in the Outer-Coordination Sphere of Bioinspired Electrocatalysts for Hydrogen Production. *Inorg. Chem.* **2011**, *50* (9), 4073–4085.

(99)   Jain, A.; Reback, M. L.; Lindstrom, M. Lou; Thogerson, C. E.; Helm, M. L.; Appel, A. M.; Shaw, W. J. Investigating the Role of the Outer-Coordination Sphere in $[Ni(P^{Ph}_2N^{Ph-R}_2)_2]^{2+}$ Hydrogenase Mimics. *Inorg. Chem.* **2012**, *51* (12), 6592–6602.

(100) Reback, M. L.; Ginovska-Pangovska, B.; Ho, M. H.; Jain, A.; Squier, T. C.; Raugei, S.; Roberts, J. A. S.; Shaw, W. J. The Role of a Dipeptide Outer-Coordination Sphere on H_2-Production Catalysts: Influence on Catalytic Rates and Electron Transfer. *Chem. Eur. J.* **2013**, *19*, 1928–1941.

(101) Ginovska-Pangovska, B.; Dutta, A.; Reback, M. L.; Linehan, J. C.; Shaw, W. J. Beyond the Active Site: The Impact of the Outer Coordination Sphere on Electrocatalysts for Hydrogen Production and Oxidation. *Acc. Chem. Res.* **2014**, *47* (8), 2621–2630.

(102) Grunes, J.; Zhu, J.; Somorjai, G. A. Catalysis and Nanoscience. *Chem. Commun.* **2003**, *3* (18), 2257–2260.

(103) Hambourger, M.; Moore, G. F.; Kramer, D. M.; Gust, D.; Moore, A. L.; Moore, T. A. Biology and Technology for Photochemical Fuel Production. *Chem. Soc. Rev.* **2009**, *38* (1), 25–35.

(104) Benson, E. E.; Kubiak, C. P.; Sathrum, A. J.; Smieja, J. M. Electrocatalytic and Homogeneous Approaches to Conversion of CO_2 to Liquid Fuels. *Chem. Soc. Rev.* **2009**, *38* (1), 89–99.

(105) Kamat, P. V.; Tvrdy, K.; Baker, D. R.; Radich, E. J. Beyond Photovoltaics: Semiconductor Nanoarchitectures for Liquid-Junction Solar Cells. *Chem. Rev.* **2010**, *110* (11), 6664–6688.

(106) Kumar, B.; Llorente, M.; Froehlich, J.; Dang, T.; Sathrum, A.; Kubiak, C. P. Photochemical and Photoelectrochemical Reduction of CO_2. *Annu. Rev. Phys. Chem.* **2012**, *63*, 541–569.

(107) Koval, C. A.; Lercher, J.; Scott, S. L. *Basic Research Needs for Catalysis Science to Transform Energy Technologies*; Washington, DC, 2017.

(108) Ye, R.; Zhao, J.; Wickemeyer, B. B.; Toste, F. D.; Somorjai, G. A. Foundations and Strategies of the Construction of Hybrid Catalysts for Optimized Performances. *Nat. Catal.*. Nature Publishing Group May 1, 2018, pp 318–325.

(109) Mizuno, N.; Misono, M. Heterogeneous Catalysis. *Chem. Rev.* **1998**, *98* (1), 199–217.

(110) McKone, J. R.; Marinescu, S. C.; Brunschwig, B. S.; Winkler, J. R.; Gray, H. B. Earth-Abundant Hydrogen Evolution Electrocatalysts. *Chem. Sci.* **2014**, *5* (3), 865–878.

(111) Rakowski DuBois, M.; Du Bois, D. L. The Roles of the First and Second Coordination Spheres in the Design of Molecular Catalysts for H$_2$ Production and Oxidation. *Chem. Soc. Rev.* **2009**, *38* (1), 62–72.

(112) Araki, K.; Wagner, M. J.; Wrighton, M. S. Layer-by-Layer Growth of Electrostatically Assembled Multilayer Porphyrin Films. *Langmuir* **1996**, *12* (22), 5393–5398.

(113) Campbell, W. M.; Jolley, K. W.; Wagner, P.; Wagner, K.; Walsh, P. J.; Gordon, K. C.; Schmidt-Mende, L.; Nazeeruddin, M. K.; Wang, Q.; Grätzel, M.; Officer, D. L. Highly Efficient Porphyrin Sensitizers for Dye-Sensitized Solar Cells. *J. Phys. Chem. C* **2007**, *111* (32), 11760–11762.

(114) Moore, G. F.; Hambourger, M.; Gervaldo, M.; Poluektov, O. G.; Rajh, T.; Gust, D.; Moore, T. A.; Moore, A. L. A Bioinspired Construct That Mimics the Proton Coupled Electron Transfer between P680$^{\bullet+}$ and the Tyr$_z$-His190 Pair of Photosystem II. *J. Am. Chem. Soc.* **2008**, *130* (32), 10466–10467.

(115) Subbaiyan, N. K.; Wijesinghe, C. A.; D'Souza, F. Supramolecular Solar Cells: Surface Modification of Nanocrystalline TiO$_2$ with Coordinating Ligands to Immobilize Sensitizers and Dyads via Metal-Ligand Coordination for Enhanced Photocurrent Generation. *J. Am. Chem. Soc.* **2009**, *131* (41), 14646–14647.

(116) Lindsey, J. S.; Bocian, D. F. Molecules for Charge-Based Information Storage. *Acc. Chem. Res.* **2011**, *44* (8), 638–650.

(117) Moore, G. F.; Blakemore, J. D.; Milot, R. L.; Hull, J. F.; Song, H.; Cai, L.; Schmuttenmaer, C. A.; Crabtree, R. H.; Brudvig, G. W. A Visible Light Water-Splitting Cell with a Photoanode Formed by Codeposition of a High-Potential Porphyrin and an Iridium Water-Oxidation Catalyst. *Energy Environ. Sci.* **2011**, *4* (7), 2389–2392.

(118) Ardo, S.; Achey, D.; Morris, A. J.; Abrahamsson, M.; Meyer, G. J. Non-Nernstian Two-Electron Transfer Photocatalysis at Metalloporphyrin- TiO$_2$ Interfaces. *J. Am. Chem. Soc.* **2011**, *133* (41), 16572–16580.

(119) Auwärter, W.; Écija, D.; Klappenberger, F.; Barth, J. V. Porphyrins at Interfaces. *Nat. Chem.* **2015**, *7* (2), 105–120.

(120) Swierk, J. R.; Méndez-Hernández, D. D.; McCool, N. S.; Liddell, P.; Terazono, Y.; Pahk, I.; Tomlin, J. J.; Oster, N. V.; Moore, T. A.; Moore, A. L.; Gust, D.; Mallouk, T. E. Metal-Free Organic Sensitizers for Use in Water-Splitting Dye-Sensitized Photoelectrochemical Cells. *Proc. Natl. Acad. Sci. U.S.A.* **2015**, *112* (6), 1681–1686.

(121) Civic, M. R.; Dinolfo, P. H. Electrochemical Rectification of Redox Mediators Using Porphyrin-Based Molecular Multilayered Films on ITO Electrodes. *ACS Appl. Mater. Interfaces* **2016**, *8* (31), 20465–20473.

(122) Collin, J. P.; Sauvage, J. P. Electrochemical Reduction of Carbon Dioxide Mediated by Molecular Catalysts. *Coord. Chem. Rev.* **1989**, *93*, 245–268.

(123) Bhugun, I.; Lexa, D.; Savéant, J.-M. Homogeneous Catalysis of Electrochemical Hydrogen Evolution by Iron(0) Porphyrins. *J. Am. Chem. Soc.* **1996**, *118* (16), 3982–3983.

(124) Dhanasekaran, T.; Grodkowski, J.; Neta, P.; Hambright, P.; Fujita, E. *P*-Terphenyl-Sensitized Photoreduction of CO_2 with Cobalt and Iron Porphyrins. Interaction between CO and Reduced Metalloporphyrins. *J. Phys. Chem. A* **1999**, *103* (38), 7742–7748.

(125) Savéant, J.-M. Molecular Catalysis of Electrochemical Reactions. Mechanistic Aspects. *Chem. Rev.* **2008**, *108* (7), 2348–2378.

(126) Morris, A. J.; Meyer, G. J.; Fujita, E. Molecular Approaches to the Photocatalytic Reduction of Carbon Dioxide for Solar Fuels. *Acc. Chem. Res.* **2009**, *42* (12), 1983–1994.

(127) Losse, S.; Vos, J. G.; Rau, S. Catalytic Hydrogen Production at Cobalt Centres. *Coord. Chem. Rev.* **2010**, *254*, 2492–2504.

(128) Lee, C. H.; Dogutan, D. K.; Nocera, D. G. Hydrogen Generation by Hangman Metalloporphyrins. *J. Am. Chem. Soc.* **2011**, *133* (23), 8775–8777.

(129) Roubelakis, M. M.; Bediako, D. K.; Dogutan, D. K.; Nocera, D. G. Proton-Coupled Electron Transfer Kinetics for the Hydrogen Evolution Reaction of Hangman Porphyrins. *Energy Environ. Sci.* **2012**, *5* (7), 7737–7740.

(130) Yao, S. A.; Ruther, R. E.; Zhang, L.; Franking, R. A.; Hamers, R. J.; Berry, J. F. Covalent Attachment of Catalyst Molecules to Conductive Diamond: CO_2 Reduction Using "Smart" Electrodes. *J. Am. Chem. Soc.* **2012**, *134* (38), 15632–15635.

(131) Costentin, C.; Drouet, S.; Robert, M.; Savéant, J.-M. A Local Proton Source Enhances CO_2 Electroreduction to CO by a Molecular Fe Catalyst. *Science* **2012**, *338* (6103), 90–94.

(132) Costentin, C.; Robert, M.; Savéant, J.-M. Catalysis of the Electrochemical Reduction of Carbon Dioxide. *Chem. Soc. Rev.* **2013**, *42* (6), 2423–2436.

(133) Costentin, C.; Robert, M.; Savéant, J.-M. Current Issues in Molecular Catalysis Illustrated by Iron Porphyrins as Catalysts of the CO_2-to-CO Electrochemical Conversion. *Acc. Chem. Res.* **2015**, *48* (12), 2996–3006.

(134) Hod, I.; Sampson, M. D.; Deria, P.; Kubiak, C. P.; Farha, O. K.; Hupp, J. T. Fe-Porphyrin-Based Metal-Organic Framework Films as High-Surface Concentration, Heterogeneous Catalysts for Electrochemical Reduction of CO_2. *ACS Catal.* **2015**, *5* (11), 6302–6309.

(135) Oveisi, A. R.; Zhang, K.; Khorramabadi-zad, A.; Farha, O. K.; Hupp, J. T. Stable and Catalytically Active Iron Porphyrin-Based Porous Organic Polymer: Activity as Both a Redox and Lewis Acid Catalyst. *Sci. Rep.* **2015**, *5*, 10621.

(136) Lin, S.; Diercks, C. S.; Zhang, Y.-B.; Kornienko, N.; Nichols, E. M.; Zhao, Y.; Paris, A. R.; Kim, D.; Yang, P.; Yaghi, O. M.; Chang, C. J. Covalent Organic Frameworks Comprising Cobalt Porphyrins for Catalytic CO_2 Reduction in Water. *Science* **2015**, *349* (6253), 1208–1213.

(137) Weng, Z.; Jiang, J.; Wu, Y.; Wu, Z.; Guo, X.; Materna, K. L.; Liu, W.; Batista, V. S.; Brudvig, G. W.; Wang, H. Electrochemical CO_2 Reduction to Hydrocarbons on a Heterogeneous Molecular Cu Catalyst in Aqueous Solution. *J. Am. Chem. Soc.* **2016**, *138* (26), 8076–8079.

(138) Azcarate, I.; Costentin, C.; Robert, M.; Savéant, J.-M. Through-Space Charge Interaction Substituent Effects in Molecular Catalysis Leading to the Design of the Most Efficient Catalyst of CO_2-to-CO Electrochemical Conversion. *J. Am. Chem. Soc.* **2016**, *138* (51), 16639–16644.

(139) Beiler, A. M.; Khusnutdinova, D.; Wadsworth, B. L.; Moore, G. F. Cobalt Porphyrin-Polypyridyl Surface Coatings for Photoelectrosynthetic Hydrogen Production. *Inorg. Chem.* **2017**, *56* (20), 12178–12185.

(140) Khusnutdinova, D.; Beiler, A. M.; Wadsworth, B. L.; Jacob, S. I.; Moore, G. F. Metalloporphyrin-Modified Semiconductors for Solar Fuel Production. *Chem. Sci.* **2017**, *8* (1), 253–259.

(141) Bullock, R. M.; Das, A. K.; Appel, A. M. Surface Immobilization of Molecular Electrocatalysts for Energy Conversion. *Chem. Eur. J.* **2017**, *23* (32), 7626–7641.

(142) Vesborg, P. C. K.; Jaramillo, T. F. Addressing the Terawatt Challenge: Scalability in the Supply of Chemical Elements for Renewable Energy. *RSC Adv.* **2012**, *2* (21), 7933–7947.

(143) Friedman, D.; Masciangioli, T.; Olson, S. *The Role of the Chemical Sciences in Finding Alternatives to Critical Resources: A Workshop Summary*; National Academies Press, 2012.

(144) Wiese, S.; Kilgore, U. J.; Ho, M.-H.; Raugei, S.; Dubois, D. L.; Bullock, R. M.; Helm, M. L. Hydrogen Production Using Nickel Electrocatalysts with Pendant Amines: Ligand Effects on Rates and Overpotentials. *ACS Catal.* **2013**, *3* (11), 2527–2535.

(145) Bacchi, M.; Berggren, G.; Niklas, J.; Veinberg, E.; Mara, M. W.; Shelby, M. L.; Poluektov, O. G.; Chen, L. X.; Tiede, D. M.; Cavazza, C.; Field, M. J.; Fontecave, M.; Artero, V. Cobaloxime-Based Artificial Hydrogenases. *Inorg. Chem.* **2014**, *53* (15), 8071–8082.

(146) Queyriaux, N.; Kaeffer, N.; Morozan, A.; Chavarot-Kerlidou, M.; Artero, V. Molecular Cathode and Photocathode Materials for Hydrogen Evolution in Photoelectrochemical Devices. *J. Photochem. Photobiol. C: Photochem. Rev.* **2015**, *25*, 90–105.

(147) Dutta, A.; Ginovska, B.; Raugei, S.; Roberts, J. A. S.; Shaw, W. J. Optimizing Conditions for Utilization of an H_2 Oxidation Catalyst with Outer Coordination Sphere Functionalities. *Dalton Trans.* **2016**, *45* (24), 9786–9793.

(148) Tsay, C.; Yang, J. Y. Electrocatalytic Hydrogen Evolution under Acidic Aqueous Conditions and Mechanistic Studies of a Highly Stable Molecular Catalyst. *J. Am. Chem. Soc.* **2016**, *138* (43), 14174–14177.

(149) Maher, A. G.; Passard, G.; Dogutan, D. K.; Halbach, R. L.; Anderson, B. L.; Gagliardi, C. J.; Taniguchi, M.; Lindsey, J. S.; Nocera, D. G. Hydrogen Evolution Catalysis by a Sparsely Substituted Cobalt Chlorin. *ACS Catal.* **2017**, *7* (5), 3597–3606.

(150) Lin, V. S.-Y.; DiMagno, S. G.; Therien, M. J. Highly Conjugated, Acetylenyl Bridged Porphyrins: New Models for Light-Harvesting Antenna Systems. *Science* **1994**, *264* (5162), 1105–1111.

(151) Anderson, H. L. Building Molecular Wires from the Colours of Life: Conjugated Porphyrin Oligomers. *Chem. Commun.* **1999**, *23*, 2323–2330.

(152) Tsuda, A.; Furuta, H.; Osuka, A. Completely Fused Diporphyrins and Triporphyrin. *Angew. Chem.* **2000**, *112* (14), 2649–2652.

(153) Tsuda, A.; Osuka, A. Fully Conjugated Porphyrin Tapes with Electronic Absorption Bands That Reach into Infrared. *Science* **2001**, *293* (5527), 79–82.

(154) Kim, D.; Osuka, A. Photophysical Properties of Directly Linked Linear Porphyrin Arrays. *J. Phys. Chem. A* **2003**, *107* (42), 8791–8816.

(155) Cheng, F.; Zhang, S.; Adronov, A.; Echegoyen, L.; Diederich, F. Triply Fused Zn^{II}-Porphyrin Oligomers: Synthesis, Properties, and Supramolecular Interactions with Single-Walled Carbon Nanotubes (SWNTs). *Chem. Eur. J.* **2006**, *12* (23), 6062–6070.

(156) Tanaka, T.; Lee, B. S.; Aratani, N.; Yoon, M.-C.; Kim, D.; Osuka, A. Synthesis and Properties of Hybrid Porphyrin Tapes. *Chem. Eur. J.* **2011**, *17* (51), 14400–14412.

(157) Brennan, B. J.; Arero, J.; Liddell, P. A.; Moore, T. A.; Moore, A. L.; Gust, D. Selective Oxidative Synthesis of *Meso*-Beta Fused Porphyrin Dimers. *J. Porphyr. Phthalocyanines* **2013**, *17* (4), 247–251.

(158) Dimé, A. K. D.; Devillers, C. H.; Cattey, H.; Lucas, D. Versatile Redox Reactivity of Triaryl-*Meso*-Substituted Ni(II) Porphyrin. *Dalton Trans.* **2014**, *43* (39), 14554–14564.

(159) Feng, C.-M.; Zhu, Y.-Z.; Zhang, S.-C.; Zang, Y.; Zheng, J.-Y. Synthesis of Directly Fused Porphyrin Dimers through Fe(OTf)$_3$-Mediated Oxidative Coupling. *Org. Biomol. Chem.* **2015**, *13* (9), 2566–2569.

(160) Tanaka, T.; Osuka, A. Conjugated Porphyrin Arrays: Synthesis, Properties and Applications for Functional Materials. *Chem. Soc. Rev.* **2015**, *44* (4), 943–969.

(161) Pegis, M. L.; McKeown, B. A.; Kumar, N.; Lang, K.; Wasylenko, D. J.; Zhang, X. P.; Raugei, S.; Mayer, J. M. Homogenous Electrocatalytic Oxygen Reduction Rates Correlate with Reaction Overpotential in Acidic Organic Solutions. *ACS Cent. Sci.* **2016**, *2* (11), 850–856.

(162) Costentin, C.; Savéant, J.-M. Towards an Intelligent Design of Molecular Electrocatalysis. *Nat. Rev. Chem.* **2017**, *1*, 0087.

(163) Barry, B. A.; Babcock, G. T. Tyrosine Radicals Are Involved in the Photosynthetic Oxygen-Evolving System. *Proc. Natl. Acad. Sci. U.S.A.* **1987**, *84* (20), 7099–7103.

(164) Tommos, C.; Babcock, G. T. Proton and Hydrogen Currents in Photosynthetic Water Oxidation. *Biochim Biophys Acta* **2000**, *1458* (1), 199–219.

(165) Vogt, L.; Vinyard, D. J.; Khan, S.; Brudvig, G. W. Oxygen-Evolving Complex of Photosystem II: An Analysis of Second-Shell Residues and Hydrogen-Bonding Networks. *Curr. Opin. Chem. Biol.* **2015**, *25*, 152–158.

(166) Hammarström, L.; Wasielewski, M. R. Biomimetic Approaches to Artificial Photosynthesis. *Energy Environ. Sci.* **2011**, *4* (7), 2339.

(167) Hammes-Schiffer, S. Theoretical Perspectives on Proton-Coupled Electron Transfer Reactions. *Acc. Chem. Res.* **2001**, *34* (4), 273–281.

(168) Stubbe, J.; Nocera, D. G.; Yee, C. S.; Chang, M. C. Y. Radical Initiation in the Class I Ribonucleotide Reductase: Long-Range Proton-Coupled Electron Transfer? *Chem. Rev.* **2003**, *103* (6), 2167–2201.

(169) Agmon, N. The Grotthuss Mechanism. *Chem. Phys. Lett.* **1995**, *244* (5–6), 456–462.

(170) Bondar, A.-N.; Dau, H. Extended Protein/Water H-Bond Networks in Photosynthetic Water Oxidation. *Biochim. Biophys. Acta.* **2012**, *1817* (8), 1177–1190.

(171) Burdinski, D.; Wieghardt, K.; Steenken, S. Intramolecular Electron Transfer from Mn or Ligand Phenolate to Photochemically Generated Ru^{III} in Multinuclear Ru/Mn Complexes. Laser Flash Photolysis and EPR Studies on Photosystem II Models. *J. Am. Chem. Soc.* **1999**, *121* (46), 10781–10787.

(172) Sjödin, M.; Styring, S.; Åkermark, B.; Sun, L.; Hammarström, L. Proton-Coupled Electron Transfer from Tyrosine in a Tyrosine-Ruthenium-Tris-Bipyridine Complex: Comparison with Tyrosine$_z$ Oxidation in Photosystem II. *J. Am. Chem. Soc.* **2000**, *122* (16), 3932–3936.

(173) Maki, T.; Araki, Y.; Ishida, Y.; Onomura, O.; Matsumura, Y. Construction of Persistent Phenoxyl Radical with Intramolecular Hydrogen Bonding. *J. Am. Chem. Soc.* **2001**, *123* (14), 3371–3372.

(174) Benisvy, L.; Bill, E.; Blake, A. J.; Collison, D.; Davies, E. S.; Garner, C. D.; Guindy, C. I.; McInnes, E. J. L.; McArdle, G.; McMaster, J.; Wilson, C.; Wolowska, J. Phenolate and Phenoxyl Radical Complexes of Co(II) and Co(III). *Dalton Trans.* **2004**, No. 21, 3647–3653.

(175) Rhile, I. J.; Mayer, J. M. One-Electron Oxidation of a Hydrogen-Bonded Phenol Occurs by Concerted Proton-Coupled Electron Transfer. *J. Am. Chem. Soc.* **2004**, *126* (40), 12718–12719.

(176) Lachaud, F.; Quaranta, A.; Pellegrin, Y.; Dorlet, P.; Charlot, M. F.; Un, S.; Leibl, W.; Aukaulo, A. A Biomimetic Model of the Electron Transfer between P$_{680}$ and the TyrZ-His190 Pair of PSII. *Angew. Chem. Int. Ed.* **2005**, *44* (10), 1536–1540.

(177) Costentin, C.; Robert, M.; Savéant, J.-M. Electrochemical and Homogeneous Proton-Coupled Electron Transfers: Concerted Pathways in the One-Electron Oxidation of a Phenol Coupled with an Intramolecular Amine-Driven Proton Transfer. *J. Am. Chem. Soc.* **2006**, *128* (14), 4552–4553.

(178) Rhile, I. J.; Markle, T. F.; Nagao, H.; DiPasquale, A. G.; Lam, O. P.; Lockwood, M. A.; Rotter, K.; Mayer, J. M. Concerted Proton-Electron Transfer in the Oxidation of Hydrogen-Bonded Phenols. *J. Am. Chem. Soc.* **2006**, *128* (18), 6075–6088.

(179) Lomoth, R.; Magnuson, A.; Sjödin, M.; Huang, P.; Styring, S.; Hammarström, L. Mimicking the Electron Donor Side of Photosystem II in Artificial Photosynthesis. *Photosynth. Res.* **2006**, *87*, 25–40.

(180) Costentin, C.; Louault, C.; Robert, M.; Savéant, J.-M. Evidence for Concerted Proton-Electron Transfer in the Electrochemical Oxidation of Phenols with Water as Proton Acceptor. Tri-*Tert*-Butylphenol. *J. Am. Chem. Soc.* **2008**, *130* (47), 15817–15819.

(181) Moore, G. F.; Hambourger, M.; Kodis, G.; Michl, W.; Gust, D.; Moore, T. A.; Moore, A. L. Effects of Protonation State on a Tyrosine-Histidine Bioinspired Redox Mediator. *J. Phys. Chem. B* **2010**, *114* (45), 14450–14457.

(182) Megiatto, J. D.; Antoniuk-Pablant, A.; Sherman, B. D.; Kodis, G.; Gervaldo, M.; Moore, T. A.; Moore, A. L.; Gust, D. Mimicking the Electron Transfer Chain in Photosystem II with a Molecular Triad Thermodynamically Capable of Water Oxidation. *Proc. Natl. Acad. Sci. U.S.A.* **2012**, *109* (39), 15578–15583.

(183) Megiatto, J. D.; Méndez-Hernández, D. D.; Tejeda-Ferrari, M. E.; Teillout, A.-L.; Llansola-Portolés, M. J.; Kodis, G.; Poluektov, O. G.; Rajh, T.; Mujica, V.; Groy, T. L.; Gust, D.; Moore, T. A.; Moore, A. L. A Bioinspired Redox Relay That Mimics Radical Interactions of the Tyr–His Pairs of Photosystem II. *Nat. Chem.* **2014**, *6*, 423–428.

(184) Ravensbergen, J.; Antoniuk-Pablant, A.; Sherman, B. D.; Kodis, G.; Megiatto, J. D.; Méndez-Hernández, D. D.; Frese, R. N.; Van Grondelle, R.; Moore, T. A.; Moore, A. L.; Gust, D.; Kennis, J. T. M. Spectroscopic Analysis of a Biomimetic Model of Tyr$_Z$ Function in PSII. *J. Phys. Chem. B* **2015**, *119* (37), 12156–12163.

(185) Odella, E.; Mora, S. J.; Wadsworth, B. L.; Huynh, M. T.; Goings, J. J.; Liddell, P. A.; Groy, T. L.; Gervaldo, M.; Sereno, L. E.; Gust, D.; Moore, T. A.; Moore, G. F.; Hammes-Schiffer, S.; Moore, A. L. Controlling Proton-Coupled Electron Transfer in Bioinspired Artificial Photosynthetic Relays. *J. Am. Chem. Soc.* **2018**, *140* (45), 15450–15460.

(186) Mora, S. J.; Heredia, D. A.; Odella, E.; Vrudhula, U.; Gust, D.; Moore, T. A.; Moore, A. L. Design and Synthesis of Benzimidazole Phenol-Porphyrin Dyads for the Study of Bioinspired Photoinduced Proton-Coupled Electron Transfer. *J. Porphyr. Phthalocyanines* **2019**, *23* (11n12), 1336–1345.

(187) Odella, E.; Wadsworth, B. L.; Mora, S. J.; Goings, J. J.; Huynh, M. T.; Gust, D.; Moore, T. A.; Moore, G. F.; Hammes-Schiffer, S.; Moore, A. L. Proton-Coupled Electron Transfer Drives Long-Range Proton Translocation in Bioinspired Systems. *J. Am. Chem. Soc.* **2019**, *141* (36), 14057–14061.

(188) Parada, G. A.; Goldsmith, Z. K.; Kolmar, S.; Pettersson Rimgard, B.; Mercado, B. Q.; Hammarström, L.; Hammes-Schiffer, S.; Mayer, J. M. Concerted Proton-Electron Transfer Reactions in the Marcus Inverted Region. *Science* **2019**, *364* (6439), 471–475.

(189) Wang, D.; Sampaio, R. N.; Troian-Gautier, L.; Marquard, S. L.; Farnum, B. H.; Sherman, B. D.; Sheridan, M. V.; Dares, C. J.; Meyer, G. J.; Meyer, T. J. Molecular Photoelectrode for Water Oxidation Inspired by Photosystem II. *J. Am. Chem. Soc.* **2019**, *141* (19), 7926–7933.

(190) Odella, E.; Mora, S. J.; Wadsworth, B. L.; Goings, J. J.; Gervaldo, M. A.; Sereno, L. E.; Groy, T. L.; Gust, D.; Moore, T. A.; Moore, G. F.; Hammes-Schiffer, S.; Moore, A. L. Proton-Coupled Electron Transfer across Benzimidazole Bridges in Bioinspired Proton Wires. *Chem. Sci.* **2020**, *11* (15), 3820–3828.

(191) Guerra, W. D.; Odella, E.; Secor, M.; Goings, J. J.; Urrutia, M. N.; Wadsworth, B. L.; Gervaldo, M.; Sereno, L. E.; Moore, T. A.; Moore, G. F.; Hammes-Schiffer, S.; Moore, A. L. Role of Intact Hydrogen-Bond Networks in Multiproton-Coupled Electron Transfer. *J. Am. Chem. Soc.* **2020**, *142* (52), 21842–21851.

(192) Yoneda, Y.; Mora, S. J.; Shee, J.; Wadsworth, B. L.; Arsenault, E. A.; Hait, D.; Kodis, G.; Gust, D.; Moore, G. F.; Moore, A. L.; Head-Gordon, M.; Moore, T. A.; Fleming, G. R. Electron-Nuclear Dynamics Accompanying Proton-Coupled Electron Transfer. *J. Am. Chem. Soc.* **2021**, *143* (8), 3104–3112.

(193) Sayre, H.; Ripberger, H. H.; Odella, E.; Zieleniewska, A.; Heredia, D. A.; Rumbles, G.; Scholes, G. D.; Moore, T. A.; Moore, A. L.; Knowles, R. R. PCET-Based Ligand Limits Charge Recombination with an Ir(III) Photoredox Catalyst. *J. Am. Chem. Soc.* **2021**, *143* (33), 13034–13043.

(194) Odella, E.; Secor, M.; Elliott, M.; Groy, T. L.; Moore, T. A.; Hammes-Schiffer, S.; Moore, A. L. Multi PCET in Symmetrically Substituted Benzimidazoles. *Chem. Sci.* **2021**, *12* (38), 12667–12675.

(195) Guerra, W. D.; Odella, E.; Urrutia, M. N.; Liddell, P. A.; Moore, T. A.; Moore, A. L. Models to Study Photoinduced Multiple Proton Coupled Electron Transfer Processes. *J. Porphyr. Phthalocyanines* **2021**, *25* (07n08), 674–682.

(196) Huynh, M. T.; Mora, S. J.; Villalba, M.; Tejeda-Ferrari, M. E.; Liddell, P. A.; Cherry, B. R.; Teillout, A.-L.; Machan, C. W.; Kubiak, C. P.; Gust, D.; Moore, T. A.; Hammes-Schiffer, S.; Moore, A. L. Concerted One-Electron Two-Proton Transfer Processes in Models Inspired by the Tyr-His Couple of Photosystem II. *ACS Cent. Sci.* **2017**, *3* (5), 372–380.

CHAPTER 2

SIX-ELECTRON CHEMISTRY OF A BINUCLEAR IRON(III) FUSED PORPHYRIN

Portions of this chapter are excerpted and reprinted with permission from:

2.1 Introduction

Monometallic porphyrins are relatively well-studied electrocatalysts for the HER, oxygen reduction (ORR), and CO_2RR.[1–3] This includes pioneering work by Savéant[4] and coworkers on the use of iron porphyrins for CO_2RR[5–8] and HER.[9] In these studies, structural modification of the phenyl substituents at the periphery of the porphyrin ring,[10–12] to include groups such as dihydroxyphenyl,[13] pentafluorophenyl,[14] trimethylanilinium,[15] or sulfonatophenyl,[16] have enabled an improved understanding of mechanistic details governing the electrocatalytic performance of these assemblies.[17] In addition, the benchmarking of both homogeneous[18,19] and heterogeneous[20] catalysts via Tafel plots[21] and/or foot-of-the-wave analysis have established approaches for comparing intrinsic catalytic properties that are independent of the characteristics of an electrochemical cell.

Since their serendipitous discovery by Sugiura and Sakata,[22] multinuclear fused porphyrins have also been fairly well studied due, in part, to the unique optical properties resulting from their extended aromaticity. They have been used in applications involving non-linear optic materials, molecular wires, and supramolecular chemistry.[23,24] Nonetheless, fused porphyrins, and related porphyrinoids featuring extended aromaticity, have not been as extensively studied for applications in electrocatalysis.[25,26] Further, although there are reported examples of doubly- and triply-fused dimers, trimers, and oligomeric porphyrin arrays containing Mg,[27] Co,[28] Ni,[22,29–42] Cu,[34–36,38–40,43–47] Zn,[28,30,31,36,38–40,44,45,47-57] Ru,[58] Pd,[29,34–36,38,50] Ag,[46] Pb,[57] Y,[59] and Tb,[59] this work describes analogous multinuclear Fe fused porphyrin complexes, which could be useful for applications in electrocatalysis.

In this chapter, the synthesis and electrochemical as well as spectroscopic characterization of a novel binuclear Fe(III) fused porphyrin (**Fe₂FPCl₂**) (Figure 2.1) is reported. Ultraviolet-visible spectroscopy confirms the extended electronic structure of this 36 π-aromatic macrocycle. In addition, Fourier transform infrared spectroscopy indicates the Fe centers experience a relatively rigid ligand environment as compared to a structurally related mononuclear complex featuring an 18 π-aromatic porphyrin ligand. X-ray photoelectron and X-ray absorption near edge spectroscopies confirm the iron centers of both assemblies are Fe(III) in the as prepared, resting state. In comparison with the mononuclear porphyrin, electrochemical measurements show there is a doubling of the number of redox events associated with the fused, binuclear complex. In summary, features of the fused-iron-porphyrin include: 1) bimetallic-iron sites, 2) a π-extended ligand environment capable of delocalizing electrons across the multimetallic scaffold, and 3) the ability to store up to six electrons.
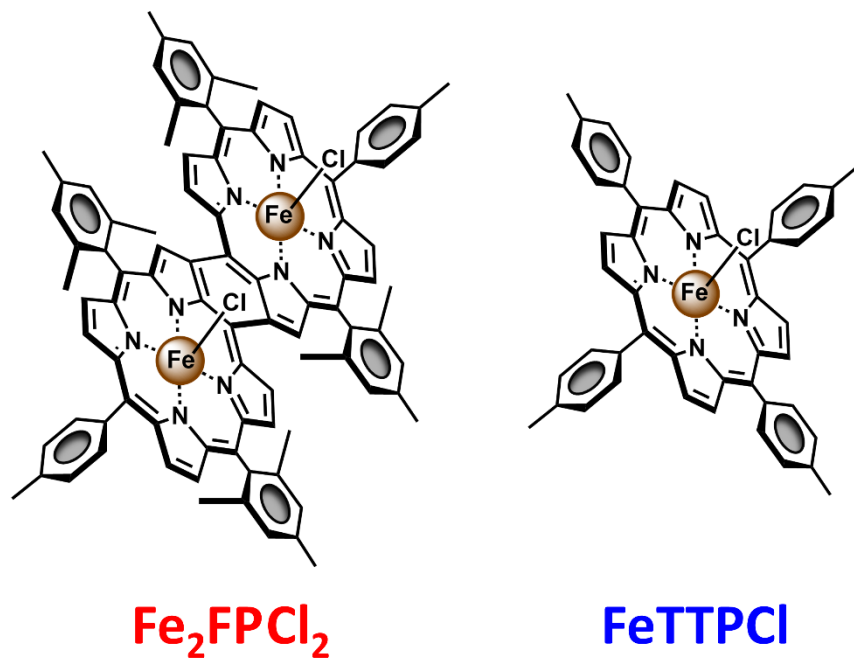
Fe₂FPCl₂   **FeTTPCl**

Figure 2.1 Molecular structures of **Fe₂FPCl₂** (left) and **FeTTPCl** (right).

2.2 Results and Discussion

2.2.1 Materials Preparation

Fe₂FPCl₂ was prepared via an 8-step synthetic route following the pathway indicated in Figure 2.2. The monometallic model compound, **FeTTPCl** (Figure 2.1), was synthesized following a previously reported method.[60] The free-base porphyrin ligands used for preparing **Fe₂FPCl₂** and **FeTTPCl** (**FP** and **TTP**, respectively) were characterized via matrix-assisted laser desorption/ionization time-of-flight mass spectrometry (MALDI-TOF MS) (Figure 4.1 and Figure 4.3), as well as ultraviolet-visible (UV-Vis) (Figure 4.5
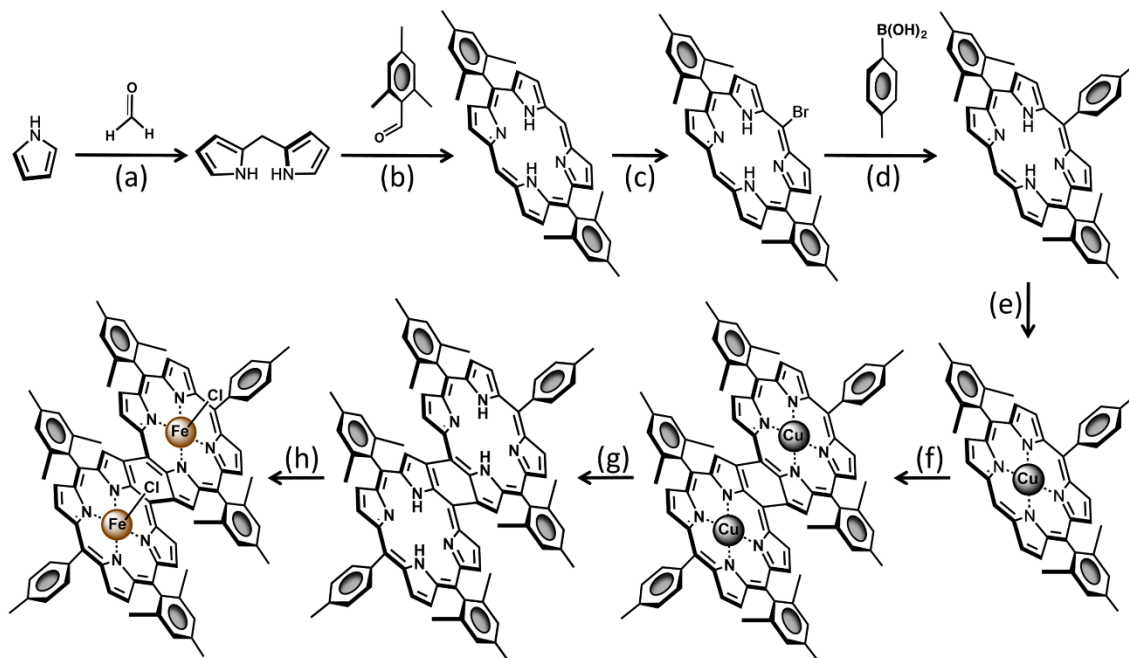
Figure 2.2 Synthetic route for preparing **Fe₂FPCl₂**: (a) TFA, 50 °C, 5 min. (b) 1. BF₃·Et₂O, CHCl₃, rt, 30 min. 2. DDQ, reflux, 1 h. (c) NBS, Pyridine, CHCl₃, 0 °C, 20 min. (d) p-Tolylboronic acid, K_3PO_4, Pd(PPh₃)₄, Tol:H₂O:Methanol, reflux, overnight. (e) CuAc₂, DCM:Methanol, reflux, overnight. (f) Cu(BF₄)₂·6H₂O, MeNO₂, rt, 2 h. (g) TFA:H₂SO₄, rt, 20 min. (h) FeCl₂·4H₂O, DCM:Methanol, reflux, overnight. All reactions were performed under Ar atmosphere.

and Figure 4.7), Fourier transform infrared (FTIR) (Figure 4.10 and Figure 4.11), and Nuclear Magnetic Resonance (NMR) spectroscopies (Figure 4.13 and Figure 4.14). Successful metal insertion was confirmed using MALDI-TOF spectrometry (Figure 4.2 and Figure 4.4), as well as UV-Vis (Figure 2.3a) and FTIR spectroscopies (Figure 2.3b). In addition, both X-ray photoelectron spectroscopy (XPS) (Figure 2.4a) and X-ray absorption near-edge spectroscopy (XANES) (Figure 2.4b) indicate a +3 oxidation state of the Fe centers in both **Fe₂FPCl₂** and **FeTTPCl.**

2.2.2 UV-Vis-NIR and FTIR Characterization

Unlike the electronic absorption spectrum of **FeTTPCl** shown in Figure 2.3a and recorded in *N*,*N*-dimethylformamide (DMF), which displays a single Soret-band transition centered at 418 nm and three Q-band transitions centered at 510 nm, 573 nm, and 695 nm, the spectrum of **Fe₂FPCl₂** in DMF displays two Soret-like absorption bands
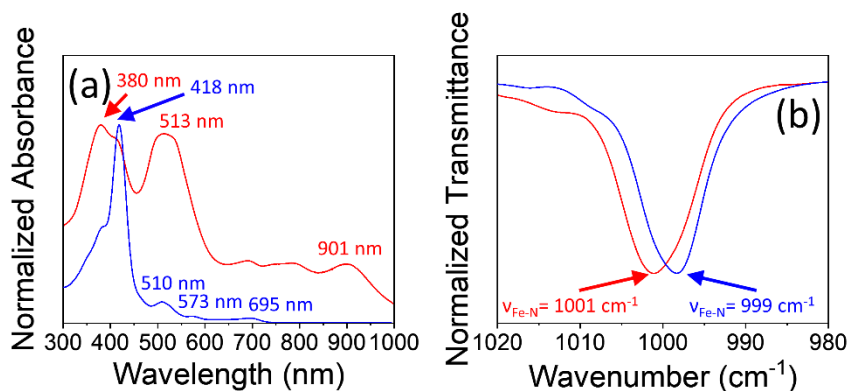
Figure 2.3 (a) Normalized absorption spectra of **Fe₂FPCl₂** (red) and **FeTTPCl** (blue) recorded in DMF. (b) Normalized FTIR transmission spectra of **Fe₂FPCl₂** (red) and **FeTTPCl** (blue) recorded in pressed KBr pellets.

centered at 380 nm and 513 nm, as well as a Q-type absorption feature at 901 nm (Figure 2.3a). The relatively red absorption features associated with **Fe₂FPCl₂** versus **FeTTPCl**

40

are consistent with the extended aromaticity of the fused architecture (*i.e.*, a 36 π-aromatic ligand versus an 18 π-aromatic ligand). Absorption spectra recorded in dichloromethane (CH_2Cl_2), benzonitrile (C_6H_5CN), and butyronitrile (C_3H_7CN), along with information on the wavelengths of the Soret and Q-type absorption bands, are included in Chapter 4.2 (Figure 4.6, Figure 4.8, Table 4.1 and Table 4.2).

FTIR data collected using a matrix of KBr containing either **FeTTPCl** or **Fe₂FPCl₂** show distinct transmission bands centered at 999 cm^{-1} and 1001 cm^{-1}, respectively (Figure 2.3b). These bands are assigned to an in-plane porphyrin deformation vibration (ν_{Fe-N}, where ν is the vibrational frequency). In general, this vibrational mode is sensitive to both the elemental nature of the porphyrin metal center and its local coordination environment.[61–64] For these reasons, in-plane porphyrin deformation vibrations have been used as diagnostic signals for indicating the presence of metalloporphyrins on surfaces and gaining information on their local chemical environments.[25,60,65–68] The difference in ν_{Fe-N} frequencies of **FeTTPCl** and **Fe₂FPCl₂** suggests the fused complex provides a more rigid ligand motif. Similar observations have been noted in comparisons of FTIR spectra collected using bimetallic copper fused porphyrins versus analogous monometallic copper porphyrins (Figure 4.12).[25]

2.2.3 XP and XANE Spectroscopy Studies

High resolution Fe core level XP spectra collected using either samples of the fused or monomeric complexes display peaks centered at 709.8 eV ($2p_{3/2}$) and 723.3 eV ($2p_{1/2}$) in the case of **Fe₂FPCl₂**, and peaks centered at 709.8 eV ($2p_{3/2}$) and 724.4 eV ($2p_{1/2}$) in the case of **FeTTPCl** (Figure 2.4a). These results are consistent with Fe(III) oxidation states for the metal centers of these overall charge neutral complexes, where **Fe₂FPCl₂** features
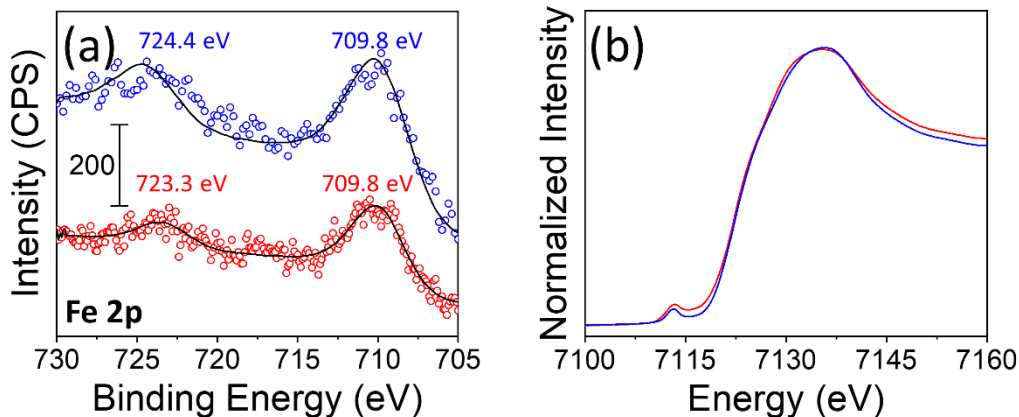
Figure 2.4 (a) High energy resolution core level XP spectra of the Fe 2p region recorded using samples of **Fe₂FPCl₂** (red) or **FeTTPCl** (blue) dropcasted onto a glassy carbon disk. The solid black lines are the component fits. (b) XANES spectra at the Fe K-edge of **Fe₂FPCl₂** (red) and **FeTTPCl** (blue).

two anionic (X-type) chloride ligands, four anionic (X-type) nitrogen ligand sites, and four charge-neutral (L-type) nitrogen ligand sites, whereas **FeTTPCl** features one anionic (X-type) chloride ligand, two anionic (X-type) nitrogen ligand sites, and two charge-neutral (L-type) nitrogen ligand sites. In addition, XANES indicates similar edge energies for the fused and non-fused complexes (Figure 2.4b), with values that are intermediate to those recorded using $FeCl_2$ (Fe^{II}) and Fe_2O_3 (Fe^{III}) as reference compounds (Figure 4.15). The positions of the main and pre-edge features recorded using samples of **Fe₂FPCl₂** match those previously reported for Fe(III) tetraphenyl porphyrin.[69] However, in the case of the fused complex, the pre-edge region displays a higher intensity peak, indicating a slightly more distorted geometry around the iron centers of **Fe₂FPCl₂**.[70]

2.2.4 Electrochemical Studies

In this work we describe the redox states of the binuclear Fe fused porphyrin and the

structurally related mononuclear complex using the monikers $[Fe_2FP]^n$ and $[FeTTP]^n$ respectively, where n gives information on the relative number of electrons transferred to or from the charge neutral **[Fe₂FP]**^{0} or **[FeTTP]**^{0} metalloporphyrin complexes. Electrochemical potentials associated with the interconversion between the **[Fe₂FP]**$^{2+}$ through **[Fe₂FP]**$^{4-}$ redox states were determined using both cyclic voltammetry and differential pulse voltammetry (Figure 2.5). Related measurements using **[FeTTP]Cl** and involving the interconversion between the **[FeTTP]**$^{1+}$ through **[FeTTP]**$^{2-}$ redox states, are included for comparison.

Voltammograms recorded using **Fe₂FPCl₂** (1.0 mM) dissolved in 0.1 M tetrabutylammonium hexafluorophosphate (TBAPF₆) in DMF, indicate a pair of
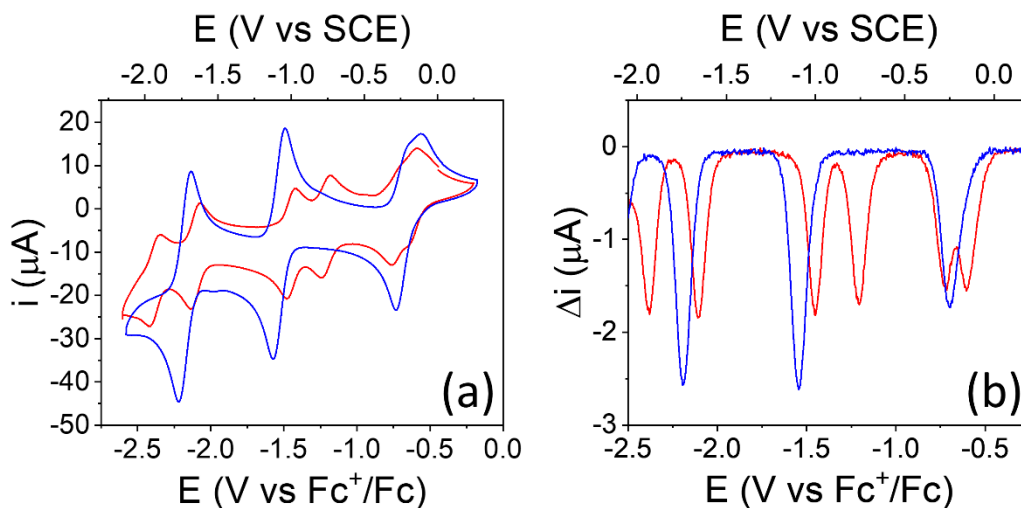
Figure 2.5 (a) Cyclic voltammograms of 1.0 mM **Fe₂FPCl₂** (red) and **FeTTPCl** (blue) recorded in a 0.1 M TBAPF₆ DMF solution under argon at a scan rate of 250 mV s^{-1}. (b) Differential pulse voltammetry data of the same solutions recorded with a pulse height of 2.5 mV, a pulse width of 100 ms, a step height of -5 mV, and a step time of 500 ms. All measurements were recorded using a 3 mm diameter glassy carbon WE at room temperature and the ferrocenium/ferrocene redox couple as an internal reference.

43

overlapping redox features appearing between the range of -0.50 and -0.80 V versus the ferrocenium/ferrocene (V vs Fc$^+$/Fc) redox couple. These features are assigned to a pair of chemically and electrochemically irreversible couples, where the chemical irreversibility is likely due to loss of X-type chloride ligands following reduction of the porphyrin complexes.[71,72] In addition, two pairs of quasi-reversible redox couples are observed at more negative potentials with midpoint potentials ($E_{1/2}$) equal to -1.21, -1.46, -2.11, and -2.40 V vs Fc$^+$/Fc, respectively (where $^nE_{1/2}$ is estimated as the average of anodic and cathodic peak potentials for a given quasi-reversible redox couple and $^{III}E_{1/2}$, $^{IV}E_{1/2}$, $^VE_{1/2}$, and $^{VI}E_{1/2}$ are reported as reduction half reactions by convention)[73] (Figure 2.5a). For comparison, when measured under otherwise similar experimental conditions, cyclic voltammograms recorded using **FeTTPCl** display one non-reversible redox feature appearing between the range of -0.50 and -0.80 V vs Fc$^+$/Fc, as well as two quasi-reversible redox couples with midpoint potentials ($^{II}E_{1/2}$ and $^{III}E_{1/2}$) equal to -1.53 V vs Fc$^+$/Fc and -2.18 V vs Fc$^+$/Fc respectively (Figure 2.5a).

The midpoint potentials, and peak potentials in the case of non-reversible redox features, recorded using **Fe$_2$FPCl$_2$** or **FeTTPCl** in DMF are summarized in Table 2.1 and Table 2.2. Table 4.3 includes cathodic peak potentials determined using differential pulse voltammetry (Figure 2.5b), which enables resolution of the overlapping redox waves associated with the conversion of **[Fe$_2$FP]$^{2+}$** to **[Fe$_2$FP]$^{1+}$** and **[Fe$_2$FP]$^{1+}$** to **[Fe$_2$FP]^0**. The height of the peaks corresponding to reductions from **[Fe$_2$FP]^0** to **[Fe$_2$FP]$^{4-}$** are approximately equal in value (Figure 2.5b), consistent with each reduction process being attributed to one-electron chemistry. The slightly lower peak height (~90 % lower) for the peaks corresponding to reductions from **[Fe$_2$FP]$^{2+}$** to **[Fe$_2$FP]^0** are attributed to sluggish

heterogeneous electron-transfer kinetics (electrochemical irreversibility) and/or

dissociation of Cl$^-$ ligands following the reduction of iron centers (chemical

irreversibility), both of which could result in a larger peak width and lower peak

intensity.[74] Cyclic voltammograms recorded in other solvents, including CH$_2$Cl$_2$,

C$_6$H$_5$CN, and C$_3$H$_7$CN, along with information on the related midpoint and peak

potentials, are included in Figure 2.6, Table 2.1, and Table 2.2.
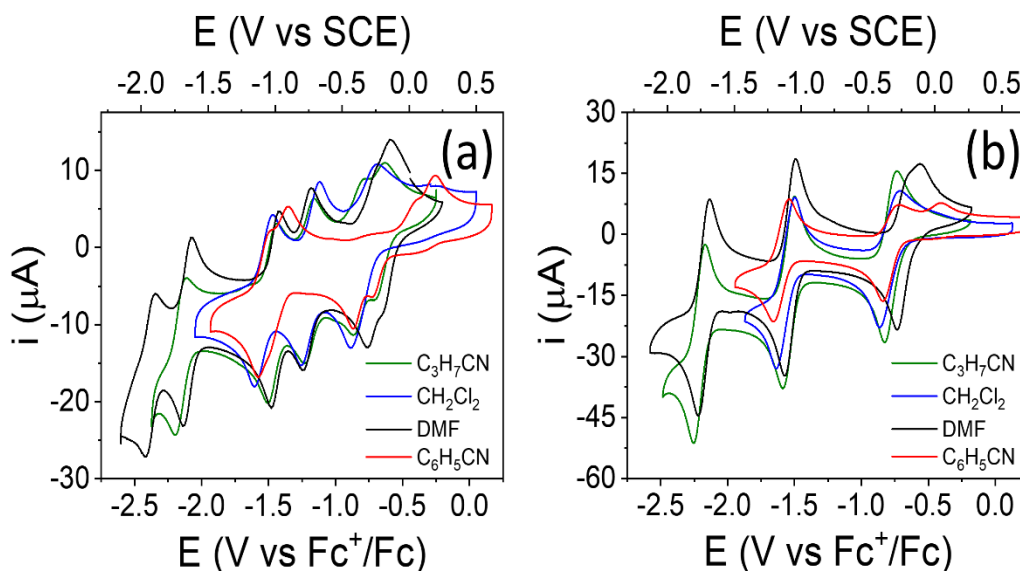
Figure 2.6 (a) Cyclic voltammograms recorded using **Fe$_2$FPCl$_2$** (1 mM) and TBAPF$_6$ (0.1

M) dissolved in C$_3$H$_7$CN (green), CH$_2$Cl$_2$ (blue), DMF (black), or C$_6$H$_5$CN (red) solution

under argon at a scan rate of 250 mV s^{-1}. (b) Cyclic voltammograms recorded using

FeTTPCl (1 mM) and TBAPF$_6$ (0.1 M) dissolved in C$_3$H$_7$CN (green), CH$_2$Cl$_2$ (blue),

DMF (black), or C$_6$H$_5$CN (red) solution under argon at a scan rate of 250 mV s^{-1}. All

voltammograms were recorded using a 3 mm diameter glassy carbon WE at room

temperature and the ferrocenium/ferrocene redox couple as an internal reference.

Table 2.1 Midpoint potentials ($^nE_{1/2}$) of **Fe2FPCl2** as determined by cyclic voltammetry and reported as reduction half-reaction by convention. Peak-to-peak separations (ΔE_p) are reported in parentheses. All voltammograms were collected under argon and at room temperature using a 3 mm diameter glassy carbon WE immersed in solutions containing 1 mM porphyrin and 0.1 M TBAPF$_6$ in C$_3$H$_7$CN, CH$_2$Cl$_2$, DMF, or C$_6$H$_5$CN. In all of these experiments, the ferrocenium/ferrocene redox couple was used as an internal reference.

| | ^nE (V vs Fc$^+$/Fc) | | | | | |
	^{VI}E (ΔE_p, mV) [Fe2FP]$^{3-}$ /[Fe2FP]$^{4-}$	^{V}E (ΔE_p, mV) [Fe2FP]$^{2-}$ /[Fe2FP]$^{3-}$	^{IV}E (ΔE_p, mV) [Fe2FP]$^{1-}$ /[Fe2FP]$^{2-}$	^{III}E (ΔE_p, mV) [Fe2FP]^{0} /[Fe2FP]$^{1-}$	^{II}E (ΔE_p, mV) [Fe2FP]$^{1+}$ /[Fe2FP]^{0}	^{I}E (ΔE_p, mV) [Fe2FP]$^{2+}$/ [Fe2FP]$^{1+}$
C$_3$H$_7$CN	-	-2.16^a (89)	-1.48^a (69)	-1.21^a (69)	-0.84^a (69)	-0.67^a (55)
CH$_2$Cl$_2$	-	-	-1.55^a (102)	-1.18^a (102)	-0.69^b / -0.89^c	-
DMF	-2.40^a (81)	-2.11^a (75)	-1.46^a (74)	-1.21^a (75)	-0.71^b / -0.76^c	-0.56^b / -0.64^c
C$_6$H$_5$CN	-	-	-1.49^b / -1.58^c	-1.35^b / -1.48^c	-0.42^b / -0.87^c	-0.26^b / -0.72^c

[a] $E = E_{1/2}$; electrochemically reversible or quasi-reversible. [b] E = anodic peak potential; electrochemically irreversible. [c] E = cathodic peak potential; electrochemically irreversible.

46

Table 2.2 Midpoint potentials ($^{n}E_{1/2}$) of **FeTTPCl** as determined by cyclic voltammetry and reported as reduction half-reactions by convention. Peak-to-peak separations (ΔE_p) are reported in parentheses. All voltammograms were collected under argon and at room temperature using a 3 mm diameter glassy carbon WE immersed in solutions containing 1 mM porphyrin and 0.1 M TBAPF$_6$ in C$_3$H$_7$CN, CH$_2$Cl$_2$, DMF, or C$_6$H$_5$CN. In all of these experiments, the ferrocenium/ferrocene redox couple was used as an internal reference.

	^{n}E (V vs Fc$^+$/Fc)		
	^{III}E (ΔE_p, mV)	^{II}E (ΔE_p, mV)	^{I}E (ΔE_p, mV)
	[FeTTP]$^{1-}$/[FeTTP]$^{2-}$	[FeTTP]^{0}/[FeTTP]$^{1-}$	[FeTTP]$^{1+}$/[FeTTP]^{0}
C$_3$H$_7$CN	-2.21[a] (89)	-1.54[a] (89)	-0.78[a] (92)
CH$_2$Cl$_2$	-	-1.57[a] (140)	-0.71[b] / -0.86[c]
DMF	-2.18[a] (87)	-1.53[a] (80)	-0.56[b] / -0.73[c]
C$_6$H$_5$CN	-	-1.60[a] (110)	-0.40[b], -0.72[b] / -0.84[c]

[a] $E = E_{½}$; electrochemically reversible or quasi-reversible.

[b] E = anodic peak potential; electrochemically irreversible.

[c] E = cathodic peak potential; electrochemically irreversible.

2.2.5 UV-Vis-NIR-SEC and IR-SEC Measurements

Differentiating ligand-based versus metal-centered redox processes can be challenging and redox processes involving metalloporphyrins have been ascribed to both innocent and non-innocent (*i.e.*, guilty) ligand chemistry.[75–81] Thus, generalized predictions regarding their reactivities should be approached cautiously. Nonetheless, UV-Vis-near

infrared spectroelectrochemistry (UV-Vis-NIR-SEC) and infrared

spectroelectrochemistry (IR-SEC) enable comparisons of the changes in electronic and

vibrational structure following reduction of the fused Fe(III) porphyrin macrocycles

described in this report and their model monomeric analogs.

UV-Vis-NIR-SEC measurements recorded using **Fe₂FPCl₂** in DMF (0.05 mM) indicate

the two-electron reduction of **[Fe₂FP]**$^{2+}$, to form **[Fe₂FP]**^{0}, gives rise to a

bathochromically-shifted, Soret-like absorption band centered at 430 nm as well as two

other secondary Soret-like bands centered at 499 nm and 545 nm, and a

hypsochromically-shifted Q-like band centered at 809 nm (Figure 2.7a). Under the

conditions used in this experiment, spectrum associated with the one-electron reduction

of **[Fe₂FP]**$^{2+}$ to form **[Fe₂FP]**$^{1+}$ was not resolved. Polarizing the working electrode (WE)

to more negative potentials gives rise to further spectroscopic transitions that are assigned

to reduction of **[Fe₂FP]**^{0} to form **[Fe₂FP]**$^{1-}$ (Figure 2.7b), whereupon the Soret-like band

at 430 nm decreases in intensity, the secondary Soret-like bands at 499 nm and 545 nm

are replaced by a broad absorption feature, and the Q-like band centered at 809 nm is

replaced by a Q-like band centered at ~880 nm. Further reduction to form **[Fe₂FP]**$^{2-}$

results in the appearance of a bathochromically-shifted, Soret-like band at 439 nm, the

growth of a new secondary Soret-like band at 594 nm, and an increase in the intensity of

the Q-like band centered at ~880 nm (Figure 2.7b). The reduction of **[Fe₂FP]**$^{2-}$ to form

[Fe₂FP]$^{3-}$ shows a loss of the secondary Soret-like band at 594 nm, the rise of a new

secondary Soret-like band at 562 nm, and a decrease in the intensity of the Q-like band at

~880 nm (Figure 2.7c). Finally, the conversion of **[Fe₂FP]**$^{3-}$ to **[Fe₂FP]**$^{4-}$ is associated

with a loss of the secondary Soret-like absorption at 562 nm, and an increase in the
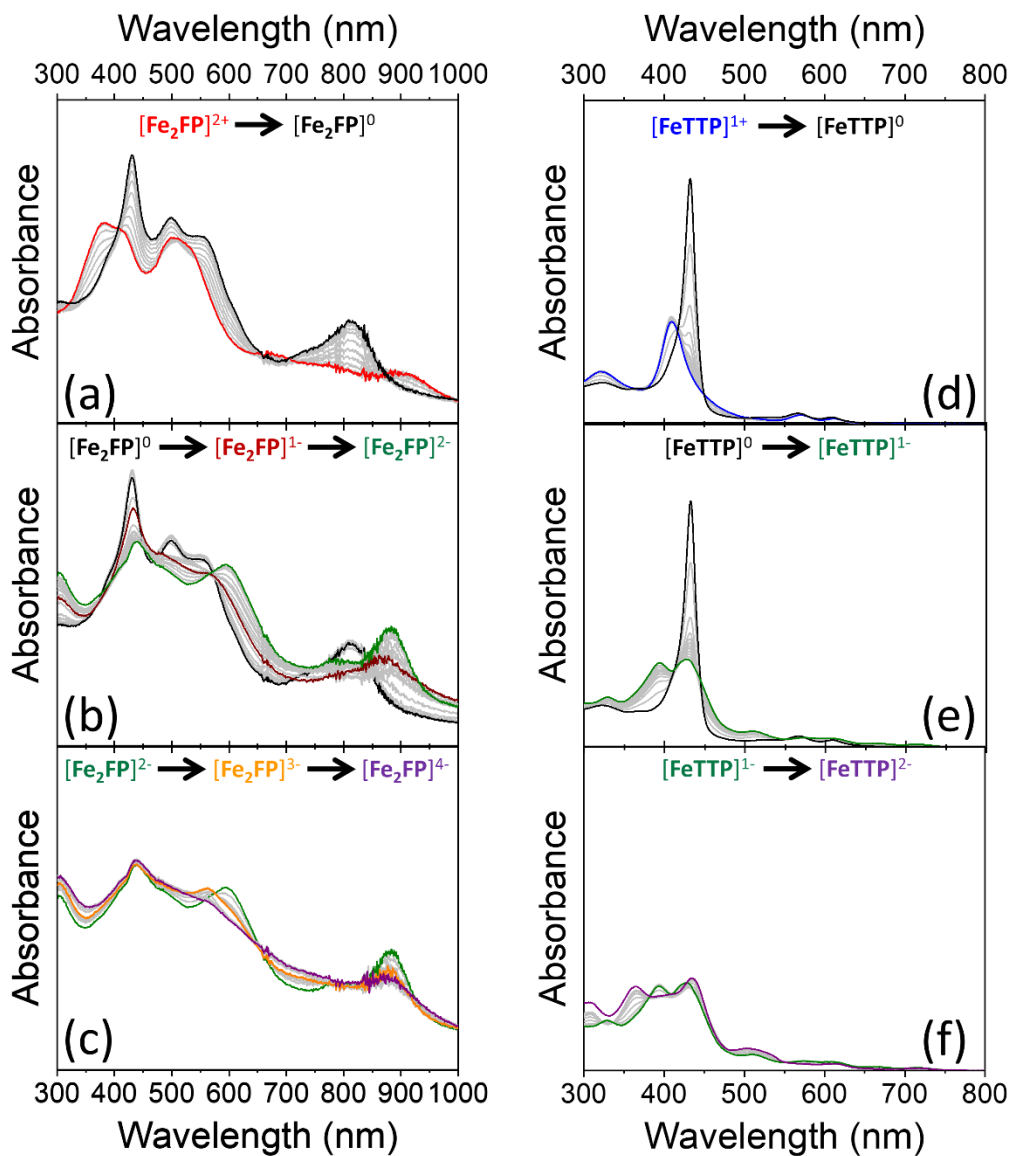
Figure 2.7 UV-Vis-NIR absorption spectra of (a-c) **Fe₂FPCl₂** (0.05 mM) recorded in a 0.1 M TBAPF$_6$ DMF solution polarized at potentials to generate **[Fe₂FP]**$^{2-}$ (red), **[Fe₂FP]**^{0} (black), **[Fe₂FP]**$^{1-}$ (maroon), **[Fe₂FP]**$^{2-}$ (green), **[Fe₂FP]**$^{3-}$ (orange), and **[Fe₂FP]**$^{4-}$ (purple) as well as spectra of (d-f) **FeTTPCl** (0.05 mM) recorded in a 0.1 M TBAPF$_6$ DMF solution polarized at potentials to generate **[FeTTP]**$^{1+}$ (blue), **[FeTTP]**^{0} (black), **[FeTTP]**$^{1-}$ (green), and **[FeTTP]**$^{2-}$ (purple).

intensity of the Soret-like band at 438 nm (Figure 2.7c). The presence of well-defined

isosbestic points at 369 nm, 447 nm, 474 nm, and 577 nm during the conversion of

[Fe₂FP]^0 to **[Fe₂FP]**$^{1-}$, 400 nm and 567 nm for the conversion of **[Fe₂FP]**$^{1-}$ to **[Fe₂FP]**$^{2-}$,

575 nm, 658 nm, and 774 nm for the conversion of **[Fe₂FP]**$^{2-}$ to **[Fe₂FP]**$^{3-}$, as well as at

524 nm and 641 nm for the conversion of **[Fe₂FP]**$^{3-}$ to **[Fe₂FP]**$^{4-}$, are consistent with

relatively stable conversion from one redox state to the next without the formation of

intermediates or decomposition products.

UV-Vis-NIR-SEC data collected using **FeTTPCl** in DMF (0.05 mM) show the one-

electron reduction of **[FeTTP]**$^{1+}$ to form **[FeTTP]**^{0} results in a loss of the Soret-band and

the rise of a bathochromically-shifted Soret-band centered at 433 nm (Figure 2.7d).

Further reduction from **[FeTTP]**^{0} to form **[FeTTP]**$^{1-}$ results in in a decreased intensity of

the Soret-band at 433 nm and the appearance of new bands at 428 nm and 394 nm

(Figure 2.7e). Finally, the conversion of **[FeTTP]**$^{1-}$ to **[FeTTP]**$^{2-}$ results in the loss of the

bands at 394 nm and 428 nm, and the rise of two new absorption bands at365 nm and 436

nm (Figure 2.7f). These experiments were performed over the same range of potentials

that were used to collect the UV-Vis-NIR-SEC data for **Fe₂FPCl₂** and show relatively

clean spectroscopic transitions associated with the **[FeTTP]**$^{2+}$/**[FeTTP]**$^{1+}$,

[FeTTP]$^{1+}$/**[FeTTP]**^{0}, and **[FeTTP]**^{0}/**[FeTTP]**$^{1-}$ redox couples. The presence of well-

defined isosbestic points at 418 nm and 450 nm during the conversion of **[FeTTP]**$^{1+}$ to

[FeTTP]^0, 421 nm and 445 nm during the conversion of **[FeTTP]**^{0} to **[FeTTP]**$^{1-}$, as well

as at 380 nm during the conversion of **[FeTTP]**$^{1-}$ to form **[FeTTP]**$^{2-}$, are consistent with

stable conversion from one redox state to the next without the formation of intermediates

or decomposition products. To better observe the spectroscopic changes in the Q-band

region, experiments were also recorded using higher concentrations of **FeTTPCl** (0.25 mM) (Figure 4.9).

IR-SEC measurements recorded using **Fe₂FPCl₂** or **FeTTPCl** in DMF (1.0 mM or 0.4 mM, respectively) show that upon reduction of these complexes there are distinct changes in the frequency range characteristic of in-plane iron porphyrin deformation vibrations. The two-electron reduction of **[Fe₂FP]**$^{2+}$ to form **[Fe₂FP]**^{0} gives rise to a relatively broad band centered at 1000 cm^{-1} (Figure 2.8a). As in the case of the UV-Vis-NIR-SEC experiments, a spectrum for the one-electron reduction from **[Fe₂FP]**$^{2+}$ to **[Fe₂FP]**$^{1+}$ was not resolved under the conditions used in these IR-SEC experiments. Further reduction, to form **[Fe₂FP]**$^{1-}$, gives rise to new bands centered at 1007 cm^{-1} and 993 cm^{-1}, and the reduction of **[Fe₂FP]**$^{1-}$ to form **[Fe₂FP]**$^{2-}$ results in a loss of the band at 993 cm^{-1} and an increase in the band at 1007 cm^{-1} (Figure 2.8b). Finally, the reduction of **[Fe₂FP]**$^{2-}$ to form **[Fe₂FP]**$^{3-}$ shows a decrease in the intensity of the band centered at 1007 cm^{-1}, along with an increase of a broad band centered at 993 cm^{-1} (Figure 2.8c). Further reduction, to obtain spectra associated with formation of **[Fe₂FP]**$^{4-}$, was not detected using the IR-SEC cell configuration for these experiments.

In the case of IR-SEC measurements recorded using **FeTTPCl**, one-electron reduction to form **[FeTTP]**^{0} results in a shift of ν_{Fe-N} from 999 cm^{-1} to 991 cm^{-1} ($\Delta\nu_1$=8 cm^{-1}) (Figure 2.8d), while further reduction from **[FeTTP]**^{0} to **[FeTTP]**$^{1-}$ yields further displacement from 991 cm^{-1} to 985 cm^{-1} ($\Delta\nu_2$=6 cm^{-1}) (Figure 2.8e). Further reduction, to obtain spectra associated with formation of **[FeTTP]**$^{2-}$, was not detected using the cell configuration for these experiments.
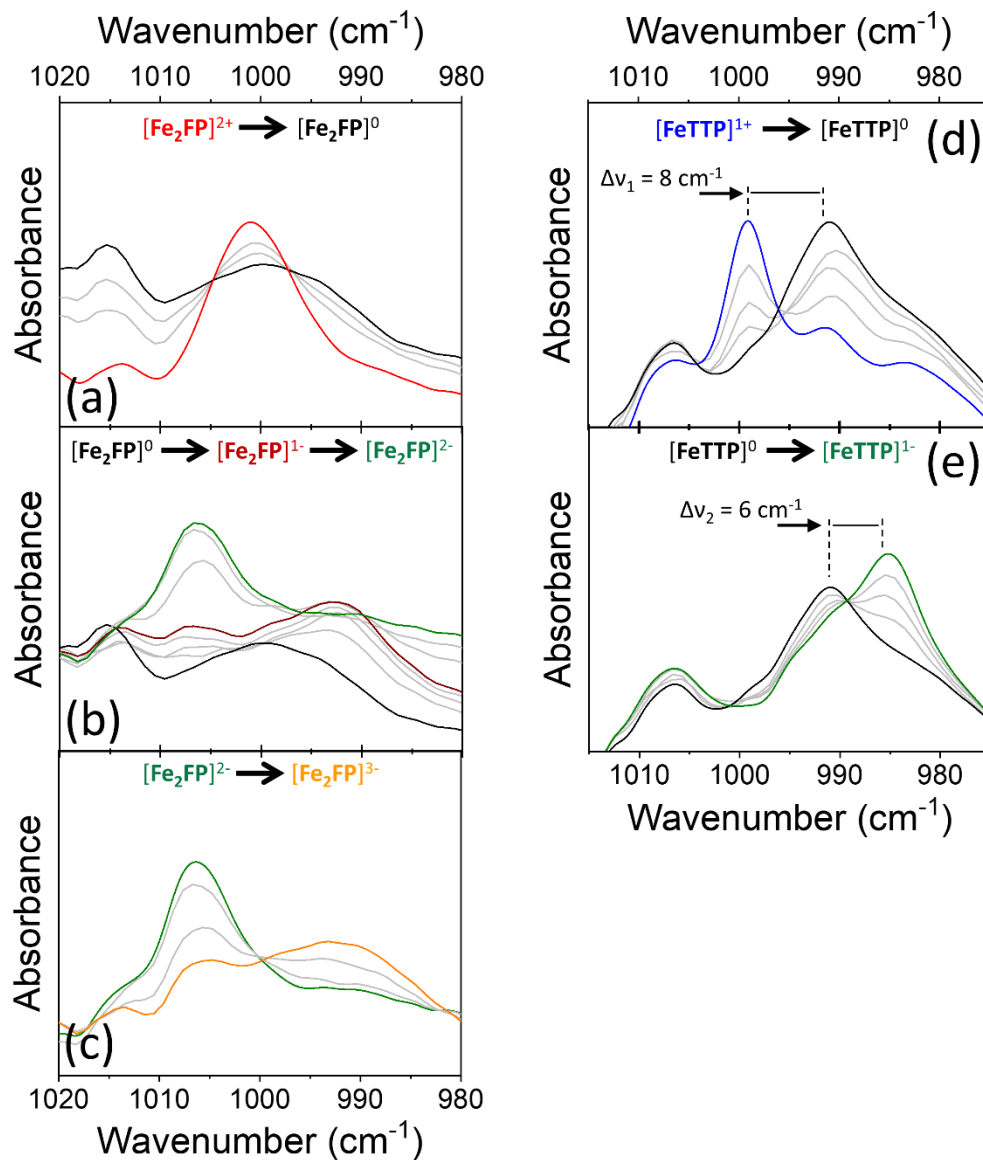
Figure 2.8 FTIR absorption spectra of (a-c) **Fe₂FPCl₂** (1.0 mM) recorded in a 0.1 M

TBAPF₆ DMF solution polarized at potentials to generate **[Fe₂FP]**$^{2+}$ (red), **[Fe₂FP]**^{0}

(black), **[Fe₂FP]**$^{1-}$ (maroon), **[Fe₂FP]**$^{2-}$ (green), and **[Fe₂FP]**$^{3-}$ (orange), as well as spectra

of (d-e) **FeTTPCl** (0.4 mM) recorded in a 0.1 M TBAPF₆ DMF solution polarized at

potentials to generate **[FeTTP]**$^{1+}$ (blue), **[FeTTP]**^{0} (black), and **[FeTTP]**$^{1-}$ (green).

52

2.3 Conclusions

The synthesis and characterization of a novel binuclear Fe(III) fused porphyrin is reported. The fused-iron-porphyrin assembly described in this chapter features: 1) bimetallic-iron sites, 2) a more rigid, π-extended ligand environment capable of delocalizing electrons across the multimetallic scaffold, and 3) the ability to store up to six electrons. These properties provide an alternative but complementary approach to the use of extended coordination spheres and the use of electron-withdrawing or -donating groups to modulate the redox potential of the metal center within the electrocatalytic complex, and ultimately could prove promising in the context of catalyzing multielectron, multisubstrate redox reactions.

2.4 References

(1)   Zhang, W.; Lai, W.; Cao, R. Energy-Related Small Molecule Activation Reactions: Oxygen Reduction and Hydrogen and Oxygen Evolution Reactions Catalyzed by Porphyrin- and Corrole-Based Systems. *Chem. Rev.* **2017**, *117* (4), 3717–3797.

(2)   Beyene, B. B.; Hung, C.-H. Recent Progress on Metalloporphyrin-Based Hydrogen Evolution Catalysis. *Coord. Chem. Rev.* **2020**, *410*, 213234.

(3)   Gotico, P.; Halime, Z.; Aukauloo, A. Recent Advances in Metalloporphyrin-Based Catalyst Design towards Carbon Dioxide Reduction: From Bio-Inspired Second Coordination Sphere Modifications to Hierarchical Architectures. *Dalton Trans.* **2020**, *49* (8), 2381–2396.

(4)   Costentin, C.; Limoges, B.; Robert, M.; Tard, C. A Pioneering Career in Electrochemistry: Jean-Michel Saveánt. *ACS Catal.* **2021**, *11* (6), 3224–3238.

(5)   Hammouche, M.; Lexa, D.; Momenteau, M.; Savéant, J.-M. Chemical Catalysis of Electrochemical Reactions. Homogeneous Catalysis of the Electrochemical Reduction of Carbon Dioxide by Iron("0") Porphyrins. Role of the Addition of Magnesium Cations. *J. Am. Chem. Soc.* **1991**, *113* (22), 8455–8466.

(6)   Bhugun, I.; Lexa, D.; Savéant, J.-M. Ultraefficient Selective Homogenous Catalysis of the Electrochemical Reduction of Carbon Dioxide by an Iron(0)

Porphyrin Associated with a Weak Bronsted Acid Cocatalyst. *J. Am. Chem. Soc.* **1994**, *116* (11), 5015–5016.

(7)   Bhugun, I.; Lexa, D.; Savéant, J.-M. Catalysis of the Electrochemical Reduction of Carbon Dioxide by Iron(0) Porphyrins: Synergystic Effect of Weak Brönsted Acids. *J. Am. Chem. Soc.* **1996**, *118* (7), 1769–1776.

(8)   Bhugun, I.; Lexa, D.; Savéant, J.-M. Catalysis of the Electrochemical Reduction of Carbon Dioxide by Iron(0) Porphyrins. Synergistic Effect of Lewis Acid Cations. *J. Phys. Chem.* **1996**, *100* (51), 19981–19985.

(9)   Bhugun, I.; Lexa, D.; Savéant, J.-M. Homogeneous Catalysis of Electrochemical Hydrogen Evolution by Iron(0) Porphyrins. *J. Am. Chem. Soc.* **1996**, *118* (16), 3982–3983.

(10)   Costentin, C.; Drouet, S.; Robert, M.; Savéant, J.-M. Turnover Numbers, Turnover Frequencies, and Overpotential in Molecular Catalysis of Electrochemical Reactions. Cyclic Voltammetry and Preparative-Scale Electrolysis. *J. Am. Chem. Soc.* **2012**, *134* (27), 11235–11242.

(11)   Costentin, C.; Drouet, S.; Passard, G.; Robert, M.; Savéant, J.-M. Proton-Coupled Electron Transfer Cleavage of Heavy-Atom Bonds in Electrocatalytic Processes. Cleavage of a C-O Bond in the Catalyzed Electrochemical Reduction of CO_2. *J. Am. Chem. Soc.* **2013**, *135* (24), 9023–9031.

(12)   Costentin, C.; Dridi, H.; Savéant, J.-M. Molecular Catalysis of H_2 Evolution: Diagnosing Heterolytic versus Homolytic Pathways. *J. Am. Chem. Soc.* **2014**, *136* (39), 13727–13734.

(13)   Costentin, C.; Drouet, S.; Robert, M.; Savéant, J.-M. A Local Proton Source Enhances CO_2 Electroreduction to CO by a Molecular Fe Catalyst. *Science* **2012**, *338* (6103), 90–94.

(14)   Costentin, C.; Passard, G.; Robert, M.; Savéant, J.-M. Pendant Acid-Base Groups in Molecular Catalysts: H-Bond Promoters or Proton Relays? Mechanisms of the Conversion of CO_2 to CO by Electrogenerated Iron(0)Porphyrins Bearing Prepositioned Phenol Functionalities. *J. Am. Chem. Soc.* **2014**, *136* (33), 11821–11829.

(15)   Costentin, C.; Robert, M.; Savéant, J.-M.; Tatin, A. Efficient and Selective Molecular Catalyst for the CO_2-to-CO Electrochemical Conversion in Water. *Proc. Natl. Acad. Sci. U.S.A.* **2015**, *112* (22), 6882–6886.

(16)   Azcarate, I.; Costentin, C.; Robert, M.; Savéant, J.-M. Through-Space Charge Interaction Substituent Effects in Molecular Catalysis Leading to the Design of

the Most Efficient Catalyst of CO_2-to-CO Electrochemical Conversion. *J. Am. Chem. Soc.* **2016**, *138* (51), 16639–16644.

(17)   Costentin, C.; Savéant, J.-M. Towards an Intelligent Design of Molecular Electrocatalysis. *Nat. Rev. Chem.* **2017**, *1*, 0087.

(18)   Costentin, C.; Passard, G.; Robert, M.; Savéant, J.-M. Ultraefficient Homogeneous Catalyst for the CO_2-to-CO Electrochemical Conversion. *Proc. Natl. Acad. Sci. U.S.A.* **2014**, *111* (42), 14990–14994.

(19)   Costentin, C.; Savéant, J.-M. Multielectron, Multistep Molecular Catalysis of Electrochemical Reactions: Benchmarking of Homogeneous Catalysts. *ChemElectroChem* **2014**, *1* (7), 1226–1236.

(20)   Costentin, C.; Savéant, J.-M. Heterogeneous Molecular Catalysis of Electrochemical Reactions: Volcano Plots and Catalytic Tafel Plots. *ACS Appl. Mater. Interfaces* **2017**, *9* (23), 19894–19899.

(21)   Artero, V.; Savéant, J.-M. Toward the Rational Benchmarking of Homogeneous H_2-Evolving Catalysts. *Energy Environ. Sci.* **2014**, *7* (11), 3808–3814.

(22)   Sugiura, K.; Matsumoto, T.; Ohkouchi, S.; Naitoh, Y.; Kawai, T.; Takai, Y.; Ushiroda, K.; Sakata, Y. Synthesis of the Porphyrin-Fused Porphyrin, [2]Porphyracene. *Chem. Commun.* **1999**, No. 19, 1957–1958.

(23)   Kim, D.; Osuka, A. Photophysical Properties of Directly Linked Linear Porphyrin Arrays. *J. Phys. Chem. A* **2003**, *107* (42), 8791–8816.

(24)   Tanaka, T.; Osuka, A. Conjugated Porphyrin Arrays: Synthesis, Properties and Applications for Functional Materials. *Chem. Soc. Rev.* **2015**, *44* (4), 943–969.

(25)   Khusnutdinova, D.; Wadsworth, B. L.; Flores, M.; Beiler, A. M.; Reyes Cruz, E. A.; Zenkov, Y.; Moore, G. F. Electrocatalytic Properties of Binuclear Cu(II) Fused Porphyrins for Hydrogen Evolution. *ACS Catal.* **2018**, *8* (10), 9888–9898.

(26)   Huerta-Flores, A. M.; Bengasi, G.; Baba, K.; Boscher, N. D. Fused Porphyrin Thin Films as Heterogeneous Visible-Light Active Photocatalysts with Well-Defined Active Metal Sites for Hydrogen Generation. *ACS Appl. Energy Mater.* **2020**, *3* (10), 9848–9855.

(27)   Liu, H.; Yu, C.; Gao, N.; Zhao, J. The Diversity of Electron-Transport Behaviors of Molecular Junctions: Correlation with the Electron-Transport Pathway. *ChemPhysChem* **2010**, *11* (9), 1895–1902.

(28)   Lysenko, A. B.; Thamyongkit, P.; Schmidt, I.; Diers, J. R.; Bocian, D. F.; Lindsey, J. S. Diverse Porphyrin Dimers as Candidates for High-Density Charge-Storage Molecules. *J. Porphyr. Phthalocyanines* **2006**, *10* (1), 22–32.

(29)   Tsuda, A.; Nakano, A.; Furuta, H.; Yamochi, H.; Osuka, A. Doubly *Meso*-β-Linked Diporphyrins from Oxidation of 5,10,15-Triaryl-Substituted Ni[II]-and Pd[II]-Porphyrins. *Angew. Chem. Int. Ed.* **2000**, *39* (3), 558–561.

(30)   Ouyang, Q.; Zhu, Y.-Z.; Zhang, C.-H.; Yan, K.-Q.; Li, Y.-C.; Zheng, J.-Y. An Efficient PIFA-Mediated Synthesis of Fused Diporphyrin and Triply-Singly Interlacedly Linked Porphyrin Array. *Org. Lett.* **2009**, *11* (22), 5266–5269.

(31)   Tanaka, T.; Lee, B. S.; Aratani, N.; Yoon, M.-C.; Kim, D.; Osuka, A. Synthesis and Properties of Hybrid Porphyrin Tapes. *Chem. Eur. J.* **2011**, *17* (51), 14400–14412.

(32)   Dimé, A. K. D.; Devillers, C. H.; Cattey, H.; Lucas, D. Versatile Redox Reactivity of Triaryl-*Meso*-Substituted Ni(II) Porphyrin. *Dalton Trans.* **2014**, *43* (39), 14554–14564.

(33)   Feng, C.-M.; Zhu, Y.-Z.; Zang, Y.; Tong, Y.-Z.; Zheng, J.-Y. Switchable Regioselectivity in the PIFA-BF$_3$·Et$_2$O Mediated Oxidative Coupling of *Meso*-Brominated Ni(II) Porphyrin. *Org. Biomol. Chem.* **2014**, *12* (36), 6990–6993.

(34)   Feng, C.-M.; Zhu, Y.-Z.; Zhang, S.-C.; Zang, Y.; Zheng, J.-Y. Synthesis of Directly Fused Porphyrin Dimers through Fe(OTf)$_3$-Mediated Oxidative Coupling. *Org. Biomol. Chem.* **2015**, *13* (9), 2566–2569.

(35)   Osuka, A. Compound Having 2 To 4 Porphyrins Doubly Bonded (Condensed) By Each Meso-Beta Carbon-Carbon. JPA 2001-089490, 2001.

(36)   Tsuda, A.; Furuta, H.; Osuka, A. Syntheses, Structural Characterizations, and Optical and Electrochemical Properties of Directly Fused Diporphyrins. *J. Am. Chem. Soc.* **2001**, *123* (42), 10304–10321.

(37)   Tsuda, A.; Nakamura, Y.; Osuka, A. Synthesis of *Meso-β* Doubly Linked Porphyrin Tapes. *Chem. Commun.* **2003**, No. 9, 1096–1097.

(38)   Kamo, M.; Tsuda, A.; Nakamura, Y.; Aratani, N.; Furukawa, K.; Kato, T.; Osuka, A. Metal-Dependent Regioselective Oxidative Coupling of 5,10,15-Triarylporphyrins with DDQ-Sc(OTf)$_3$ and Formation of an Oxo-Quinoidal Porphyrin. *Org. Lett.* **2003**, *5* (12), 2079–2082.

(39)   Muranaka, A.; Yokoyama, M.; Matsumoto, Y.; Uchiyama, M.; Tsuda, A.; Osuka, A.; Kobayashi, N. Magnetic Circular Dichroism Study of Directly Fused Porphyrins. *ChemPhysChem* **2005**, *6* (1), 171–179.

(40)   Kim, D. Y.; Ahn, T. K.; Kwon, J. H.; Kim, D.; Ikeue, T.; Aratani, N.; Osuka, A.; Shigeiwa, M.; Maeda, S. Large Two-Photon Absorption (TPA) Cross-Section of Directly Linked Fused Diporphyrins. *J. Phys. Chem. A* **2005**, *109* (13), 2996–2999.

(41)   Sahoo, A. K.; Nakamura, Y.; Aratani, N.; Kim, K. S.; Noh, S. B.; Shinokubo, H.; Kim, D.; Osuka, A. Synthesis of Brominated Directly Fused Diporphyrins through Gold(III)-Mediated Oxidation. *Org. Lett.* **2006**, *8* (18), 4141–4144.

(42)   Yoon, M.-C.; Noh, S. B.; Tsuda, A.; Nakamura, Y.; Osuka, A.; Kim, D. Photophysics of *Meso-β* Doubly Linked Ni(II) Porphyrin Arrays: Large Two-Photon Absorption Cross-Section and Fast Energy Relaxation Dynamics. *J. Am. Chem. Soc.* **2007**, *129* (33), 10080–10081.

(43)   Brennan, B. J.; Kenney, M. J.; Liddell, P. A.; Cherry, B. R.; Li, J.; Moore, A. L.; Moore, T. A.; Gust, D. Oxidative Coupling of Porphyrins Using Copper(II) Salts. *Chem. Commun.* **2011**, *47* (36), 10034–10036.

(44)   Tsuda, A.; Furuta, H.; Osuka, A. Completely Fused Diporphyrins and Triporphyrin. *Angew. Chem.* **2000**, *112* (14), 2649–2652.

(45)   Tsuda, A.; Osuka, A. Fully Conjugated Porphyrin Tapes with Electronic Absorption Bands That Reach into Infrared. *Science* **2001**, *293* (5527), 79–82.

(46)   Ikeue, T.; Furukawa, K.; Hata, H.; Aratani, N.; Shinokubo, H.; Kato, T.; Osuka, A. The Importance of a β-β Bond for Long-Range Antiferromagnetic Coupling in Directly Linked Copper(II) and Silver(II) Diporphyrins. *Angew. Chem. Int. Ed.* **2005**, *44* (42), 6899–6901.

(47)   Fendt, L.-A.; Fang, H.; Plonska-Brzezinska, M. E.; Zhang, S.; Cheng, F.; Braun, C.; Echegoyen, L.; Diederich, F. Meso,Meso-Linked and Triply Fused Diporphyrins with Mixed-Metal Ions: Synthesis and Electrochemical Investigations. *Eur. J. Org. Chem.* **2007**, *2007* (28), 4659–4673.

(48)   Cho, H. S.; Jeong, D. H.; Cho, S.; Kim, D.; Matsuzaki, Y.; Tanaka, K.; Tsuda, A.; Osuka, A. Photophysical Properties of Porphyrin Tapes. *J. Am. Chem. Soc.* **2002**, *124* (49), 14642–14654.

(49)   Tsuda, A.; Osuka, A. Discrete Conjugated Porphyrin Tapes with an Exceptionally Small Bandgap. *Adv. Mater.* **2002**, *14* (1), 75–79.

(50) Nakamura, Y.; Aratani, N.; Tsuda, A.; Osuka, A.; Furukawa, K.; Kato, T. Oxidative Direct Coupling of Metalloporphyrins. *J. Porphyr. Phthalocyanines* **2003**, *7* (4), 264–269.

(51) Nalin De Silva, K. M. Meso-β Doubly Linked and Meso-Meso, β-β, β-β Triply Linked Oligoporphyrin Molecular Tapes as Potential Non Linear Optical (NLO) Materials: Quantum Chemical Calculations. *J. Mol. Struct.: THEOCHEM.* **2005**, *726* (1–3), 39–45.

(52) Cheng, F.; Zhang, S.; Adronov, A.; Echegoyen, L.; Diederich, F. Triply Fused ZnII-Porphyrin Oligomers: Synthesis, Properties, and Supramolecular Interactions with Single-Walled Carbon Nanotubes (SWNTs). *Chem. Eur. J.* **2006**, *12* (23), 6062–6070.

(53) Zhang, X.-B.; Feng, J.-K.; Ren, A.-M.; Sun, C.-C. A Comparative Study of One- and Two-Photon Absorption Properties of *Meso-Meso* Singly, *Meso-*β Doubly and *Meso-Meso* β-β β-β Triply Linked Zn^{II}-Porphyrin Oligomers. *J. Mol. Struct.: THEOCHEM.* **2007**, *804* (1–3), 21–29.

(54) Ikeda, T.; Aratani, N.; Easwaramoorthi, S.; Kim, D.; Osuka, A. Meso-*β* Doubly Linked Zn(II) Porphyrin Trimers: Distinct *Anti-*versus-*Syn* Effects on Their Photophysical Properties. *Org. Lett.* **2009**, *11* (14), 3080–3083.

(55) Heo, J. H.; Ikeda, T.; Lim, J. M.; Aratani, N.; Osuka, A.; Kim, D. Molecular-Shape-Dependent Photophysical Properties of *Meso-β* Doubly Linked Zn(II) Porphyrin Arrays and Their Indene-Fused Analogues. *J. Phys. Chem. B* **2010**, *114* (45), 14528–14536.

(56) Mai, C.-L.; Huang, W.-K.; Lu, H.-P.; Lee, C.-W.; Chiu, C.-L.; Liang, Y.-R.; Diau, E. W.-G.; Yeh, C.-Y. Synthesis and Characterization of Diporphyrin Sensitizers for Dye-Sensitized Solar Cells. *Chem. Commun.* **2010**, *46* (5), 809–811.

(57) Diev, V. V.; Hanson, K.; Zimmerman, J. D.; Forrest, S. R.; Thompson, M. E. Fused Pyrene-Diporphyrins: Shifting Near-Infrared Absorption to 1.5 μm and Beyond. *Angew. Chem. Int. Ed.* **2010**, *49* (32), 5523–5526.

(58) Tokita, Y.; Suzuki, Y.; Morooka, M.; Noda, K. Dye Sensitized Photoelectric Conversion Device. JPA 2005-276410, 2005.

(59) Lee, S.; Yamashita, K.; Sakata, N.; Hirao, Y.; Ogawa, K.; Ogawa, T. Stable Singlet Biradicals of Rare-Earth-Fused Diporphyrin-Triple-Decker Complexes with Low Energy Gaps and Multi-Redox States. *Chem. Eur. J.* **2019**, *25* (13), 3240–3243.

(60)   Khusnutdinova, D.; Beiler, A. M.; Wadsworth, B. L.; Jacob, S. I.; Moore, G. F. Metalloporphyrin-Modified Semiconductors for Solar Fuel Production. *Chem. Sci.* **2017**, *8* (1), 253–259.

(61)   Boucher, L. J.; Katz, J. J. The Infrared Spectra of Metalloporphyrins (4000-160 Cm^{-1}). *J. Am. Chem. Soc.* **1967**, *89* (6), 1340–1345.

(62)   Alben, J. O.; Choi, S. S.; Adler, A. D.; Caughey, W. S. Infrared Spectroscopy of Porphyrins. *Ann. N. Y. Acad. Sci.* **1973**, *206* (1), 278–295.

(63)   Bar-Ilan, A.; Manassen, J. Heterogeneous and Homogeneous Catalysis by Substituted Cobalt Tetraphenylporphyrins, and Correlations with IR Spectra. *J. Catal.* **1974**, *33* (1), 68–73.

(64)   Kincaid, J.; Nakamoto, K. Vibrational Spectra of Transition Metal Complexes of Tetraphenylporphine. *J. Inorg. Nucl. Chem.* **1975**, *37* (1), 85–89.

(65)   Beiler, A. M.; Khusnutdinova, D.; Wadsworth, B. L.; Moore, G. F. Cobalt Porphyrin-Polypyridyl Surface Coatings for Photoelectrosynthetic Hydrogen Production. *Inorg. Chem.* **2017**, *56* (20), 12178–12185.

(66)   Khusnutdinova, D.; Beiler, A. M.; Wadsworth, B. L.; Nanyangwe, S. K.; Moore, G. F. Vibrational Structure Analysis of Cobalt Fluoro-Porphyrin Surface Coatings on Gallium Phosphide. *J. Porphyr. Phthalocyanines* **2018**, *22* (6), 461–468.

(67)   Khusnutdinova, D.; Flores, M.; Beiler, A. M.; Moore, G. F. Synthesis and Characterization of a Cobalt(II) Tetrakis(3-Fluorophenyl) Porphyrin with a Built-in 4-Vinylphenyl Surface Attachment Moiety. *Photosynthetica* **2018**, *56* (1), 67–74.

(68)   Wadsworth, B. L.; Khusnutdinova, D.; Urbine, J. M.; Reyes, A. S.; Moore, G. F. Expanding the Redox Range of Surface-Immobilized Metallocomplexes Using Molecular Interfaces. *ACS Appl. Mater. Interfaces* **2020**, *12* (3), 3903–3911.

(69)   Römelt, C.; Song, J.; Tarrago, M.; Rees, J. A.; van Gastel, M.; Weyhermüller, T.; Debeer, S.; Bill, E.; Neese, F.; Ye, S. Electronic Structure of a Formal Iron(0) Porphyrin Complex Relevant to CO_2 Reduction. *Inorg. Chem.* **2017**, *56* (8), 4745–4750.

(70)   Westre, T. E.; Kennepohl, P.; DeWitt, J. G.; Hedman, B.; Hodgson, K. O.; Solomon, E. I. A Multiplet Analysis of Fe K-Edge 1s → 3d Pre-Edge Features of Iron Complexes. *J. Am. Chem. Soc.* **1997**, *119* (27), 6297–6314.

(71)   Lexa, D.; Momenteau, M.; Rentien, P.; Rytz, G.; Savéant, J.-M.; Xu, F. Molecular Environment Effects in Redox Chemistry. Electrochemistry of Ether-Linked Basket-Handle and Amine-Linked Basket-Handle and Picket-Fence Iron Porphyrins. *J. Am. Chem. Soc.* **1984**, *106* (17), 4755–1765.

(72)   Mashiko, T.; Reed, C. A.; Scheidt, W. R. Nature of Iron (I) and Iron (0) Tetraphenylporphyrin Complexes. Synthesis and Molecular Structure of (Dibenzo-18-Crown-6)Bis(Tetrahydrofuran)Sodium (*Meso*-Tetraphenylporphinato)Ferrate and Bis[Tris(Tetrahydrofuran)Sodium] (*Meso*-Tetrapheynlporphinato)Ferrate. *Inorg. Chem.* **1984**, *23* (20), 3192–3196.

(73)   Trasatti, S. The Absolute Electrode Potential: An Explanatory Note. *J. Electroanal. Chem.* **1986**, *209*, 417–428.

(74)   Bard, A. J.; Faulkner, L. R. *Electrochemical Methods: Fundamentals and Applications*, 2nd ed.; Wiley & Sons, 2001.

(75)   Lexa, D.; Mispelter, J.; Savéant, J.-M. Electroreductive Alkylation of Iron in Porphyrin Complexes. Electrochemical and Spectral Characteristics of σ-Alkyliron Porphyrins. *J. Am. Chem. Soc.* **1981**, *103* (23), 6806–6812.

(76)   Lexa, D.; Savéant, J.-M.; Wang, D. L. Electroreductive Alkylation of Iron Porphyrins. Iron(III), Iron(II), and Iron(I) Alkyl Complexes from the Reaction of Doubly Reduced Iron(II) Porphyrins with Alkyl Halides. *Organometallics* **1986**, *5* (7), 1428–1434.

(77)   Kadish, K. M.; van Caemelbecke, E. Electrochemistry of Porphyrins and Related Macrocycles. *J. Solid State Chem.* **2003**, *7* (5), 254–258.

(78)   Sun, H.; Smirnov, V. v.; DiMagno, S. G. Slow Electron Transfer Rates for Fluorinated Cobalt Porphyrins: Electronic and Conformational Factors Modulating Metalloporphyrin ET. *Inorg. Chem.* **2003**, *42* (19), 6032–6040.

(79)   Lyaskovskyy, V.; de Bruin, B. Redox Non-Innocent Ligands: Versatile New Tools to Control Catalytic Reactions. *ACS Catal.* **2012**, *2* (2), 270–279.

(80)   Luca, O. R.; Crabtree, R. H. Redox-Active Ligands in Catalysis. *Chem. Soc. Rev.* **2013**, *42* (4), 1440–1459.

(81)   Wu, Y.; Jiang, J.; Weng, Z.; Wang, M.; Broere, D. L. J.; Zhong, Y.; Brudvig, G. W.; Feng, Z.; Wang, H. Electroreduction of CO_2 Catalyzed by a Heterogenized Zn-Porphyrin Complex with a Redox-Innocent Metal Center. *ACS Cent. Sci.* **2017**, *3* (8), 847–852.

CHAPTER 3

PROTON-COUPLED ELECTRON TRANSFERS IN GROTHUSS-TYPE PROTON

WIRES

Portions of this chapter are excerpted and reprinted with permission from:

Arsenault, E. A.; Guerra, W. D.; Shee, J.; Reyes Cruz, E. A.; Yoneda, Y.; Wadsworth, B. L.; Odella, E.; Urrutia, M. N.; Kodis, G.; Moore, G. F.; Head-Gordon, M.; Moore, A. L.; Moore, T. A.; Fleming, G. R. Concerted Electron-Nuclear Motion in Proton-Coupled Electron Transfer-Driven Grotthuss-Type Proton Translocation. *J. Phys. Chem. Lett.*, **2022**, *13* (20): 4479–4485.

and

Odella, E.; Secor, M.; Reyes Cruz, E. A.; Guerra, W. D.; Urrutia, M. N.; Liddell, P. A.; Moore, T. A.; Moore, G. F.; Hammes-Schiffer, S.; Moore, A. L. Managing the Redox Potential of PCET in Grotthuss-Type Proton Wires. *J. Am. Chem. Soc.*, **2022**, *144* (34): 15672–15679.

Copyright 2022 American Chemical Society.

Contributions to this work included performing spectroelectrochemical experiments.

3.1 Introduction

Reversibly coupling the electrochemical potential of redox reactions to the generation of PMF is the central principle of bioenergetics in all living organisms.[1] Among a variety of mechanisms for generating PMF, two fundamental processes may be used in series. First, redox reactions involving protons may use PCET processes, which, in addition to providing kinetically efficient, low activation energy reaction pathways for protons and electrons, provides a thermodynamically efficient mechanism for coupling electrochemical potential to proton activity.[2–4] Second, a further elaboration of the PCET process by coupling it to Grotthuss-type proton translocations can provide an efficient mechanism for the transfer of protons over nanoscale distances as part of the process to generate PMF across energy-coupling biological membranes. Examples of PCET can be found in a wide range of biochemical reactions and Grotthuss-type processes have been suggested as mechanisms for proton transfer in many biological systems.[2–14]

A detailed understanding of how nature accomplishes the efficient conversion of redox potential to PMF via PCET and a Grotthuss-type process is necessary for it to be adapted to reengineered photosynthesis for improved yields.[15–17] Further, proton control is technologically important for improvements in a wide variety of catalysts.[18,19] Grotthuss-type processes have also been identified as key to extremely high charge/discharge rates in proton batteries.[20] As the full range of proton-based energy-linked processes in biology becomes better understood, and biomimicry becomes more influential in technology, the value of exchanging chemical potential between redox potential and PMF is likely to also find its way into technological applications—enabling cleaner and more efficient processes.

3.1.1 Monitoring PCET Via 2DEV Spectroscopy

Synchronizing the ensemble by ultrafast optical triggering and simultaneously observing the vibrational markers for electrons and proton transfer has the potential to provide new insight into the coupling of PCET and Grotthuss-type processes. Recently, a photodriven PCET was investigated in a biomimetic model system with the emerging two-dimensional electronic-vibrational (2DEV) spectroscopic technique[21,22] and electronic structure calculations in which electron and proton transfer were found to occur on a 120 fs time scale accompanied by substantial inner sphere reorganization.[23] In that system, a nonequilibrium PCET pathway was observed and found to correspond to the evolution from the photoexcited, partly charge transferred state to the fully charge separated state accompanied via nuclear rearrangement and solvation. Because the nonequilibrium pathway proceeded without a barrier, it was possible to dynamically track the evolution of the reaction (with the presence of a barrier, only the initial and final states would be significantly populated).

3.2 Results and Discussion: Photoinduced Electron-coupled Proton Transfer in a BIP-Porphyrin Dyad

A more complicated system was investigated, in which a similar photodriven PCET process is coupled to a Grotthuss-type proton wire so that a second proton translocation occurs and could be characterized dynamically. The construct is porphyrin-BIP-pyridine (**PF$_{15}$-BIP-Pyr**, Figure 3.1). Upon photoexcitation of the porphyrin moiety, ET from the phenol to the porphyrin is coupled to both proton transfer from the phenolic proton to benzimidazole and proton transfer from benzimidazole to pyridine (Figure 3.1) leading to the formation of a one-electron, two-proton transfer (E2PT) product. The application of

63
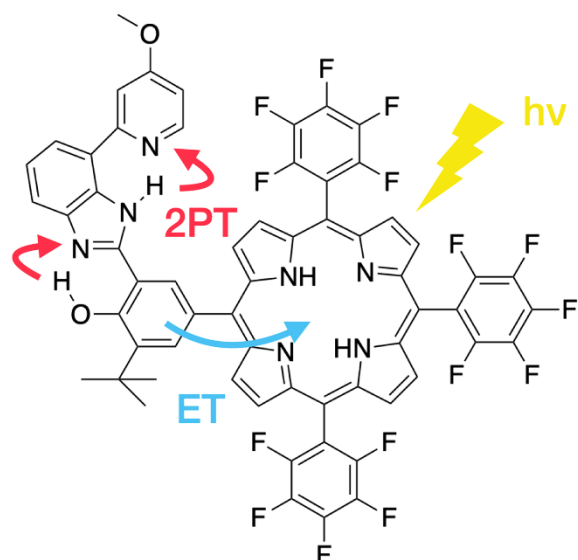
Figure 3.1 Molecular structure of the photoinduced proton wire (**PF$_{15}$-BIP-Pyr**). The red arrows indicate the double proton transfer (2PT) and the blue arrow indicates the electron transfer (ET) following photoexcitation (hv).

2DEV spectroscopy is leveraged in order to elucidate the coupled PCET and Grotthuss-type dynamics leading to the formation of the E2PT product. The results focus exclusively on the nonequilibrium pathway and find that the proton translocations are facilitated by a low frequency vibration of the BIP-Pyr moiety as supported by a recent theoretical investigation.[24] In addition, the presence of the low frequency modulation allows for a comparison of the phase associated with the spectroscopic signatures tracking electron and proton transfer and provides evidence that E2PT product formation is a concerted process. 2DEV spectroscopy also allows for the correlation between the electronic and nuclear degrees of freedom to be followed directly and is therefore highly sensitive to electronic-vibrational (vibronic) mixing, which is found to play a significant role in the dynamics of this proton wire.

3.2.1 IR-SEC Studies

Steady state IR-SEC measurements were performed to examine changes in the IR spectra

due to oxidation and reduction of the system (Figure 3.2) and to facilitate assignments in

the 2DEV spectra discussed below. Upon oxidation, new bands at 1636, 1614, and 1535

cm^{-1} appeared (Figure 3.2a). These frequencies are similar to those observed in

pyridinium salts, $C_5H_5NH^+$ (1635, 1610 cm, and 1535 cm^{-1}), and are assigned to the

PyrH$^+$ ring stretching modes.[25,26] Therefore, these bands serve as markers for double

proton transfer (2PT). Upon reduction (Figure 3.2b), a band at 1593 cm^{-1} emerges, which

is assigned to the formation of a porphyrin anion as observed in previous studies.[23,27] This

band then serves to track ET. The oxidative IR-SEC measurements indicate the location

of the translocated protons in the E2PT product, and the reductive IR-SEC measurements

identify the porphyrin anion radical in the E2PT product.
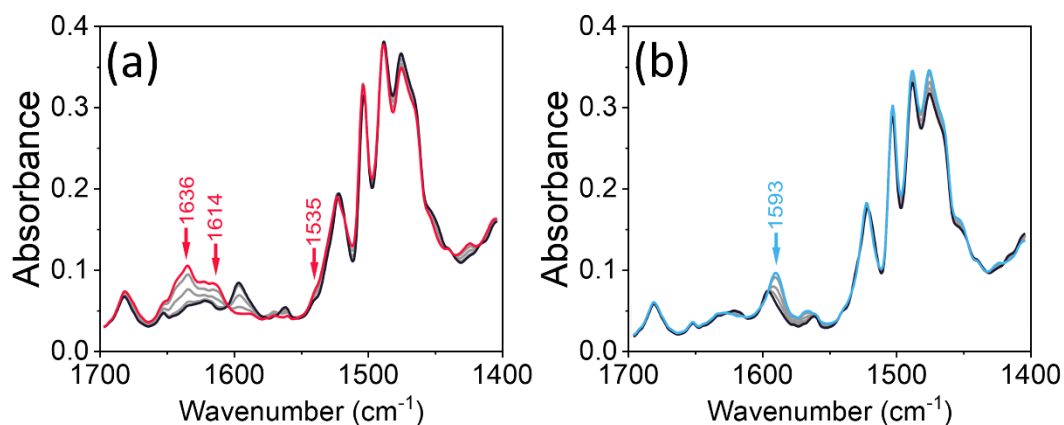
Figure 3.2 IR-SEC spectra of **PF$_{15}$-BIP-Pyr** upon (a) oxidation and (b) reduction. The

black curves show the neutral species and colored curves show oxidized (red) and reduced

species (blue). Spectra were recorded in dry deuterated acetonitrile solution with 0.1 M

TBAPF$_6$.

The $E_{1/2}$ for the **PF₁₅-BIP-Pyr⁺/PF₁₅-BIP-Pyr** and **PF₁₅-BIP-Pyr/PF₁₅-BIP-Pyr⁻**

redox couples were estimated to be +0.85 and -0.83 V versus the standard calomel

electrode (SCE), respectively, by cyclic voltammetry measurements (Figure 4.16). The $E_{1/2}$

of a reference compound which can only undergo one electron, one proton transfer (E1PT)

(**BIP-Pyr⁺/BIP-Pyr**) was measured to be 1.01 versus SCE.[28]

3.2.2 2DEV Studies

Briefly, in a 2DEV experiment, visible excitation pulses prepare an ensemble of

electronic/vibronic states that evolve as a function of waiting time, *t*, which are tracked via

an IR detection pulse (see Chapter 4.3 for experimental details). The resulting spectra,

collected by collaborators from University of California at Berkeley, are then presented as

(visible) excitation frequency-(IR) detection frequency correlation plots at given waiting

times, allowing for the correlation between electronic and vibrational degrees of freedom

to be followed directly. This correlation can be quantitatively described by the center line

slope (CLS) of the spectra features, which is related to a cross correlation of vibrational

and electronic dipoles.[21,29] As a result, this quantity is highly sensitive to both dynamical

changes in the electronic structure and the mixing of vibronic states.[23,30–32]

Figure 3.3 shows representative 2DEV spectra for **PF₁₅-BIP-Pyr**. Immediately after

photoexcitation, ground state bleach features were observed at 1505, 1524, 1537, and

1564 cm⁻¹, while photoinduced absorption (PIA) features were observed at 1514, 1530,

1544, 1586, 1604, 1627, 1648, 1665, 1682, and 1694 cm⁻¹. Below ~1540 cm⁻¹, the

observed spectral features reflect those of PF₁₅.[23] However, distinct bands at 1586, 1604,

and 1627 cm⁻¹ were observed in the 2DEV spectra of this species, **PF₁₅-BIP-Pyr**, and are

ascribed to ET (1586 cm⁻¹) and 2PT (1604 cm⁻¹ and 1627 cm⁻¹) based on the IR-SEC
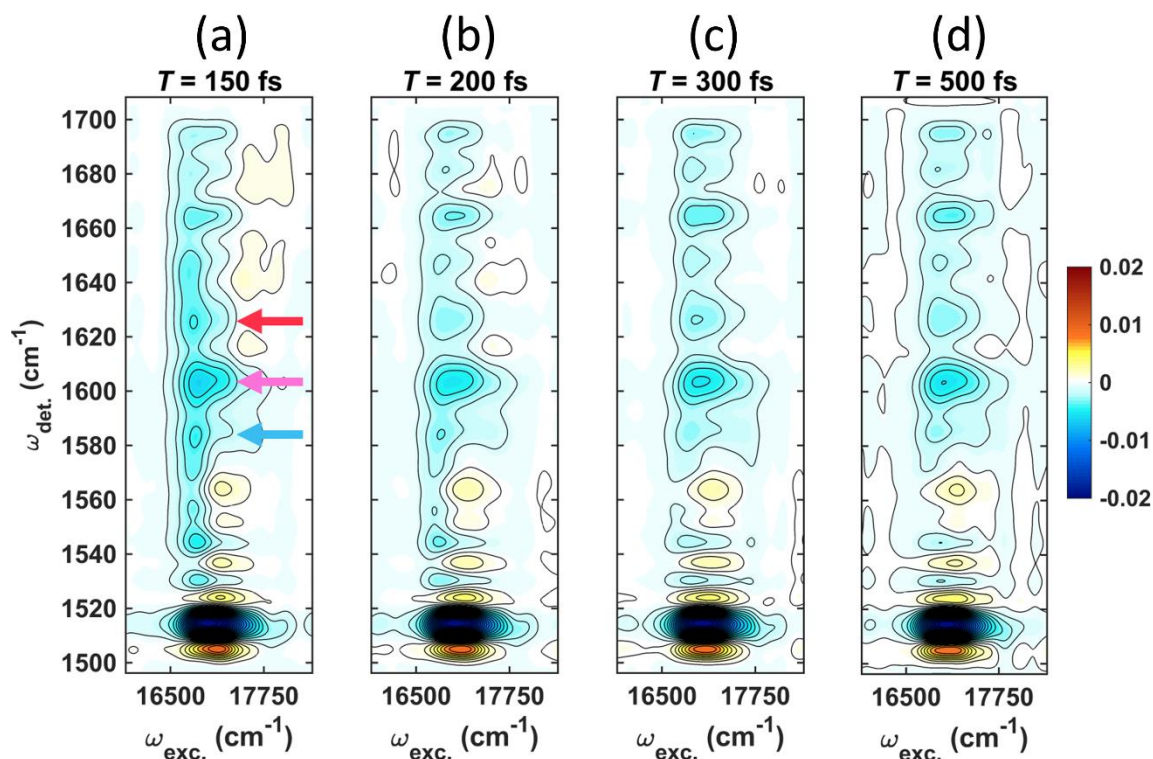
Figure 3.3 (a)-(d) 2DEV spectra of **PF$_{15}$-BIP-Pyr** in deuterated acetonitrile at t = 150 fs, 200 fs, 300 fs, and 500 fs, respectively. Positive signals (red/yellow contours) indicate ground state bleaches and negative signals (blue contours) represent photoinduced absorptions (PIAs). Contour levels are drawn in 5% intervals. Arrows indicate the main PIA features of interest at 1586 cm^{-1} (ET, blue), 1604 cm^{-1} (2PT, pink), and 1627 cm^{-1} (2PT, red), respectively.

measurements, indicating the formation of the E2PT product following photoexcitation. Additional PIAs were observed at >1630 cm^{-1} and are very likely related to the E2PT product based on similarities in the observed dynamics. Although only slight spectral evolution was observed in this region in the IR-SEC measurements (Figure 3.2), the E2PT product in the 2DEV measurements is formed on the excited state potential surface, so a complete agreement in the signals independently observed on each experiments is

not expected. The dynamics of the features at 1586, 1604, and 1627 cm^{-1}, corresponding to the most significant changes in the IR-SEC measurements, will be the focus for the remainder of the discussion. It is noted that the observed appearance of these bands within ~90 fs (the instrument response function) suggests, based on the free energy difference between E1PT and E2PT products (more driving force for E2PT by ~160 meV), that the E1PT is only transiently formed (<90 fs), if at all. As it will be shown, analysis of the 2DEV spectral dynamics reveals that it is very unlikely the E1PT product is ever formed.

To understand the dynamics of the ultrafast, nonequilibrium formation of the E2PT product, the following analysis can be made: the excitation frequency ($\omega_{exc.}$) peak evolution at specific detection frequencies corresponding to either the 2PT or ET signals (Figure 3.4a, Figure 4.18 for raw data). It is found that the $\omega_{exc.}$ peak evolution for these features exhibits significant changes within the first few hundred femtoseconds (Figure 3.4a). This is in stark contrast to features that are specific to PF$_{15}$ (1505 and 1514 cm^{-1}),[23] not relevant to the E2PT product, which do not show any dynamics along $\omega_{exc.}$ during the waiting time (Figure 4.18 and Figure 4.19). The evolution of the 2PT and ET signals, however, is striking in that the $\omega_{exc.}$ peak evolution appears to undergo a ~200 cm^{-1} blue-shift (from ~1.72×10^4 cm^{-1} to values under ~1.70×10^4 cm^{-1}), contradictory to the expected energetic relaxation from the Franck-Condon region due to either electronic or solvent rearrangement. The observed dynamics can be rationalized by viewing the observed $\omega_{exc.}$ peak evolution not as a blueshift but rather as the result of a modulation by a low frequency vibrational mode. This is reminiscent of a previous 2DEV study which revealed that a low-frequency vibrational mode can influence the $\omega_{exc.}$ peak evolution if it is coupled to both the excited electronic
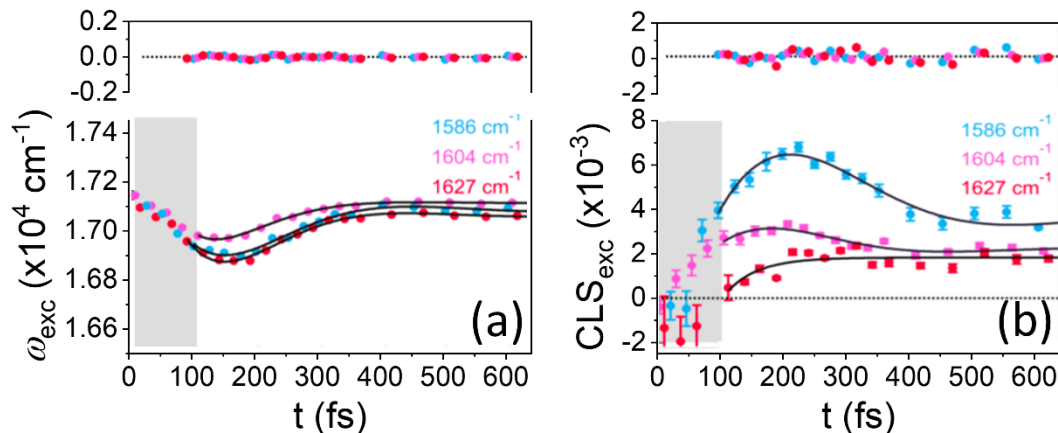
Figure 3.4 (a) $\omega_{exc.}$ peak evolution of **PF₁₅-BIP-Pyr** at 1586 cm⁻¹ (ET, blue), 1604 cm⁻¹ (2PT, pink), and 1627 cm⁻¹ (2PT, red). Solid black lines indicate the fit results (listed in Table 3.1). (b) Center line slope (CLS) dynamics of **PF₁₅-BIP-Pyr** at 1586 cm⁻¹ (ET, blue), 1604 cm⁻¹ (2PT, pink), and 1627 cm⁻¹ (2PT, red). Solid black lines indicate the fit results (listed in Table 3.2). In panels a and b, the time range in which visible and IR pulses overlap, <90 fs, is indicated by the shaded area.

state and the probed vibrational mode.[33] Indeed, it is found here that the dynamics of the $\omega_{exc.}$ peak evolution fit well and consistently to a damped cosine function (results shown in Table 3.1) and not to a mono- or bi-exponential function. From Table 3.1, it is apparent that the three bands yield nearly identical fits, where the average values for the frequency and damping time of this low-frequency mode were found to be 55 ± 2 cm⁻¹ and 112 ± 12 fs, respectively.

In a first-principles molecular dynamics study of the nonequilibrium PCET dynamics of a BIP construct by Goings and Hammes-Schiffer, the vibrational modes most crucial to the proton transfer process were predicted.[24] In particular, a slow bending mode in the plane of the BIP subunit, found to dominate the inner sphere reorganization, was identified as the

Table 3.1 Parameters from fit of $\omega_{exc.}$ peak evolution (see Figure 3.4a) to damped cosine function ($f = A_0 + A_1 \cos(\omega_1 t + \varphi_1) e^{-t/\tau_1}$).

	A_0	A_1	ω_1 (cm^{-1})	φ (deg)	τ_1 (fs)
1586 cm^{-1} (ET)	17090	675	56 ± 3	57 ± 7	140 ± 30
1604 cm^{-1} (2PT)	17127	1121	51 ± 5	57 ± 4	86 ± 15
1627 cm^{-1} (2PT)	17068	923	58 ± 2	49 ± 3	110 ± 13

most important vibration for facilitating proton transfer. For the **BIP-Pyr** species (the one under investigation here but without the PF$_{15}$ group), the frequency of this vibrational mode was determined to be 45 cm^{-1}, specifically corresponding to an in-plane bending motion that modulates the PT distances following oxidation. Despite the fact that the present investigation features the inclusion of a photoactive, electron accepting PF$_{15}$ group and is in solution rather than in the gas phase, the presence of a low frequency vibration with a similar frequency, 55 ± 2 cm^{-1}, is nevertheless identified in the dynamics of the nonequilibrium PCET pathway. Therefore the observed vibration is assigned as an in-plane bend localized on the **BIP-Pyr** which, when damped, promotes 2PT (where it is noted that the localized character of this mode is further supported by the lack of any $\omega_{exc.}$ peak evolution displayed by modes specific to the PF$_{15}$ moiety as discussed above and shown in Figure 4.19 and Figure 4.20). It is emphasized that the 55 cm^{-1} mode specifically promotes the formation of the E2PT product (*i.e.*, involves double proton translocation), which suggests that the E1PT product is not formed or at most transiently populated during the reaction.

An additional important distinction to note between the previous theoretical study and

this experimental work involves the ET process. In the work of Goings and Hammes-Schiffer, the oxidation process was treated by instantaneously removing an electron from the system. However, in the photoactive E2PT species investigated here, the nonequilibrium pathway does not undergo instantaneous ET. Rather, initial photoexcitation corresponds to a π to π^* electronic transition on the porphyrin, followed by an ultrafast, nonequilibrium evolution of protons and electron density giving rise to the E2PT process. It is also found experimentally that both the ET and 2PT features are modulated by the low-frequency mode. In fact, the frequencies and phase shifts extracted from the fit to a damped oscillator are nearly identical (Table 3.1). The agreement in the phase shift in particular constitutes strong evidence that the transfers of the electron and two protons are concerted, even on ultrafast timescales. In addition, the error in the phase shifts can be used to estimate the degree of concertedness of the E2PT product formation. On the basis of the average frequency of the low-frequency mode, 55 ± 2 cm^{-1}, and the largest error in the phase, $\pm 7°$, we can estimate that the error in the delay between the ET and 2PT features is ~24 fs, which is interpreted to mean that the ultrafast motion of the electron and two protons is concerted within an uncertainty of ~24 fs.

Turning to the CLS, it is possible to understand how the coupling of this vibration to the PET state gives rise to vibronic mixing and influences the correlation between the electronic and vibrational degrees of freedom that are directly interrogated. Figure 3.4b shows the CLS dynamics of the ET and 2PT features. The CLS dynamics observed are strikingly similar to the $\omega_{exc.}$ peak evolution, notably the modes at 1586 and 1604 cm^{-1}. The discrepancy in the CLS dynamics of the feature at 1627 cm^{-1}, which are shown for completeness in Table 3.2, could be due to differences in the degree of coupling between

71

this mode and the low-frequency mode which is known to drastically influence the CLS.[30] Another possibility is that peak overlap from weak positive features just above and below 1627 cm^{-1} could obscure the CLS dynamics of this mode. Both of these possibilities are supported by the fact that there is agreement between the $\omega_{exc.}$ peak evolution for this feature and the modes at 1586 and 1604 cm^{-1} (Table 3.1) despite the discrepancy in the CLS dynamics. Focusing on the modes at 1586 and 1604 cm^{-1}, and utilizing a damped cosine fit function, an average frequency is obtained for the CLS dynamics of 55 $\pm$ 9 cm^{-1} and damping time of 165 $\pm$ 60 fs, which are in agreement with the values obtained for the $\omega_{exc.}$ peak evolution (see Table 3.2 for complete fit details). This indicates that the same vibrational mode is driving the CLS as was observed in the $\omega_{exc.}$ peak evolution. Because the CLS is related to a cross correlation of electronic and vibrational dipoles, it is possible to understand the non-zero CLS in this case as arising from vibronic mixing, which significantly alters the transition moments.[23,30] In contrast, the CLS of the bands specific to PF$_{15}$ (1505 and 1514 cm^{-1}),[23] which are not relevant to the E2PT product, were

Table 3.2 Parameters from fit of CLS dynamics (see Figure 3.4b) to damped cosine function ($f = A_0 + A_1 \cos (\omega_1 t + \varphi_1) e^{-t/\tau_1}$).

	A_0	A_1	ω_1 (cm^{-1})	φ (deg)	τ_1 (fs)
1586 cm^{-1} (ET)	0.27	0.73	48 $\pm$ 8	220 $\pm$ 10	180 $\pm$ 50
1604 cm^{-1} (2PT)	0.39	0.61	61 $\pm$ 9	210 $\pm$ 13	150 $\pm$ 70
1627 cm^{-1} (2PT)^a	0.11	-0.89	--	--	50 $\pm$ 23

^{a} The CLS dynamics for this mode were unable to be fit to a damped cosine function.

essentially constant over the observation time window (Figure 4.17). It is concluded that the ultrafast Grotthuss-type process in this system is driven by highly correlated electronic and nuclear evolution arising from vibronic mixing.

Interestingly, the CLS dynamics for this species differ significantly from those observed previously for **PF₁₅-BIP** (an E1PT only system). In that case, the CLS dynamics reflected a monotonic rise on a timescale estimated to be 120 fs which was assigned to the evolution from the Frank-Codon region of the locally excited (LE) state to the minimum of the E1PT state, accompanied by a twisting of the dihedral angle between BIP and porphyrin moieties from 60° to 90°.[23] This dihedral twisting was found to result in an increase in the electronic dipole moment, which in turn drove the observed rise in the CLS. To rationalize and gain further insight into the differences in the PCET reaction in **PF₁₅-BIP** versus **PF₁₅-BIP-Pyr**, dipole moments of the E2PT state of the latter were calculated as a function of dihedral angle between BIP and porphyrin moieties over the same range. One can see that electronic dipole moment again shows a concomitant increase with the dihedral angle, and reaches a maximum at 90°. However, in addition, near the Franck-Condon region (*i.e.*, with dihedral angle fixed to that of the ground-state, ~60°), 2PT is found to correspond to ~80% ET. Thus, the E2PT system has a larger degree of charge transfer character near the Franck-Condon region compared to that in **PF₁₅-BIP** (~50%).[23]

The **PF₁₅-BIP-Pyr** molecule illustrates an optically triggered Grotthus-type mechanism for the transfer of two protons and one electron. As in the case of one-proton, one-electron transfers (E1PTs),[23] it is found here an ultrafast, nonequilibrium channel for E2PT, enabling the reaction to be followed in real time (cartoon representation shown in Figure 3.5). No evidence is found for a single proton transfer intermediate, and the
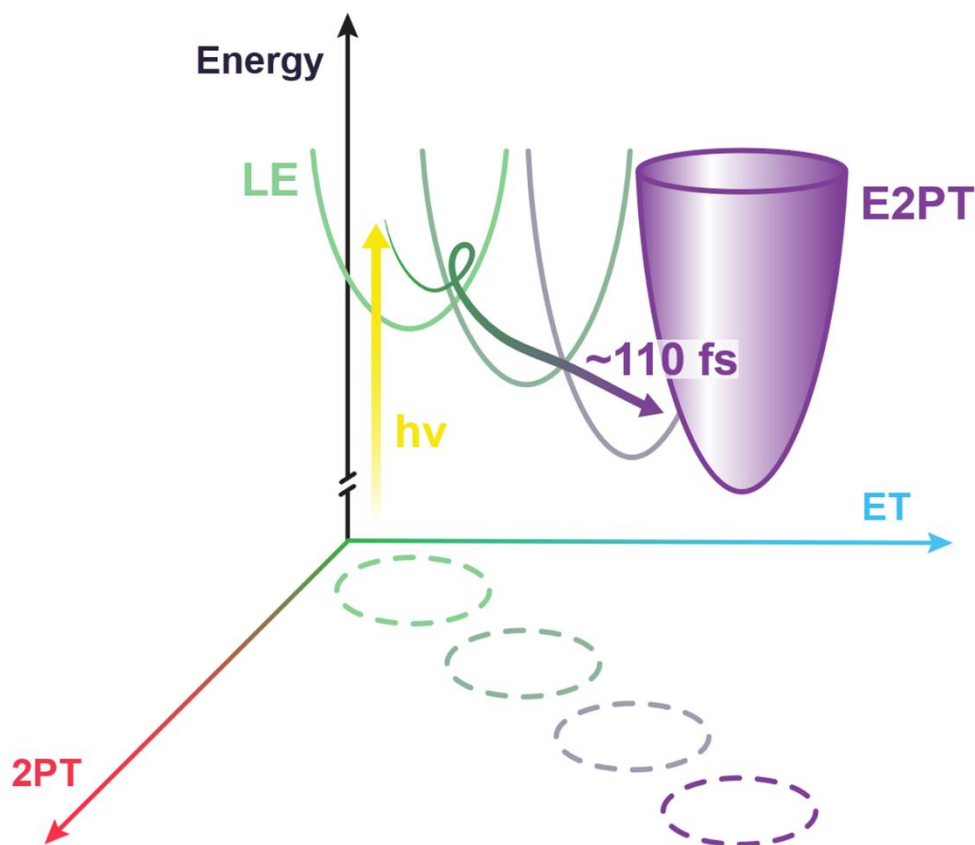
Figure 3.5 Cartoon schematic of the ultrafast, nonequilibrium dynamics of the Grotthus-type proton wire as a function of the double proton transfer (2PT) and electron transfer (ET) coordinates. Following photoexcitation (yellow arrow), the system is led to the unrelaxed Franck-Condon region where concerted 2PT and ET leads to formation of the E2PT product on a ~110 fs timescale. The concerted electron-nuclear motion is promoted by the damping (purple end of the arrow) of a low frequency vibration (green end of the arrow) localized in the BIP-Pyr moiety.

process is facilitated by a low-frequency mode as suggested by Goings and Hammes-Schiffer in a recent theoretical study of a related molecule.[24] This modulation of the interproton distances produces a damped cosinusoidal oscillation of the mid-IR modes

assigned to the 2PT and ET components of the E2PT process, clearly demonstrating the involvement of vibronic coupling in the dynamics. Fits of the $\omega_{exc.}$ peak evolution for the modes tracking 2PT and ET reveal identical (within error) phases for the low frequency oscillation. This, in turn, enables an estimate of the maximum possible delay between the ET and 2PT processes, *i.e.*, the degree to which the ET and 2PT processes are concerted. The error bounds on the phase in Table 3.1 have a maximum value of $\pm 7°$, which given the frequency of ~55 cm^{-1}, translates to a maximum delay of ~24 fs between the ET and 2PT processes. A more precise delineation of "concertedness" is likely not warranted because the electron distribution progressively evolves until it roughly corresponds to one whole electron transferred to the porphyrin moiety.[23] Although not reported at this time, photochemically driven translocations over nanoscale distances should be possible in extended versions of this genre of constructs, and further spectroscopic studies are likely to significantly advance our understanding of the dynamics governing such systems if an optical trigger can be incorporated.[24,34-39]

3.3 Results and Discussion: Redox Potential Tuning Of Electron-coupled Proton Transfers With Electron-withdrawing Groups

There have been reports of the design of a PCET-driven, Grotthuss-type hydrogen-bonded network that serves as a proton wire and models systems found in nature for proton transport.[28,35,37,39,40] However, this model system exposed an unexpectedly strong dependence of the $E_{1/2}$ of the redox couple driving the process on the number of Grotthuss-type proton donor-acceptor units involved in the proton wire. Indeed, the redox potential driving proton translocation over ~16 Å was found to be ~300 mV lower than the redox potential of the PCET process that initiated the Grotthuss-type process.[35] This

loss in redox potential in a model system accompanying Grotthuss-type proton translocation raises questions fundamental to bioenergetics involving the coupling of redox processes to proton currents to generate PMF.

Figure 3.6 displays the molecular structures of the proton wires, showing the number of protons to be transferred upon electrochemical oxidation, *i.e.*, from the simplest case E1PT (models **1**/**1′**), the intermediate length E2PT (models **2**/**2′**), and the longest proton wire capable of one-electron, three-proton transfers (E3PT, models **3**/**3′**). Both molecules **3** and **3′** have three distinguishing components: (*i*, red) a phenol moiety (the oxidation center) that serves simultaneously as an electron donor and the first proton donor; (*ii*, blue) a benzimidazole-based bridge containing two benzimidazoles covalently connected and electronically linked to act as a proton relay; and (*iii*, green) a TPA that ends the

R = -H (series **1-3**), -CF$_3$ (series **1′-3′**)

C H O N

1, 1′   2, 2′   3, 3′
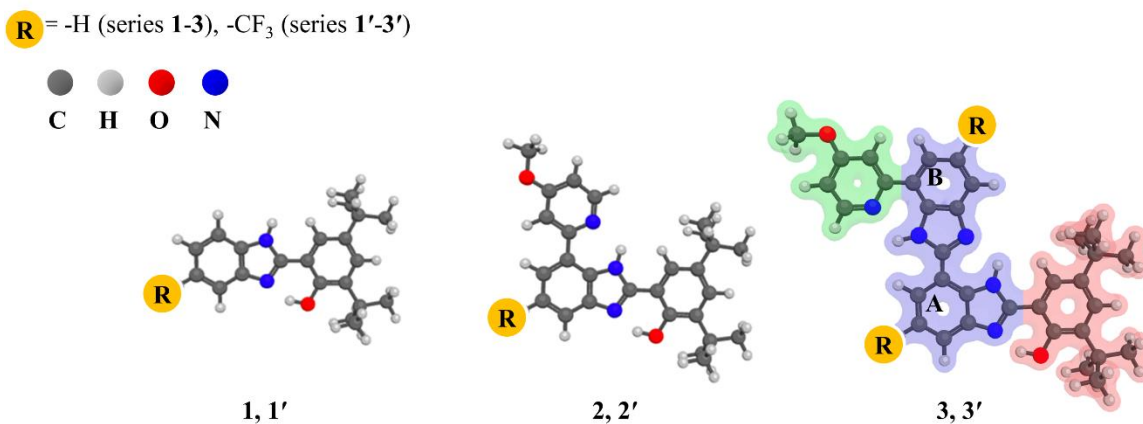
Figure 3.6 Molecular structures of the compounds presented in this work. R = CF$_3$ denotes the series of compounds containing the trifluoromethyl substituent (**1′**–**3′**), R = H denotes the analogous, unsubstituted compounds (**1**–**3**). The different components of the proton wire (color coded) are described for molecules **3**/**3′**: the oxidation center in red, the benzimidazole-based bridge in blue, the terminal proton acceptor in green, and the substituted site in yellow.

proton relay after accepting the final benzimidazole proton. The difference between the series **1**–**3** and **1′**–**3′** is the substituted R-group on the benzimidazole moiety.

The one-electron oxidation of the oxidation center leads to a dramatic decrease in the phenol pKa (from 10 to -2),[9,41,42] resulting in deprotonation and fast transfer of the phenolic proton to either the bulk solution or the nearest basic site. In BIP-based systems, both the spatial proximity of the benzimidazole nitrogen and the strong hydrogen bond between the phenol oxygen and the benzimidazole nitrogen provide a well-defined, intramolecular proton transfer coordinate.[38] This pathway and its connectedness impact the electrochemical reversibility of the phenoxyl radical/phenol redox couple. The two *tert*-butyl groups are strategically placed to impart stability to the phenoxyl radical and prevent undesired reactions such as dimerization.[43]

On the other hand, the TPA is the end point of the series of the proton translocation steps (for EnPT process with $n \geq 2$) initiated upon electrochemical oxidation of the phenol. Substituents potentially selected as the TPA should satisfy the following requirements: *(a)* have sufficiently high pK_a, *(b)* form a strong intramolecular hydrogen bond with the benzimidazole NH, *(c)* be electrochemically inactive in the vicinity of the phenol oxidation potential, *(d)* be chemically stable during both standard purification procedures and the required experimental time-scales, and *(e)* display both detectable and characteristic spectroscopic signatures once protonated. Substituted pyridines fulfill all these requirements and allow to spectroscopically monitor the formation of the oxidized species through the characteristic vibrational modes of the protonated pyridine.[26,44]

Finally, a key component of the proton wire is the benzimidazole-based bridge, which is not an innocent participant in the PCET process. Cyclic voltammetry studies have

shown that the addition of each benzimidazole unit lowers the redox potential of the

phenoxyl radical/phenol couple by a nearly constant value of ~60 mV, regardless of the

nature of the TPA group.[37]

3.3.1 Synthesis and Structural Characterization

Molecules capable of an E1PT process, **1** and **1′**, were synthetized and characterized in

previous reports.[39,45] Among the molecules featuring an E2PT mechanism, the reference

compound **2** was previously reported,[28] while its trifluoromethylated version **2′** has been

obtained following a 5-step synthetic scheme, starting with the commercially available 3-

bromo-5-(trifluoromethyl)benzene-1,2-diamine. Compound **3** was prepared using

precursors previously reported, whereas the high potential proton wire **3′** has been

synthesized in an overall 10-step synthetic scheme, beginning the synthesis with the

commercially available 2-amino-3-nitro-5-(trifluoromethyl)benzoic acid. Compounds **2'**,

3, and **3'** were prepared by collaborators from Arizona State University.

   In molecules **3/3′**, all three components described above are covalently connected so

that the phenolic proton and the two benzimidazole NH groups form an extended

hydrogen-bonded network. Similar to other BIP based constructs, the hydrogen-bonded

network is defined by the presence of strong hydrogen bonds between the acidic and

basic sites. The electron-withdrawing properties of the trifluoromethyl group impact the

overall electron distribution of the entire molecule and specifically the strength of the

hydrogen bonds.

   The electron-withdrawing character of the trifluoromethyl group at the 5-position of

benzimidazole A (Figure 3.6) induces an upfield shift of the phenolic proton resonance

(δ_{OH}) in the NMR spectrum, in comparison with the δ_{OH} found for its analogue **3** (13.00

ppm for **3'** *vs* 13.29 ppm for **3** in CDCl$_3$). Accordingly, the decrease in the electron density on the heterocycle ring due to the electron-withdrawing effect of the trifluoromethyl group weakens the intramolecular O$_1$–H$\cdots$N$_2$ hydrogen bond (Figure 3.7).

On the other hand, the electron-withdrawing effect is also manifested in benzimidazole B (Figure 3.6). In this case, a downfield shift is observed in the resonance of the benzimidazole NH (δ_{NH}) hydrogen bonded with the pyridinic nitrogen (N$_5$–H$\cdots$N$_6$) of the TPA, suggesting a stronger hydrogen bond compared to that of **3** (δ_{NH} = 12.68 ppm for **3'** *vs* 12.46 ppm for **3** in CDCl$_3$). Based on the chemical shifts, the intramolecular
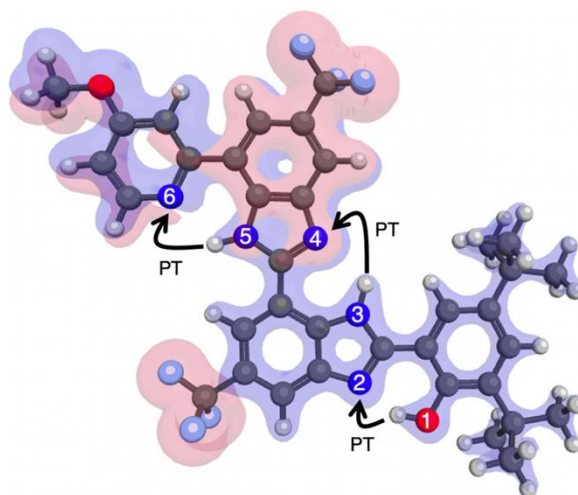
Figure 3.7 Calculated molecular structure of **3'** and electron density difference with respect to **3**. The red/blue isosurfaces show an increase/decrease in the electron density due to the substitution of the trifluoromethyl groups with an isosurface value of 0.05 au for this electron density difference. The trifluoromethyl groups draw significant electron density out of the proton wire and the phenol. The calculated excess partial charge on each of the trifluoromethyl groups is –0.231 au. The proton transfer processes are labeled as PT.

hydrogen bond connecting both benzimidazoles (N_3–H$\cdots$N$_4$) is only slightly affected by the presence of both trifluoromethyl groups on the benzimidazole-based bridge. The effects seen in **2′** and **2** are similar to those described above for **3′** and **3**. The trifluoromethyl group present in **2′** weakens the hydrogen bond between the phenol and the benzimidazole N (δ_{OH} = 13.48 ppm and 13.12 ppm in CDCl$_3$ for **2** and **2′**, respectively) and strengthens the hydrogen bond between the benzimidazole NH and the pyridinic nitrogen of the TPA (δ_{NH} = 12.36 ppm and 12.52 ppm in CDCl$_3$ for **2** and **2′**, respectively). The same behavior has been observed and described in the case of the simplest models **1** and **1′**.[45] In summary, the trifluoromethyl group affects the strengths of the hydrogen bonds but does not seem to drastically modify the hydrogen bond donating/accepting capability of the benzimidazole, which is indispensable for a successful proton relay mechanism.

3.3.2 Electrochemical Studies

Figure 3.8 shows the cyclic voltammograms recorded using the unsubstituted reference molecules **1**–**3** and bridge-modified molecules **1′**–**3′**. Experimental and calculated $E_{1/2}$ values for the phenoxyl radical/phenol couple, together with other relevant electrochemical parameters, are summarized in Table 3.3. For all the compounds, the experimental $E_{1/2}$ values were taken as the average of the anodic and cathodic peak potentials swept over the phenoxyl radical/phenol couple. Each calculated $E_{1/2}$ was obtained using the lowest free energy intramolecular proton transfer state. For all systems, it was found that the most stable (lowest free energy) oxidized state involved the transfer of all protons, *i.e.*, one proton transfer in **1/1′**, two proton transfers in **2/2′**, and three proton transfers in **3/3′**. The quasi-reversible one-electron electrochemical oxidation
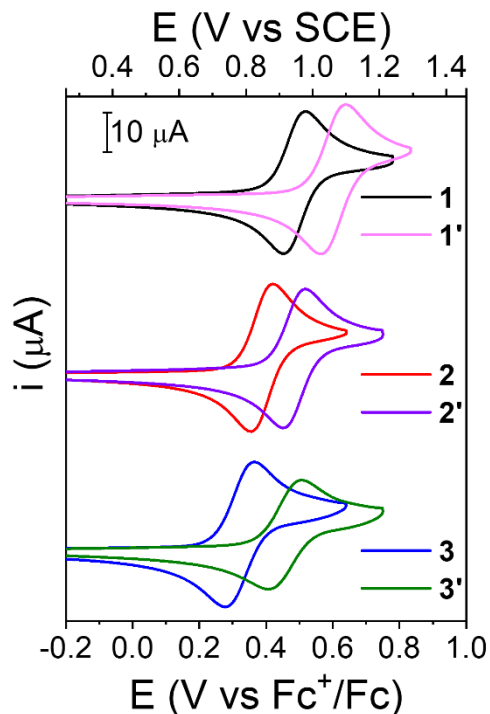
Figure 3.8 Cyclic voltammograms of unsubstituted molecules **1**–**3** and bridge-modified molecules **1′**–**3′**. Concentration: 1 mM of the indicated compound, 0.1 M TBAPF$_6$ as supporting electrolyte in dry CH$_2$Cl$_2$. WE: glassy carbon. RE: Ag wire (ferrocenium/ferrocene redox couple as an internal reference). CE: Pt wire. Scan rate, 100 mV s^{-1}.

of the phenol moiety is observed in all systems, independent of the presence of the trifluoromethyl substitution and the extension of the proton relay system (*i.e.*, the length of proton translocation distance).

For the unsubstituted molecules (**1**–**3**), the progressive drop in $E_{1/2}$ along the series follows the same trend observed for the analogous systems bearing TPAs different than pyridine.[37] In the case of the bridge-modified series **1′**–**3′**, the incorporation of the trifluoromethyl group dampens this drop in $E_{1/2}$ between **2′** and **3′**, *i.e.*, for the

81

unsubstituted molecules, the $\Delta E_{1/2}$ between **2** and **3** is 70 mV, while for the analogous

molecules having the trifluoromethyl group(s) (**2′** and **3′**) the $\Delta E_{1/2}$ is only 20 mV (Table

3.3 and Figure 4.21).

Importantly, the $E_{1/2}$ is always higher for the constructs bearing the trifluoromethyl

group(s) in comparison with their non-trifluoromethylated analogues.

The much smaller drop in $E_{1/2}$ between **2′** and **3′** can be described to the combination of

two effects acting in opposite directions: *(i)* expansion of the proton wire as a

consequence of the second benzimidazole addition leads to the decrease of $E_{1/2}$ and *(ii)*

incorporation of the trifluoromethyl groups in the benzimidazole-based bridge affects the

overall electron density of the system and increases the $E_{1/2}$. Figure 3.7 shows the

redistribution of electron density as a result of introducing the trifluoromethyl groups. As

shown elsewhere, the benzimidazole bridges are non-innocent participants in the PCET

process. The addition of each benzimidazole unit lowers the redox potential of the

phenoxyl radical/phenol couple regardless of the nature of the TPA group. These results

were rationalized in terms of the electronic structure of the linked benzimidazole groups

and their partial conjugation with the phenol.[37] In **1**–**3** and **1′**–**3′**, a progressive red shift in

the UV-Vis absorption spectrum (Figure 4.22) is evidence of the partially conjugated

framework.

On the other hand, the trifluoromethyl groups draw electron density out of the phenol

moiety where electrochemical oxidation originates, making it more difficult to remove an

electron (Figure 3.7 and Table 4.4). This effect counterbalances the drop in $E_{1/2}$ arising

from the extended conjugation. Additionally, withdrawal of electron density from the

phenol also weakens the O_1–H···N_2 hydrogen bond, in agreement with previously

Table 3.3 Electrochemical Data of Unsubstituted Molecules **1**–**3** and Bridge-Modified Molecules **1'**-**3'** in CH_2Cl_2.

Compound	Experimental $E_{1/2}$ (V *vs* Fc⁺/Fc)	Experimental $E_{1/2}{}^a$ (V *vs* SCE)	Calculated $E_{1/2}{}^b$ (V *vs* SCE)	$\Delta E_p{}^c$ (mV)	$i_c/i_a{}^c$
1	0.49[d]	0.95[d]	1.11	70[d]	0.95[d]
2	0.39[d]	0.85[d]	0.85	70[d]	0.90[d]
3	0.32	0.78	0.72	80	0.99
1'	0.60[e]	1.06[e]	1.20	80[e]	0.96[e]
2'	0.48	0.94	0.94[f]	70	0.99
3'	0.46	0.92	0.82	90	0.94

[a] The potential of the RE was determined using the ferrocenium/ferrocene redox couple as an internal standard and adjusting to the SCE scale (with the ferrocenium/ferrocene $E_{1/2}$ taken to be 0.46 V *vs* SCE in CH_2Cl_2).[46]

[b] Each computed redox potential is calculated using the maximum number of intramolecular proton transfers, which is consistently the lowest free energy isomer for the oxidized state. The redox potentials corresponding to the intermediates that would arise from only some of these proton transfers are given in Table 4.4.

[c] Peak to peak separation (ΔE_p) and cathodic to anodic peak intensity ratios (i_c/i_a) measured at a scan rate of 100 mV s⁻¹.

[d] Values from ref. 28.

[e] Values from ref. 45.

reported BIP based systems, in which a clear trend between $E_{1/2}$ and hydrogen bond strength was observed, *i.e.*, the weaker the intramolecular hydrogen bond, the higher the $E_{1/2}$ value.[34,45] It is worth comparing the $E_{1/2}$ for **1** and **3′**, *i.e.*, the simplest and most elaborate models within the series, respectively. The unsubstituted system can only perform an E1PT process (**1**), and the extended molecule, bearing the pyridine TPA and the trifluoromethyl groups, can translocate three protons in an E3PT process (**3′**). The redox potential for **1** is $E_{1/2} = 0.95$ V *vs* SCE (Table 3.3), while for the more complex molecule **3′**, the $E_{1/2}$ is similar (0.92 V *vs* SCE, Table 3.3) but **3′** translocates three protons instead of one over ~11 Å. In other words, the energetic cost required for the E3PT process in the trifluoromethylated proton wire **3′** is almost the same as that needed for the E1PT process in **1**. This observation highlights the role of the trifluoromethyl groups in conserving the redox potential as the proton wire is extended.

3.3.3 IR-SEC Studies

IR-SEC is used to track in-situ the product(s) of the electrochemical oxidation/reduction process. The IR-SEC of **1**, **1′** and **2** in CH_2Cl_2 solution were reported in previous work[28,39,45] and serve as models to interpret the IR-SEC experiments of the more complex constructs **3** and **3′**. The IR-SEC of **2′** (Figure 3.9) closely resembles the results obtained for **3′** (*vide infra*). For this reason, our discussion will focus on molecules capable of performing the E3PT process. Considering that compounds **3/3′** are structurally similar, the vibrational modes of the neutral species are expected to have similar key features. Moreover, the spectral changes upon oxidation of the phenol should also coincide because the multiproton translocation process leads to structurally similar phenoxyl radicals and protonated TPA species in both compounds. For example, in the 1700−1400

84
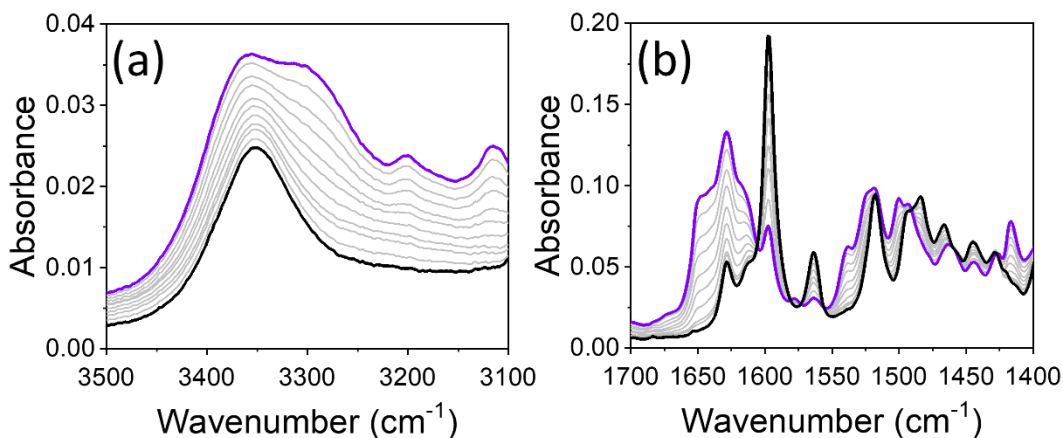
Figure 3.9 IR-SEC spectra of **2′** recorded in the (a) 3100−3500 cm^{-1} and (b) 1700−1400 cm^{-1} regions. Black traces represent the spectrum of the neutral species. Purple traces show the resulting spectrum of oxidized species after bulk electrolysis, while grey traces display intermediate situations. Solvent: dry CH_2Cl_2, 0.1 M TBAPF$_6$.

cm^{-1} frequency region of the spectrum of both molecules, the bands at 1596, 1563 cm^{-1} for **3** (Figure 3.10d), and 1598, 1565 cm^{-1} for **3′** (Figure 3.10b) are attributed to the ring stretching modes of the pyridyl group.[28,46–48] These bands gradually decrease upon oxidative polarization, and new bands in the region above 1600 cm^{-1} appear in both cases, the bands associated with the pyridinium ion are 1615, 1639 and 1649 cm^{-1} for **3** (Figure 3.10d), and 1628 and 1651 cm^{-1} for **3′** (Figure 3.10b). Tracking the formation of the which are assigned to the vibrational modes of protonated pyridine.[26,28,44] Specifically, stretching mode frequency (ν_{NH}) region 3500−3100 cm^{-1} of the spectrum. The frequency of this band is sensitive to the intramolecular hydrogen bond strength in these constructs. For both molecules the ν_{NH} is located at ~3370 cm^{-1}, clearly oxidized product is also possible by monitoring the changes in the benzimidazole NH different from that observed for either of the reference compounds **1** or **1′**, which display no internal hydrogen-bonded

85
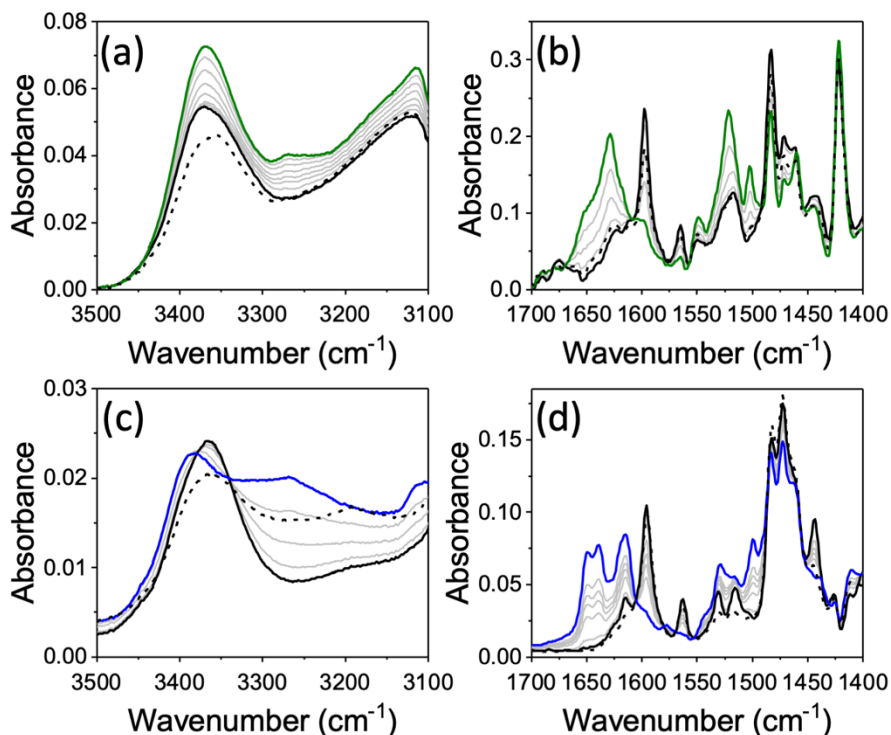
Figure 3.10 IR-SEC spectra of **3′** recorded in the (a) 3500−3100 cm^{-1} and (c) 1700−1400 cm^{-1} regions, and of **3** recorded in the (c) 3500−3100 cm^{-1} and (d) 1700−1400 cm^{-1} regions. Black traces represent the spectrum of the neutral species. Green and blue traces show the resulting spectrum of oxidized species after bulk electrolysis for **3'** and **3**, respectively, while grey traces display intermediate situations. Black dashed lines correspond to the spectrum obtained upon polarizing the solution to reducing potentials after oxidizing for 2 min at a potential required to deplete **3′** and **3** on each case. Solvent: dry CH$_2$Cl$_2$, 0.1 M TBAPF$_6$.

NH (ν_{NH} = 3414 cm^{-1} and ν_{NH} = 3404 cm^{-1}, respectively).[39,45] Following electrochemical oxidation, the intensity of ν_{NH} decreases and a small shift towards higher frequency (from 3367 to 3381 cm^{-1}) is observed for **3** (Figure 3.10c), while an increase in its intensity is the only spectral changes noticed in the trifluoromethylated version **3′** (Figure 3.10a).

Most importantly, the characteristic broad band of the benzimidazolium ion (protonated

benzimidazole species) at ~3300 cm^{-1} is not present in the spectra, suggesting that the

oxidized species resulting from intermediate proton translocations (either by E1PT or

E2PT processes) are not present during the IR-SEC experiment. Therefore, these results,

together with the appearance of the set of bands from the protonated pyridine, imply that

a complete multiproton translocation takes place, leading to the formation of the E3PT

product in both the **3** and **3′** constructs.

3.4 Conclusions

Photoinduced PCET and long-range two-proton transport via a Grotthuss-type

mechanism were investigated in a biomimetic construct. The ultrafast, nonequilibrium

dynamics were assessed via 2DEV spectroscopy, in concert with electrochemical

techniques. A low frequency mode was identified experimentally and found to promote

double proton and electron transfer. Excitation frequency peak evolution and CLS

dynamics showed direct evidence of strongly coupled nuclear and electronic degrees of

freedom, from which it was concluded that the double proton and electron transfer

processes are concerted (up to an uncertainty of 24 fs). The nonequilibrium pathway from

the photoexcited Franck-Condon region to the E2PT state is characterized by a ~110 fs

timescale.

Additionally, electronic modulation of a benzimidazole-based bridge by

functionalization with trifluoromethyl EWGs proved to be an effective strategy for

increasing the redox potential of a MPCET process driving protons in a Grotthuss-type

proton wire and confirms the non-innocent nature of the partially conjugated scaffold that

is part of the hydrogen-bonded network between the initial proton donor (phenol) and the

TPA (pyridine). Substituting the trifluoromethyl groups on the benzimidazole-based bridge maintains the necessary balance between the hydrogen bond-accepting and donating capabilities of the benzimidazole, thus conserving its role as a reversible proton wire. These trifluoromethylated proton wires provide design principles for new generations of molecular proton wires capable of translocating multiple protons over significantly large distances with minimum thermodynamic cost to the coupled redox process.

3.5 References

(1)   Mitchell, P. Coupling of Phosphorylation to Electron and Hydrogen Transfer by a Chemi-Osmotic Type of Mechanism. *Nature* **1961**, *191* (4784), 144–148.

(2)   Migliore, A.; Polizzi, N. F.; Therien, M. J.; Beratan, D. N. Biochemistry and Theory of Proton-Coupled Electron Transfer. *Chem. Rev.* **2014**, *114* (7), 3381–3465.

(3)   Hammes-Schiffer, S.; Soudackov, A. V. Proton-Coupled Electron Transfer in Solution, Proteins, and Electrochemistry. *J. Phys. Chem. B* **2008**, *112* (45), 14108–14123.

(4)   Huynh, M. H. V.; Meyer, T. J. Proton-Coupled Electron Transfer. *Chem. Rev.* **2007**, *107* (11), 5004–5064.

(5)   Stubbe, J.; Nocera, D. G.; Yee, C. S.; Chang, M. C. Y. Radical Initiation in the Class I Ribonucleotide Reductase: Long-Range Proton-Coupled Electron Transfer? *Chem. Rev.* **2003**, *103* (6), 2167–2201.

(6)   Cukierman, S. Et Tu, Grotthuss! And Other Unfinished Stories. *Biochim. Biophys. Acta* **2006**, *1757* (8), 876–885.

(7)   Pavošević, F.; Culpitt, T.; Hammes-Schiffer, S. Multicomponent Quantum Chemistry: Integrating Electronic and Nuclear Quantum Effects via the Nuclear-Electronic Orbital Method. *Chem. Rev.* **2020**, *120* (9), 4222–4253.

(8)   Barry, B. A. Reaction Dynamics and Proton Coupled Electron Transfer: Studies of Tyrosine-Based Charge Transfer in Natural and Biomimetic Systems. *Biochim. Biophys. Acta* **2015**, *1847* (1), 46–54.

(9)   Meyer, T. J.; Huynh, M. H. V.; Thorp, H. H. The Possible Role of Proton-Coupled Electron Transfer (PCET) in Water Oxidation by Photosystem II. *Angew. Chem. Int. Ed.* **2007**, *46* (28), 5284–5304.

(10)   Reece, S. Y.; Nocera, D. G. Proton-Coupled Electron Transfer in Biology: Results from Synergistic Studies in Natural and Model Systems. *Annu. Rev. Biochem.* **2009**, *78*, 673–699.

(11)   Nagao, R.; Ueoka-Nakanishi, H.; Noguchi, T. D1-Asn-298 in Photosystem II Is Involved in a Hydrogen-Bond Network near the Redox-Active Tyrosine YZ for Proton Exit during Water Oxidation. *J. Biol. Chem.* **2017**, *292* (49), 20046–20057.

(12)   Kawashima, K.; Saito, K.; Ishikita, H. Mechanism of Radical Formation in the H-Bond Network of D1-Asn298 in Photosystem II. *Biochemistry* **2018**, *57* (33), 4997–5004.

(13)   Vinyard, D. J.; Brudvig, G. W. Progress Toward a Molecular Mechanism of Water Oxidation in Photosystem II. *Annu. Rev. Phys. Chem.* **2017**, *68*, 101–116.

(14)   Saito, K.; Rutherford, A. W.; Ishikita, H. Energetics of Proton Release on the First Oxidation Step in the Water-Oxidizing Enzyme. *Nat. Commun.* **2015**, *6*, 8488.

(15)   Long, S. P.; Marshall-Colon, A.; Zhu, X.-G. Meeting the Global Food Demand of the Future by Engineering Crop Photosynthesis and Yield Potential. *Cell* **2015**, *161* (1), 56–66.

(16)   Blankenship, R. E.; Tiede, D. M.; Barber, J.; Brudvig, G. W.; Fleming, G.; Ghirardi, M.; Gunner, M. R.; Junge, W.; Kramer, D. M.; Melis, A.; Moore, T. A.; Moser, C. C.; Nocera, D. G.; Nozik, A. J.; Ort, D. R.; Parson, W. W.; Prince, R. C.; Sayre, R. T. Comparing Photosynthetic and Photovoltaic Efficiencies and Recognizing the Potential for Improvement. *Science* **2011**, *332* (6031), 805–809.

(17)   Ort, D. R.; Merchant, S. S.; Alric, J.; Barkan, A.; Blankenship, R. E.; Bock, R.; Croce, R.; Hanson, M. R.; Hibberd, J. M.; Long, S. P.; Moore, T. A.; Moroney, J.; Niyogi, K. K.; Parry, M. A. J.; Peralta-Yahya, P. P.; Prince, R. C.; Redding, K. E.; Spalding, M. H.; Van Wijk, K. J.; Vermaas, W. F. J.; Von Caemmerer, S.; Weber, A. P. M.; Yeates, T. O.; Yuan, J. S.; Zhu, X. G. Redesigning Photosynthesis to Sustainably Meet Global Food and Bioenergy Demand. *Proc. Natl. Acad. Sci. U.S.A.* **2015**, *112* (28), 8529–8536.

(18)   Sayre, H. J.; Tian, L.; Son, M.; Hart, S. M.; Liu, X.; Arias-Rotondo, D. M.; Rand, B. P.; Schlau-Cohen, G. S.; Scholes, G. D. Solar Fuels and Feedstocks: The Quest for Renewable Black Gold. *Energy Environ. Sci.* **2021**, *14* (3), 1402–1419.

(19)   Sayre, H.; Ripberger, H. H.; Odella, E.; Zieleniewska, A.; Heredia, D. A.; Rumbles, G.; Scholes, G. D.; Moore, T. A.; Moore, A. L.; Knowles, R. R. PCET-Based Ligand Limits Charge Recombination with an Ir(III) Photoredox Catalyst. *J. Am. Chem. Soc.* **2021**, *143* (33), 13034–13043.

(20)   Wu, X.; Hong, J. J.; Shin, W.; Ma, L.; Liu, T.; Bi, X.; Yuan, Y.; Qi, Y.; Surta, T. W.; Huang, W.; Neuefeind, J.; Wu, T.; Greaney, P. A.; Lu, J.; Ji, X. Diffusion-Free Grotthuss Topochemistry for High-Rate and Long-Life Proton Batteries. *Nat. Energy* **2019**, *4* (2), 123–130.

(21)   Arsenault, E. A.; Bhattacharyya, P.; Yoneda, Y.; Fleming, G. R. Two-Dimensional Electronic-Vibrational Spectroscopy: Exploring the Interplay of Electrons and Nuclei in Excited State Molecular Dynamics. *J. Chem. Phys.* **2021**, *155* (2), 020901.

(22)   Oliver, T. A. A.; Lewis, N. H. C.; Fleming, G. R. Correlating the Motion of Electrons and Nuclei with Two-Dimensional Electronic-Vibrational Spectroscopy. *Proc. Natl. Acad. Sci. U.S.A.* **2014**, *111* (28), 10061–10066.

(23)   Yoneda, Y.; Mora, S. J.; Shee, J.; Wadsworth, B. L.; Arsenault, E. A.; Hait, D.; Kodis, G.; Gust, D.; Moore, G. F.; Moore, A. L.; Head-Gordon, M.; Moore, T. A.; Fleming, G. R. Electron-Nuclear Dynamics Accompanying Proton-Coupled Electron Transfer. *J. Am. Chem. Soc.* **2021**, *143* (8), 3104–3112.

(24)   Goings, J. J.; Hammes-Schiffer, S. Nonequilibrium Dynamics of Proton-Coupled Electron Transfer in Proton Wires: Concerted but Asynchronous Mechanisms. *ACS Cent. Sci.* **2020**, *6* (9), 1594–1601.

(25)   Cook, D. Vibrational Spectra Of Pyridinium Salts. *Can. J. Chem.* **1961**, *39* (10), 2009–2024.

(26)   Glazunov, V. P.; Odinokov, S. E. Infrared Spectra of Pyridinium Salts in Solution - I. The Region of Middle Frequencies. *Spectrochim. Acta A* **1982**, *38* (4), 399–408.

(27)   Moore, G. F.; Hambourger, M.; Gervaldo, M.; Poluektov, O. G.; Rajh, T.; Gust, D.; Moore, T. A.; Moore, A. L. A Bioinspired Construct That Mimics the Proton Coupled Electron Transfer between P680$^{•+}$ and the Tyr$_z$-His190 Pair of Photosystem II. *J. Am. Chem. Soc.* **2008**, *130* (32), 10466–10467.

(28)   Guerra, W. D.; Odella, E.; Secor, M.; Goings, J. J.; Urrutia, M. N.; Wadsworth, B. L.; Gervaldo, M.; Sereno, L. E.; Moore, T. A.; Moore, G. F.; Hammes-Schiffer, S.; Moore, A. L. Role of Intact Hydrogen-Bond Networks in Multiproton-Coupled Electron Transfer. *J. Am. Chem. Soc.* **2020**, *142* (52), 21842–21851.

(29)   Cho, M.; Fleming, G. R. Two-Dimensional Electronic-Vibrational Spectroscopy Reveals Cross-Correlation between Solvation Dynamics and Vibrational Spectral Diffusion. *J. Phys. Chem. B* **2020**, *124* (49), 11222–11235.

(30)   Arsenault, E. A.; Yoneda, Y.; Iwai, M.; Niyogi, K. K.; Fleming, G. R. Vibronic Mixing Enables Ultrafast Energy Flow in Light-Harvesting Complex II. *Nat. Commun.* **2020**, *11*, 1460.

(31)   Wu, E. C.; Ge, Q.; Arsenault, E. A.; Lewis, N. H. C.; Gruenke, N. L.; Head-Gordon, M. J.; Fleming, G. R. Two-Dimensional Electronic-Vibrational Spectroscopic Study of Conical Intersection Dynamics: An Experimental and Electronic Structure Study. *Phys. Chem. Chem. Phys.* **2019**, *21* (26), 14153–14163.

(32)   Roy, P. P.; Shee, J.; Arsenault, E. A.; Yoneda, Y.; Feuling, K.; Head-Gordon, M.; Fleming, G. R. Solvent Mediated Excited State Proton Transfer in Indigo Carmine. *J. Phys. Chem. Lett.* **2020**, *11* (10), 4156–4162.

(33)   Arsenault, E. A.; Yoneda, Y.; Iwai, M.; Niyogi, K. K.; Fleming, G. R. The Role of Mixed Vibronic Q_y-Q_x States in Green Light Absorption of Light-Harvesting Complex II. *Nat. Commun.* **2020**, *11*, 6011.

(34)   Odella, E.; Mora, S. J.; Wadsworth, B. L.; Huynh, M. T.; Goings, J. J.; Liddell, P. A.; Groy, T. L.; Gervaldo, M.; Sereno, L. E.; Gust, D.; Moore, T. A.; Moore, G. F.; Hammes-Schiffer, S.; Moore, A. L. Controlling Proton-Coupled Electron Transfer in Bioinspired Artificial Photosynthetic Relays. *J. Am. Chem. Soc.* **2018**, *140* (45), 15450–15460.

(35)   Odella, E.; Wadsworth, B. L.; Mora, S. J.; Goings, J. J.; Huynh, M. T.; Gust, D.; Moore, T. A.; Moore, G. F.; Hammes-Schiffer, S.; Moore, A. L. Proton-Coupled Electron Transfer Drives Long-Range Proton Translocation in Bioinspired Systems. *J. Am. Chem. Soc.* **2019**, *141* (36), 14057–14061.

(36)   Mora, S. J.; Heredia, D. A.; Odella, E.; Vrudhula, U.; Gust, D.; Moore, T. A.; Moore, A. L. Design and Synthesis of Benzimidazole Phenol-Porphyrin Dyads for the Study of Bioinspired Photoinduced Protoncoupled Electron Transfer. *J. Porphyr. Phthalocyanines* **2019**, *23* (11n12), 1336–1345.

(37)   Odella, E.; Mora, S. J.; Wadsworth, B. L.; Goings, J. J.; Gervaldo, M. A.; Sereno, L. E.; Groy, T. L.; Gust, D.; Moore, T. A.; Moore, G. F.; Hammes-Schiffer, S.; Moore, A. L. Proton-Coupled Electron Transfer across Benzimidazole Bridges in Bioinspired Proton Wires. *Chem. Sci.* **2020**, *11* (15), 3820–3828.

(38)   Mora, S. J.; Odella, E.; Moore, G. F.; Gust, D.; Moore, T. A.; Moore, A. L.
         Proton-Coupled Electron Transfer in Artificial Photosynthetic Systems. *Acc.
         Chem. Res.* **2018**, *51* (2), 445–453.

(39)   Huynh, M. T.; Mora, S. J.; Villalba, M.; Tejeda-Ferrari, M. E.; Liddell, P. A.;
         Cherry, B. R.; Teillout, A.-L.; Machan, C. W.; Kubiak, C. P.; Gust, D.; Moore, T.
         A.; Hammes-Schiffer, S.; Moore, A. L. Concerted One-Electron Two-Proton
         Transfer Processes in Models Inspired by the Tyr-His Couple of Photosystem II.
         ACS Cent. Sci. **2017**, *3* (5), 372–380.

(40)   Odella, E.; Secor, M.; Elliott, M.; Groy, T. L.; Moore, T. A.; Hammes-Schiffer,
         S.; Moore, A. L. Multi PCET in Symmetrically Substituted Benzimidazoles.
         Chem. Sci. **2021**, *12* (38), 12667–12675.

(41)   Hoganson, C. W.; Babcock, G. T. A Metalloradical Mechanism for the
         Generation of Oxygen from Water in Photosynthesis. *Science* **1997**, *277* (5334),
         1953–1956.

(42)   Faller, P.; Goussias, C.; Rutherford, A. W.; Un, S. Resolving Intermediates in
         Biological Proton-Coupled Electron Transfer: A Tyrosyl Radical Prior to Proton
         Movement. *Proc. Natl. Acad. Sci. U.S.A.* **2003**, *100* (15), 8732–8735.

(43)   Markle, T. F.; Rhile, I. J.; DiPasquale, A. G.; Mayer, J. M. Probing Concerted
         Proton-Electron Transfer in Phenol-Imidazoles. *Proc. Natl. Acad. Sci. U.S.A.*
         2008, *105* (24), 8185–8190.

(44)   Glazunov, V. P.; Odinokov, S. E. Infrared Spectra of Pyridinium Salts in Solution
         - II. Fermi Resonance and Structure of ν_{NH} Bands. *Spectrochim. Acta A* **1982**, *38*
         (4), 409–415.

(45)   Odella, E.; Moore, T. A.; Moore, A. L. Tuning the Redox Potential of Tyrosine-
         Histidine Bioinspired Assemblies. *Photosynth. Res.* **2022**, *151*, 185–193.

(46)   Connelly, N. G.; Geiger, W. E. Chemical Redox Agents for Organometallic
         Chemistry. *Chem. Rev.* **1996**, *96* (2), 877–910.

(47)   Corrsin, L.; Fax, B. J.; Lord, R. C. The Vibrational Spectra of Pyridine and
         Pyridine-d$_5$. *J. Chem. Phys.* **1953**, *21* (7), 1170–1176.

(48)   Wong, K. N.; Colson, S. D. The FT-IR Spectra of Pyridine and Pyridine-d$_5$. *J.
         Mol. Spectrosc.* **1984**, *104* (1), 129–151.

(49)   Partal Ureña, F.; Fernández Gómez, M.; López González, J. J.; Martínez Torres,
         E. A New Insight into the Vibrational Analysis of Pyridine. *Spectrochim. Acta A*
         2003, *59* (12), 2815–2839.

CHAPTER 4

EXPERIMENTAL PROCEDURES

4.1 General Experimental Methods

Mass spectra. Mass spectra of all compounds were obtained with Voyager DE STR MALDI-TOF-MS in positive ion using *trans,trans*-1,4-diphenyl-1,3-butadiene as a matrix.

Nuclear Magnetic Resonance. ^{1}H-NMR spectra were recorded on a Varian MR400 spectrometer operating at 400 MHz in deuterated chloroform ($CDCl_3$) at room temperature. Chemical shifts (δ) are reported in parts per million (ppm) relative to residual trimethylsilane peak.

4.2 Experimental Procedures for Chapter 2

Materials. All compounds were synthesized from commercially available starting materials. All reagents were purchased from commercial suppliers and used as received without further purification. Solvents were obtained from Fisher (CH_2Cl_2, hexanes, toluene, and methanol) or Aldrich (C_3H_7CN, DMF, and C_6H_5CN), and were distilled before use.

Electrochemistry. All voltammetry measurements were performed with a Biologic SP-300 potentiostat using a glassy carbon (3 mm diameter) WE, a platinum counter electrode (CE), and a silver wire pseudoreference electrode (RE) in a conventional three-electrode cell at 250 mV s^{-1} scan rate at room temperature under argon. The potential of the silver wire RE was determined using the ferrocenium/ferrocene redox couple as an internal standard and adjusting to V vs SCE in voltammograms collected prior adding ferrocene.[1] C_6H_5CN, C_3H_7CN, CH_2Cl_2, or DMF were used as solvents. Electrochemical analysis grade $TBAPF_6$ electrolyte was obtained from Aldrich and stored in a desiccator containing calcium sulfate ($CaSO_4$) as a desiccant. The supporting electrolyte

concentration of all electrochemical measurements was 0.1 M TBAPF$_6$, and the WE was cleaned between experiments by polishing with alumina (50 nm diameter) slurry, followed by solvent rinses.

UV-Vis-NIR and UV-Vis-NIR-SEC. All ultraviolet-visible-near-infrared (UV-Vis-NIR) spectra were recorded on a Shimadzu SolidSpec-3700 spectrometer with a deuterium (D$_2$) lamp for the ultraviolet range and a WI (halogen) lamp for the visible and near-infrared, using C$_6$H$_5$CN, C$_3$H$_7$CN, CH$_2$Cl$_2$, or DMF as solvents. UV-Vis-NIR-SEC measurements were recorded using a Biologic SP-200 potentiostat, a Pt "*honeycomb*" design WE with a Pt CE (Pine Research), and a silver wire RE. In all experiments, the supporting electrolyte contained 0.1 M TBAPF$_6$ and was sparged with argon. Thin layer constant potential electrolysis was monitored via UV-Vis-NIR as the WE was polarized in a stepwise manner (*i.e.*, an incrementally increasing bias potential versus the silver wire reference). Before changing the electrode polarization, absorption spectra were continuously collected at each applied potential until there were no significant changes in the resulting absorption spectra. This procedure was repeated until increasing the polarization no longer resulted in significant changes between UV-Vis-NIR spectra collected prior to and following the potential step. The Pt honeycomb WE was cleaned between experiments by collecting cyclic voltammograms in 0.1 M H$_2$SO$_4$, followed by rinsing with 18.2 MΩ cm water and then acetone. The potential of the RE was determined by measuring the ferrocenium/ferrocene redox couple under identical solvent conditions before and after completion of the measurements.

FTIR and IR-SEC. FTIR spectra were recorded on a Bruker Vertex 70, in pressed KBr

pellets using a transmission mode at 64 scans with a 1 cm^{-1} resolution, GloBar MIR source, a broadband KBr beamsplitter, and a liquid nitrogen cooled MCT detector. Background measurements were obtained from the air, and baselines were corrected for rubberband scattering. The data were processed using OPUS software. IR-SEC measurements were performed using a Biologic potentiostat connected to a custom optically transparent thin-layer electrochemical cell (path length: 0.2 mm) equipped with NaCl optical windows and purchased from Professor Frantisek Hartl, University of Reading. The cell contained a Pt mesh CE, a silver wire RE, and a Pt mesh WE. In all experiments the supporting electrolyte contained 0.1 M TBAPF$_6$ and was sparged with argon. The Pt mesh WE was positioned within the light path of the IR spectrophotometer. The cell and its contents were sealed under an argon atmosphere prior to all measurements, and thin layer constant potential electrolysis was monitored via FTIR as the WE was polarized in a stepwise manner (*i.e.*, an incrementally increasing bias potential versus the silver wire reference). Before changing the electrode polarization, absorption spectra were continuously collected at each applied potential until there were no significant changes in the resulting absorption spectra. This procedure was repeated until increasing the polarization no longer resulted in significant changes between FTIR spectra collected prior to and following the potential step. The cell was disassembled and cleaned between experiments by rinsing the cell components first with water, followed by acetone, and finally CH$_2$Cl$_2$. A drop of nitric acid was placed on the Pt mesh WE for approximately 5−10 min before rinsing with water.

XPS. Photoelectron Spectroscopy was performed using a monochromatized Al Ka source (hv = 1486.6 eV), operated at 63 W, on a VG ESCALAB 220i-XL (Thermo Fisher)

system at a takeoff angle of 0° relative to the surface normal and a pass energy for narrow scan spectra of 20 eV at an instrument resolution of ~700 meV. Survey spectra were collected with a pass energy of 150 eV. Spectral analysis was performed using Casa XPS analysis software, and all spectra were calibrated by adjusting C 1s core level position to 284.8 eV.

X-ray Absorption Near Edge Structure. XANES analyses were conducted at the SAMBA beamline,[2] Synchrotron SOLEIL, France. The electron storage ring was operated at 2.75 GeV. A Si(220) double crystal monochromator was used, which was calibrated by assigning the first inflection of a Fe foil XANES spectrum to 7111.2 eV. The XANES spectra were collected in transmission mode using an N_2-filled ionization chamber. Spectra were collected from 6900 to 8000 eV using a continuous scan acquisition mode, with a 5 eV s^{-1} velocity and 0.04 s $point^{-1}$ integration time. Each scan was obtained in 220 seconds and featured 5500 data points with a 0.2 eV step size. Multiple spectra were repeatedly collected for each sample until their average spectrum had a satisfying signal-to-noise ratio. All XAS data processing was done using the Athena program of the Demeter software suite.[3]

Synthesis

*5,10,15,20-tetra-p-tolylporphyrin (**TTP**), **FeTTPCl**, and meso-β doubly-fused 5,24-di-(p-tolyl)-10,19,29,38-tetramesitylporphyrin (free-base fused-porphyrin, **FP**)*. These compounds were synthesized following previously reported methods.[4,5] The identity and purity of the compound was confirmed via MALDI-TOF MS, Ultraviolet-visible (UV-Vis) spectroscopy, and homogenous electrochemical analysis.

Fe₂FPCl₂. This compound was synthesized by adding $FeCl_2 \cdot 4H_2O$ (187.8 mg, 945.3 μmol) in approximately three equivalent portions over 30 min to refluxing solution of **FP** (20 mg, 15.7 μmol) in a 5:1 solution of CH_2Cl_2:methanol. The mixture was refluxed overnight under an argon atmosphere before removing the solvent under reduced pressure. The crude product was purified via column chromatography using alumina as the stationary phase and 50:50:3 CH_2Cl_2:hexane:methanol as the mobile phase. The resulting dark purple fractions were concentrated under reduced pressure before redissolving in CH_2Cl_2 and washing with an aqueous 6 M HCl solution using a separatory funnel. Collection of the resulting organic phase and removal of the solvent under reduced pressure gave the target compound in near quantitative yield. UV-Vis (CH_2Cl_2) 375 nm, 411 nm, 500 nm, 533 nm, 678 nm, 738 nm, 785 nm, 894 nm. FTIR (KBr) 1500 cm^{-1}, 1463 cm^{-1}, 1384 cm^{-1}, 1321 cm^{-1}, 1263 cm^{-1}, 1208 cm^{-1}, 1182 cm^{-1}, 1162 cm^{-1}, 1129 cm^{-1}, 1109 cm^{-1}, 1065 cm^{-1}, 1001 cm^{-1}. MALDI-TOF MS: calcd. for $C_{90}H_{72}Cl_2Fe_2N_8$ 1446.396 m/z, obsd. 1446.700 m/z.
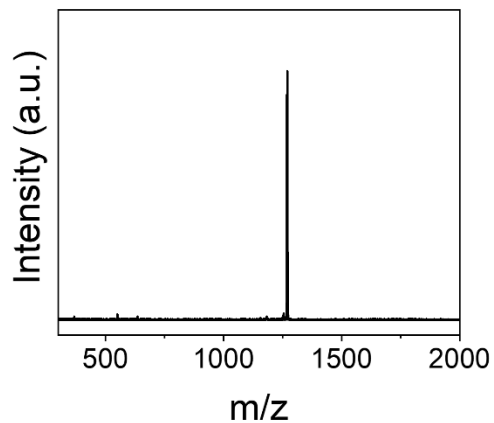
Figure 4.1 MALDI-TOF MS data collected using **FP**.
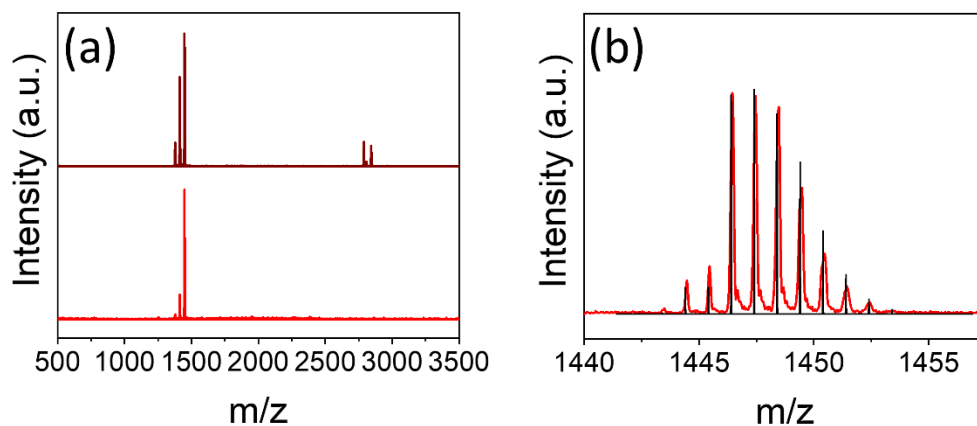
Figure 4.2 (a) MALDI-TOF MS data collected using **Fe₂FPCl₂** (red/bottom) and the

crude product obtained before washing with an aqueous 6 M HCl solution (brown/top).

(b) MALDI-TOF MS data collected using **Fe₂FPCl₂** (red) overlaid with the calculated

isotopic distribution of $C_{90}H_{72}N_8Fe_2Cl_2$ (black).
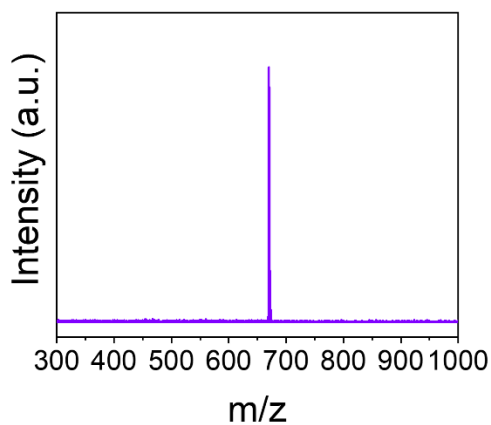
Figure 4.3 MALDI-TOF MS data collected using **TTP**.
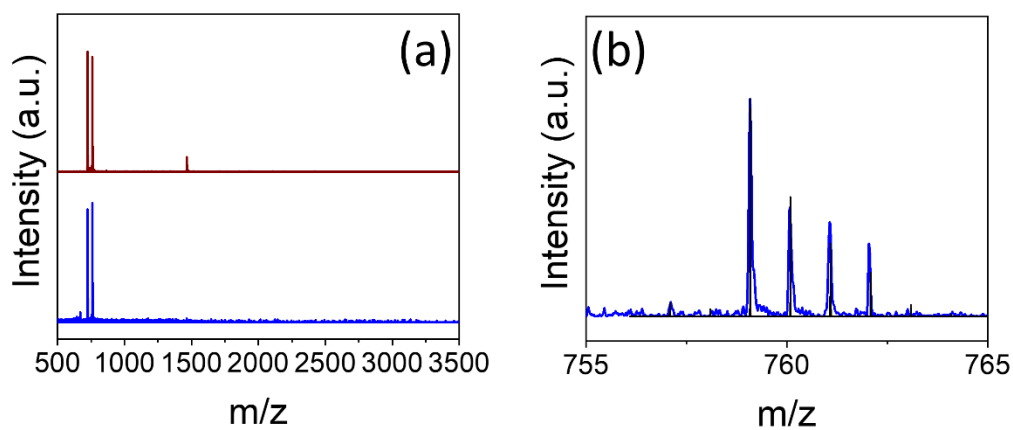
Figure 4.4 (a) MALDI-TOF MS data collected using **FeTTPCl** (blue/bottom) and the

crude product obtained before washing with an aqueous 6 M HCl solution (brown/top). b)

MALDI-TOF MS data collected using **FeTTPCl** (blue) overlaid with the calculated

isotopic distribution of $C_{48}H_{36}N_4FeCl$ (black).
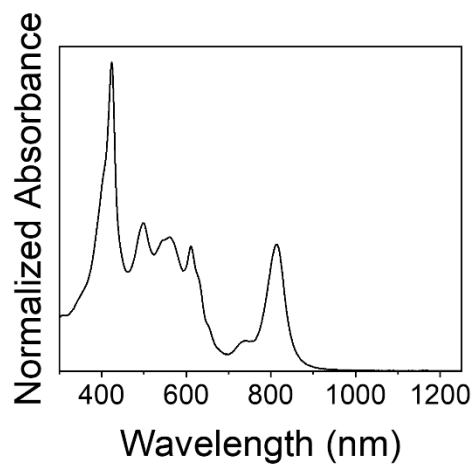
Figure 4.5 Normalized absorption spectrum of **FP** recorded in CH_2Cl_2.
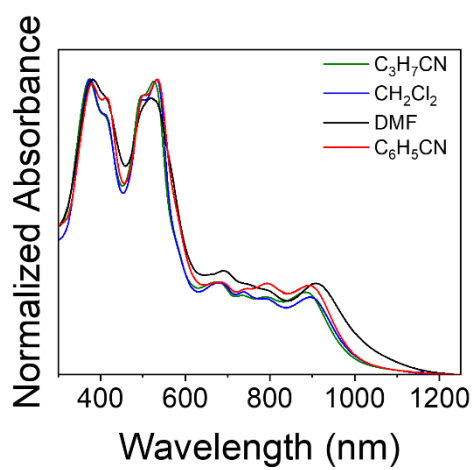
Figure 4.6 Normalized absorption spectra of **Fe₂FPCl₂** recorded in C_3H_7CN (green),

CH_2Cl_2 (blue), DMF (black), or C_6H_5CN (red).
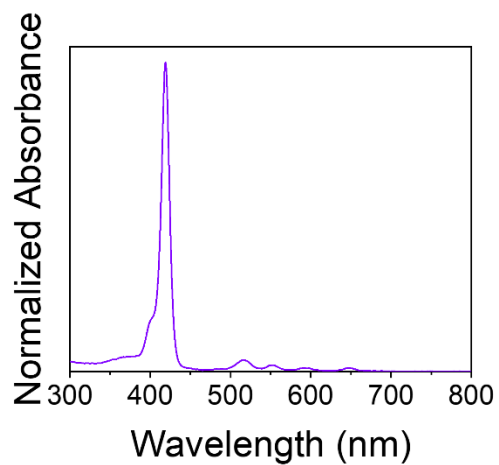
Figure 4.7 Normalized absorption spectrum of **TTP** recorded in CH_2Cl_2.
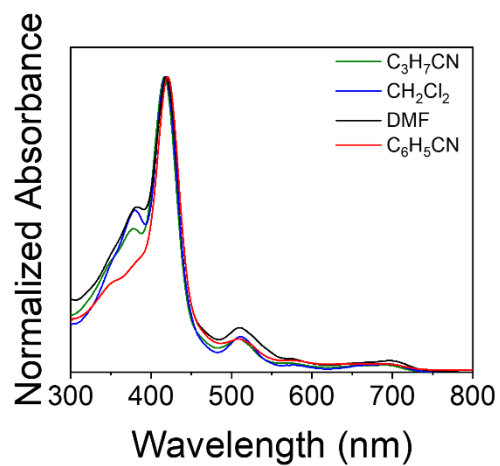
Figure 4.8 Normalized absorption spectra of **FeTTPCl** recorded in C_3H_7CN (green),

CH_2Cl_2 (blue), DMF (black), or C_6H_5CN (red).

Table 4.1 Wavelengths of Soret-like and Q-like absorption bands of **Fe₂FPCl₂** in different solvents.

	Soret-absorption band(s) (nm)	Q-absorption band(s) (nm)
C_3H_7CN	373, 409,[a] 496, 524	670, 737, 794, 879
CH_2Cl_2	375, 411,[a] 500, 533	678, 738, 785, 894
DMF	380, 513	901
C_6H_5CN	380, 413, 502, 534	683, 746, 793, 892

[a] This absorption feature appears as a shoulder.

Table 4.2 Wavelengths of Soret-like and Q-like absorption bands of **FeTTPCl** in different solvents.

	Soret-absorption band(s) (nm)	Q-absorption band(s) (nm)
C_3H_7CN	378, 417	509, 571, 658,[a] 688
CH_2Cl_2	381, 418	511, 574.5, 663,[a] 692
DMF	322, 410	570, 612
C_6H_5CN	351,[a] 421	509, 572, 641, 684

[a] This absorption feature appears as a shoulder.
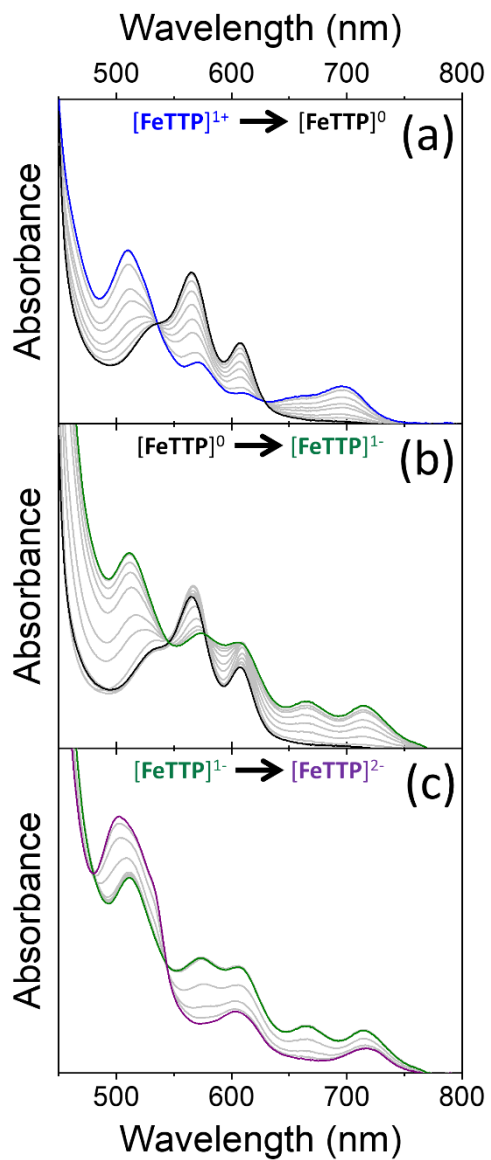
Figure 4.9 UV-Vis-NIR absorption spectra of (a-c) **FeTTPCl** (0.25 mM) recorded in a

0.1 M TBAPF$_6$ DMF solution polarized at potentials to generate **[FeTTP]**$^{1+}$ (blue),

[FeTTP]^0 (black), and **[FeTTP]**$^{1-}$ (green), and **[FeTTP]**$^{2-}$ (purple).
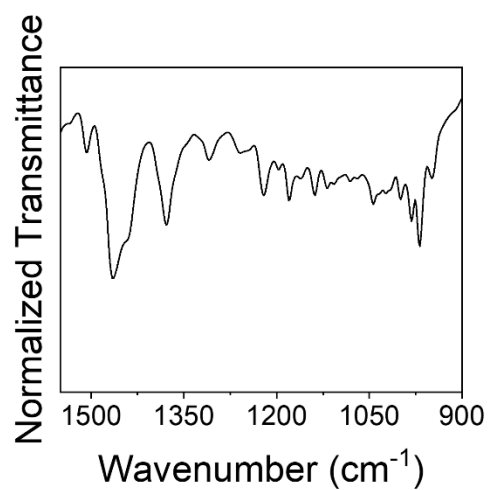
Figure 4.10 Normalized FTIR transmission spectrum of **FP** recorded in a KBr pellet.
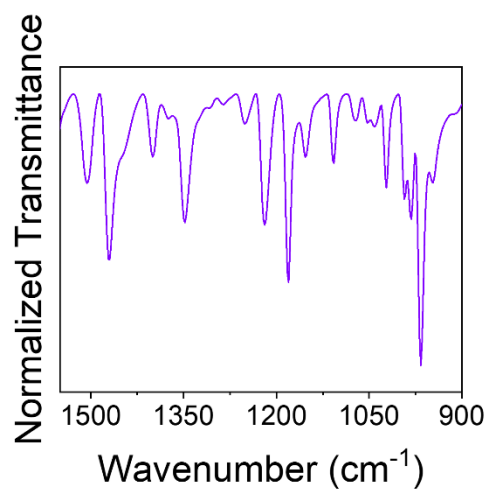
Figure 4.11 Normalized FTIR transmission spectrum of **TTP** recorded in a KBr pellet.
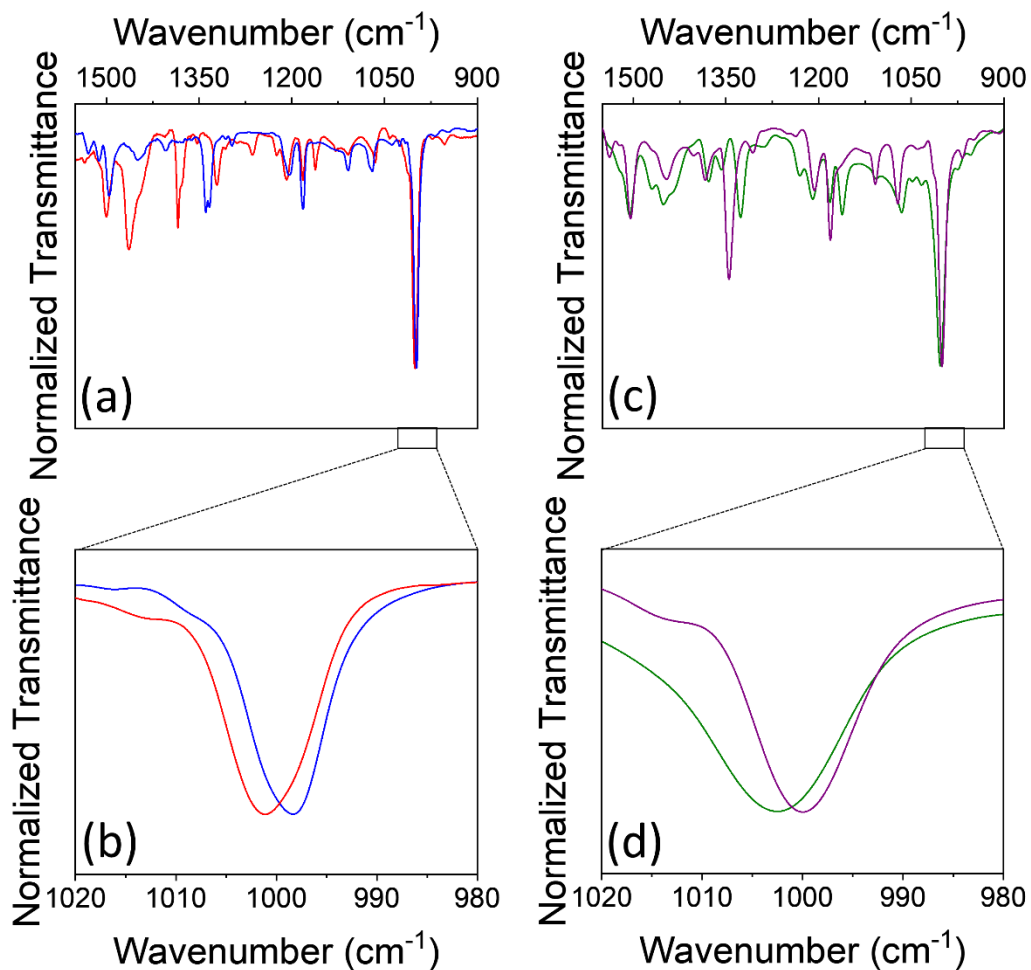
Figure 4.12 (a) Normalized FTIR transmission spectra of **Fe₂FPCl₂** (red) and **FeTTPCl** (blue), with an (b) expanded plot of the 980–1020 cm^{-1} region. Data recorded with a 1 cm^{-1} resolution. (c) Normalized FTIR transmission spectra of Cu₂FP (green) and CuTTP (purple), with an (d) expanded plot of the 980–1020 cm^{-1} region. Data recorded with a 2 cm^{-1} resolution.

106
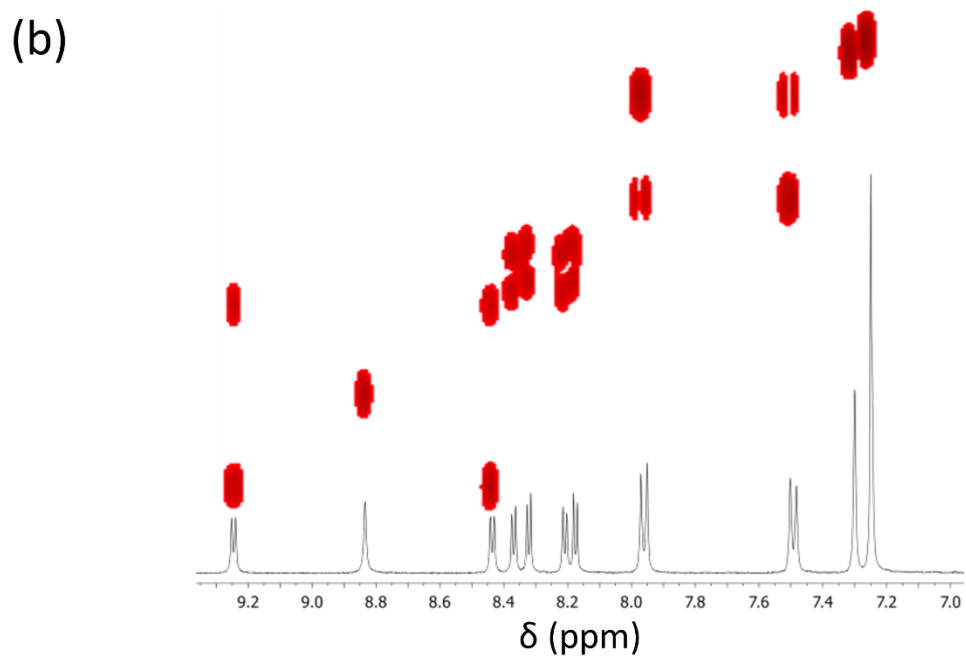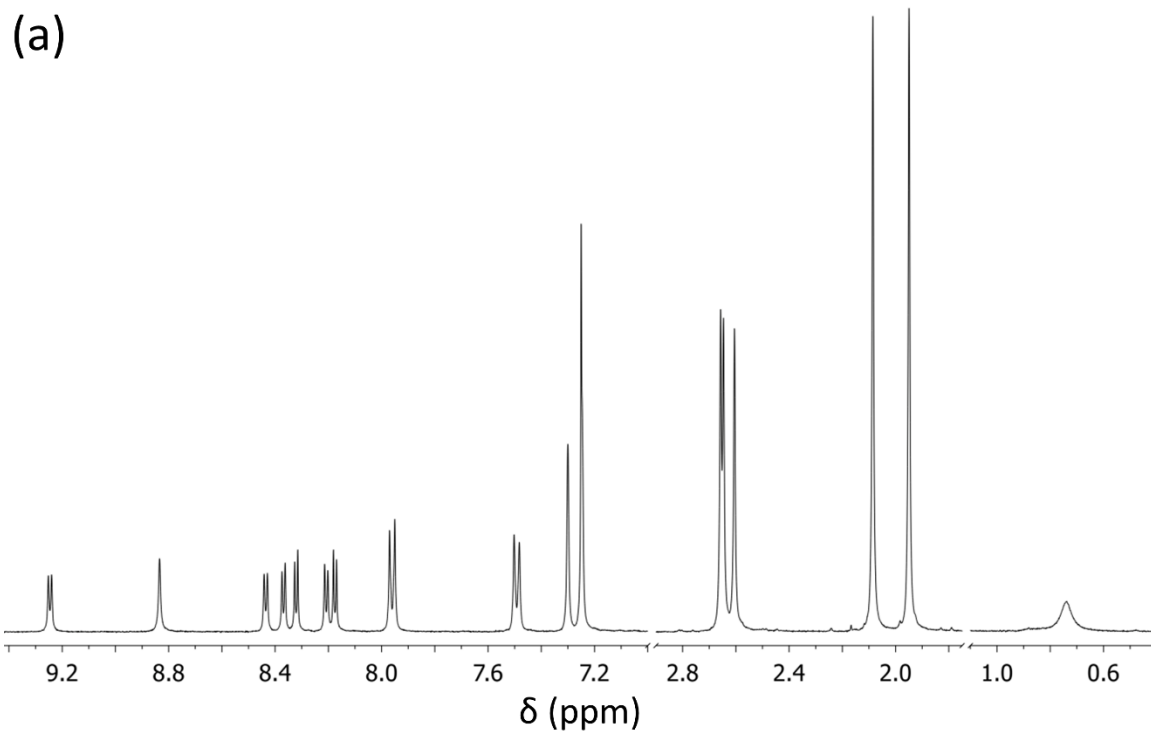
Figure 4.13 (a) ^{1}H NMR spectrum (black) and (b) ^{1}H NMR spectrum (black) of the aromatic region with overlaid COSY data (red) of **FP** in CDCl$_3$.
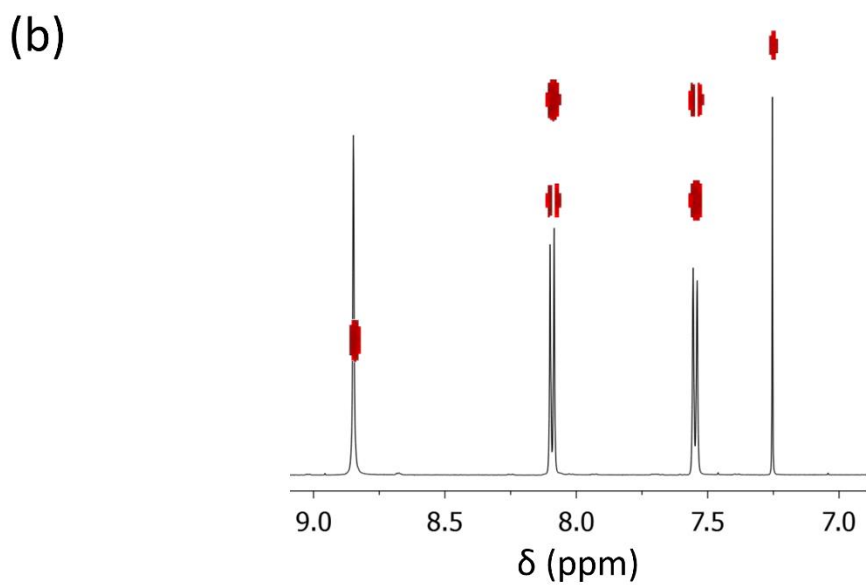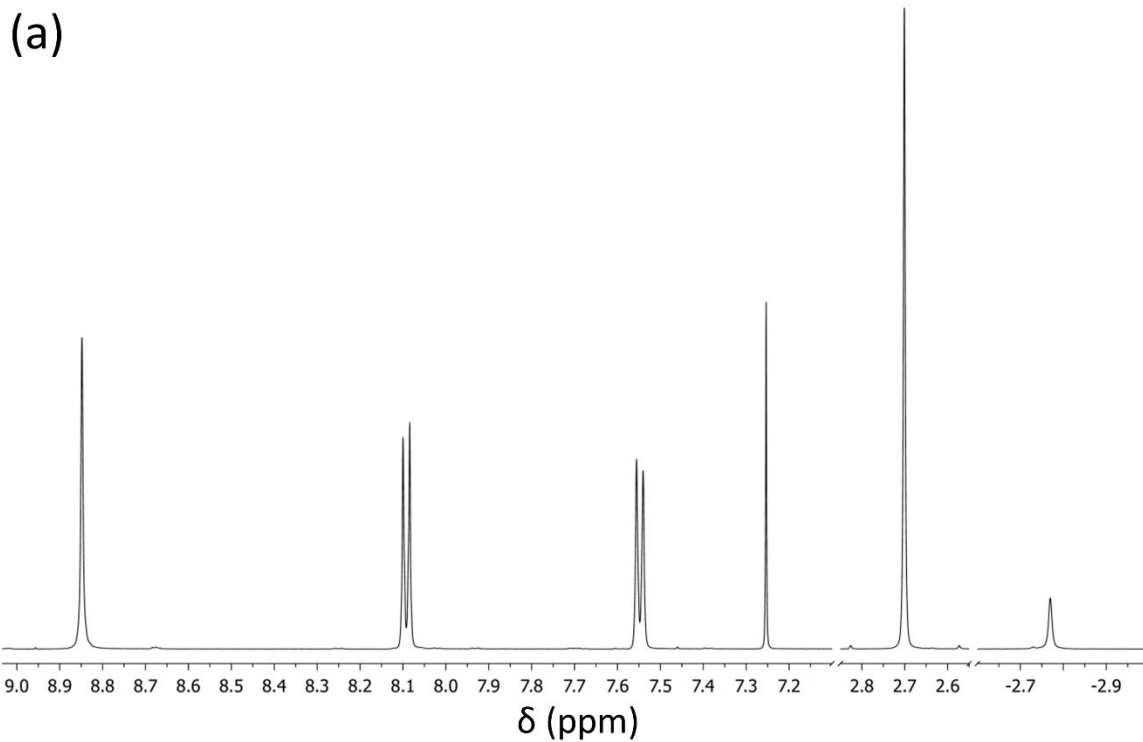
Figure 4.14 (a) ^{1}H NMR spectrum (black) and (b) ^{1}H NMR spectrum (black) of the aromatic region with overlaid COSY data (red) of **TTP** in CDCl$_3$.
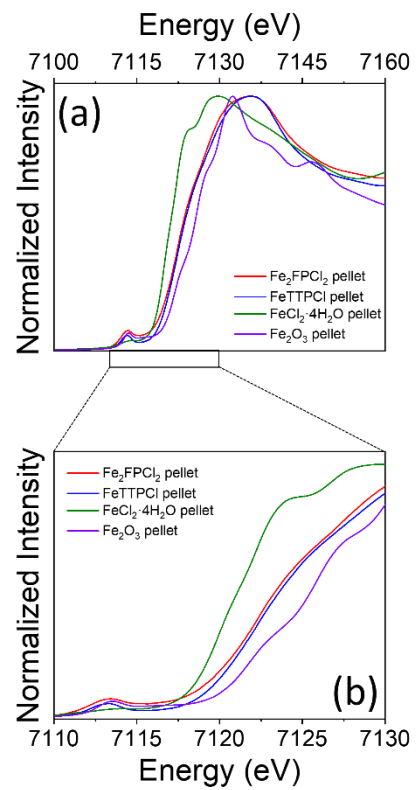
Figure 4.15 (a) XANES spectra recorded at the Fe K-edge of **Fe₂FPCl₂** (red), **FeTTPCl** (blue), FeCl₂·4H₂O (green), or Fe₂O₃ (purple) pellets. (b) Expanded plot of the 7110–7130 eV region.

Table 4.3 Cathodic peak potentials of **Fe₂FPCl₂** and **FeTTPCl** as determined by differential pulse voltammetry. An assignment of the related redox couple is indicated in parenthesis. All voltammograms were collected under argon and at room temperature using a 3 mm diameter glassy carbon WE immersed in solutions containing 1 mM porphyrin and 0.1 M TBAPF$_6$ in DMF. In all of these experiments, the ferrocenium/ferrocene cathodic peak potential was used as an internal reference.

	^nE (V vs Fc$^+$/Fc)					
	^{VI}E	^{V}E	^{IV}E	^{III}E	^{II}E	^{I}E
	-2.38	-2.11	-1.45	-1.20	-0.71	-0.60
Fe₂FPCl₂	[Fe₂FP]$^{3-}$ /[Fe₂FP]$^{4-}$	[Fe₂FP]$^{2-}$ /[Fe₂FP]$^{3-}$	[Fe₂FP]$^{1-}$ /[Fe₂FP]$^{2-}$	[Fe₂FP]^{0}/ [Fe₂FP]$^{1-}$	[Fe₂FP]$^{1+}$/ [Fe₂FP]^{0}	[Fe₂FP]$^{2+}$/ [Fe₂FP]$^{1+}$
FeTTPCl	-	-	-	-2.20 [FeTTP]$^{1-}$ /[FeTTP]$^{2-}$	-1.54 [FeTTP]^{0}/ [FeTTP]$^{1-}$	-0.70 [FeTTP]$^{1+}$ /[FeTTP]^{0}

4.3 Experimental Procedures for Chapter 3

Materials. CH₂Cl₂ was distilled from calcium hydride (CaH₂) prior to use and stored over molecular sieves (3 Å or 4 Å).

Electrochemistry. The cyclic voltammetry measurements were performed with a CH Instruments 760C potentiostat using a glassy carbon (3 mm diameter) WE, a platinum wire CE, and a silver wire RE in a conventional three-electrode cell. Anhydrous CH₂Cl₂ stored over molecular sieves and K₂CO₃ or deuterated acetonitrile were used as solvent in

the electrochemical measurements. The concentration of the compound of interest was 1

mM, containing 0.1 M (for CH_2Cl_2) or 0.5 M (for acetonitrile) $TBAPF_6$ as the supporting

electrolyte. The WE was cleaned between experiments by polishing it with a 0.05 μm

alumina slurry on a microcloth polishing pad, followed by solvent rinses and drying

under a stream of nitrogen. All measurements were conducted at room temperature, and

the solution was deoxygenated by bubbling with argon. The potential of the RE was

determined using the ferrocenium/ferrocene redox couple as an internal standard and

adjusting to the SCE scale (with $E_{1/2}$ taken to be 0.46 V vs SCE in CH_2Cl_2 and 0.40 V vs

SCE in acetonitrile) in voltammograms collected prior adding ferrocene.[1]

IR-SEC. The IR-SEC measurements were conducted using a Biologic SP-200 potentiostat

connected to an optically transparent thin-layer electrochemical cell

(Spectroelectrochemistry Reading RT OTTLE cell), pathlength 0.2 mm, equipped with

CaF_2 optical windows. The electrodes arranged in the cell are Pt mesh CE, Ag wire

pseudo RE, and Pt mesh WE. The WE was positioned in the light path of the IR

spectrophotometer (Bruker Vertex 70 spectrometer, GloBar MIR source, broadband KBr

beamsplitter, and liquid nitrogen cooled MCT detector). For all the IR-SEC

measurements, 0.1 M $TBAPF_6$ was used as the supporting electrolyte in deuterated

acetonitrile or CH_2Cl_2. Thin-layer constant potential electrolysis was monitored via FTIR

as the WE was polarized in 100 mV increments *vs* the Ag wire RE. Absorption spectra

(64 scans, 2 cm^{-1} resolution) were continuously collected at each applied potential until

there were no further significant changes.

2DEV. A detailed description for the two-dimensional electronic-vibrational (2DEV)

spectroscopic setup can be found elsewhere.[6] Briefly, the output of a Ti:sapphire

oscillator (Vitara-S, Coherent) was regeneratively amplified with a 1 kHz repetition rate (Legend Elite, Coherent), an energy of 1 mJ/pulse, and a pulse duration of 40 fs. The amplified pulse was divided into two and one was used to pump a home-built visible non-collinear optical parametric amplifier (NOPA). The other pulse was used to generate a mid-IR probe pulse (centered at 6.2 μm) by difference frequency generation with signal and idler pulses from a near-IR collinear OPA. The output of the NOPA (centered at 580 nm, 60 nm fwhm) was compressed to 10 fs at the sample position using a pair of prisms and an acousto-optic dispersive programmable filter (AODPF, Dazzler, Fastlite). The pulse pair was introduced to a retroreflector on a motorized translation stage to control the waiting time, t, between the pump and probe pulses. The total power of the pump pulses was 200 nJ and the pulses were focused into the sample with spot size of 250 μm. The mid-IR pulse was divided by a 50:50 beam splitter to form probe and reference beams. The probe and reference beams were dispersed by a spectrometer (Horiba, Triax 180) and detected by a 64-pixel HgCdTe dual array (Infrared Systems Development). The cross-correlation between visible and mid-IR pulses was estimated to be 90 fs by a step-like transient IR response of a 50 μm Ge plate and by a solvent only measurement. For each waiting time, a 2DEV spectrum was acquired by using the AODPF to scan the t_1 delay over 0-100 fs with 2.5 fs steps. For each t_1 delay, the signal was acquired with the relative phase between the pump pulses φ_{12} set by 0, $2\pi/3$ and $4\pi/3$, and the desired signal was isolated by a 3×1 phase cycling scheme.[7,8] The excitation axis was obtained by a Fourier transformation over t_1. The signal was collected in the fully rotated frame with respect to t_1. The CLS was calculated by linear fitting of the conditional averages along visible axis[9] as the CLS (Figure 3.4b and Figure 4.17) along the IR axis reflects the same

information.[10] Excitation frequency peak evolution (Figure 3.4a, Figure 4.18, Figure 4.19, and Figure 4.20) was calculated by fitting the 2DEV spectrum along visible excitation axis at a particular IR probe frequency at each waiting time with a Gaussian function.
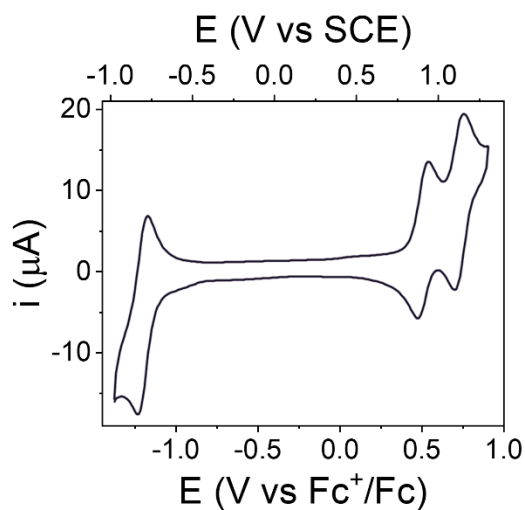
Figure 4.16 Cyclic voltammetry of **PF₁₅-BIP-Pyr**. The midpoint potentials ($E_{1/2}$) for the **PF₁₅-BIP-Pyr⁺/PF₁₅-BIP-Pyr** and **PF₁₅-BIP-Pyr/PF₁₅-BIP-Pyr⁻** redox couples were estimated as the average of the anodic and cathodic peak potentials, yielding values of +0.85 and -0.83 V versus SCE, respectively.
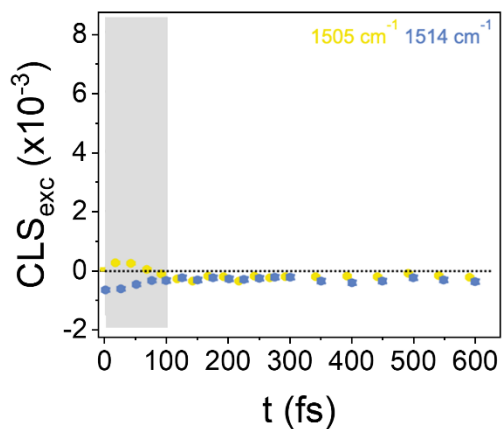
Figure 4.17 CLS dynamics of **PF₁₅-BIP-Pyr** for features unrelated to the BIP-Pyr (*i.e.*, localized on PF_{15}).[11] The time range in which visible and IR pulses overlap, <90 fs, is indicated by the gray area. The error bars indicated the standard error of the CLS, obtained by a linear fit of the conditional average.[9] A comparison to Figure 3.4b reveals a distinct lack of oscillatory (or any) dynamics for these features which are unrelated to the E2PT product.
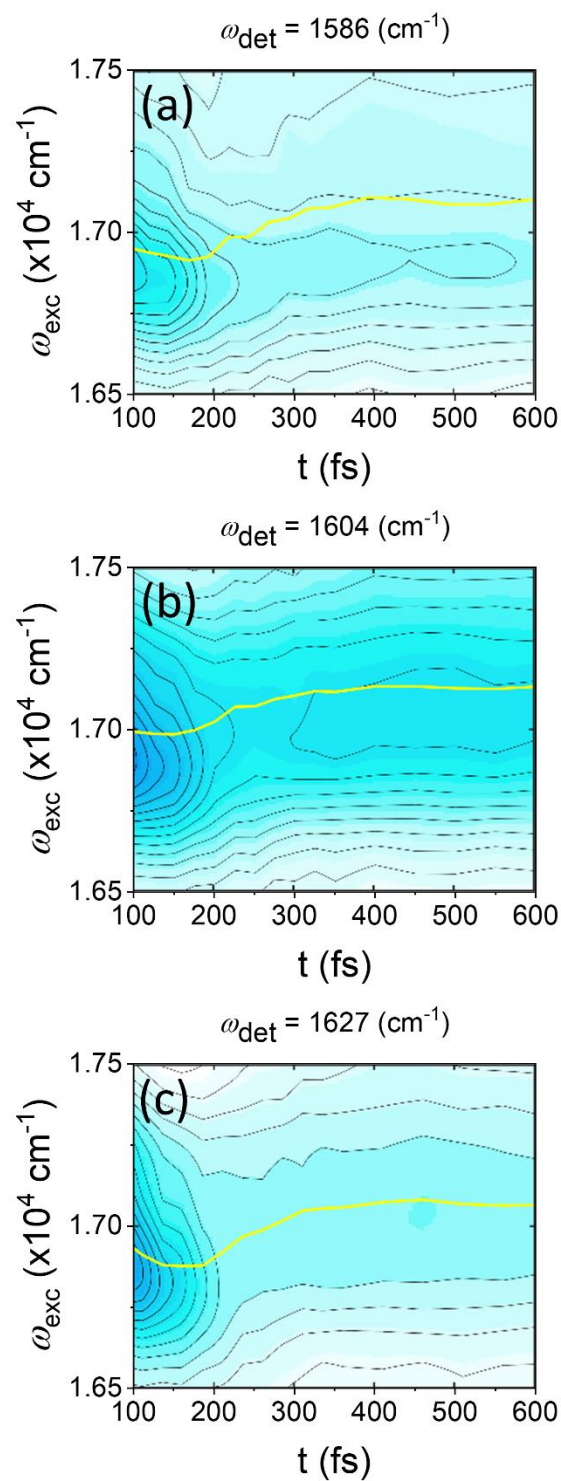
Figure 4.18 $\omega_{exc.}$ peak evolution of **PF₁₅-BIP-Pyr** at 1586 cm⁻¹, 1604 cm⁻¹, and 1627 cm⁻¹ corresponding to Figure 3.4a. The yellow line traces the peak maximum along the waiting time, *t*, obtained by fitting with a Gaussian function.
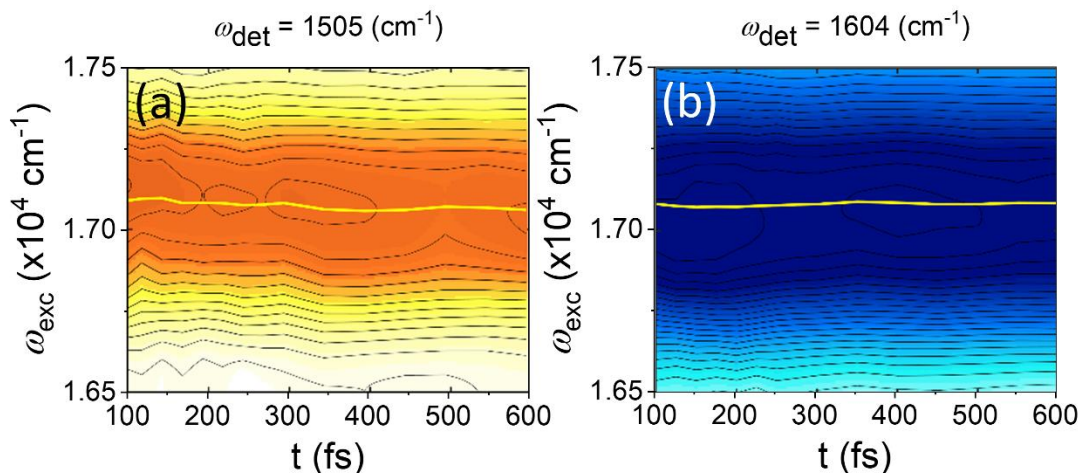
Figure 4.19 $\omega_{exc.}$ peak evolution of **PF$_{15}$-BIP-Pyr** for features unrelated to the BIP-Pyr (*i.e.*, localized on PF$_{15}$) at 1505 cm^{-1} and 1514 cm^{-1}.[11] The yellow line traces the peak maximum along the waiting time, *t*, obtained by fitting with a Gaussian function.
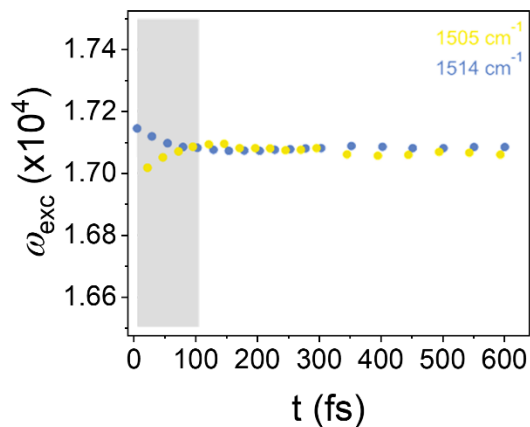
Figure 4.20 $\omega_{exc.}$ peak evolution of **PF$_{15}$-BIP-Pyr** for features unrelated to the BIP-Pyr (*i.e.*, localized on PF$_{15}$) at 1505 cm^{-1} and 1514 cm^{-1}.[11] The time range in which visible and IR pulses overlap, <90 fs, is indicated by the shaded area. A comparison to Figure 3.4a reveals a distinct lack of oscillatory (or any) dynamics for these features which are unrelated to the E2PT product.
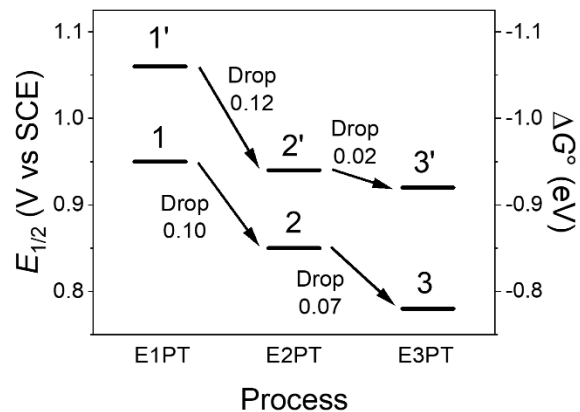
Figure 4.21 Graphic presentation of data in Table 3.3 showing changes in $E_{1/2}$ and ΔG^0.

Compounds **1**, **2** and **3** are not substituted with EWGs. Compound **1′** and **2′** each have

one EWG and compound **3′** has two EWGs. The arrows labeled "Drop" and the

associated numbers indicate the magnitude of the increase in ΔG^0 (eV) and corresponding

decrease in $E_{1/2}$ (V) between the indicated compounds.
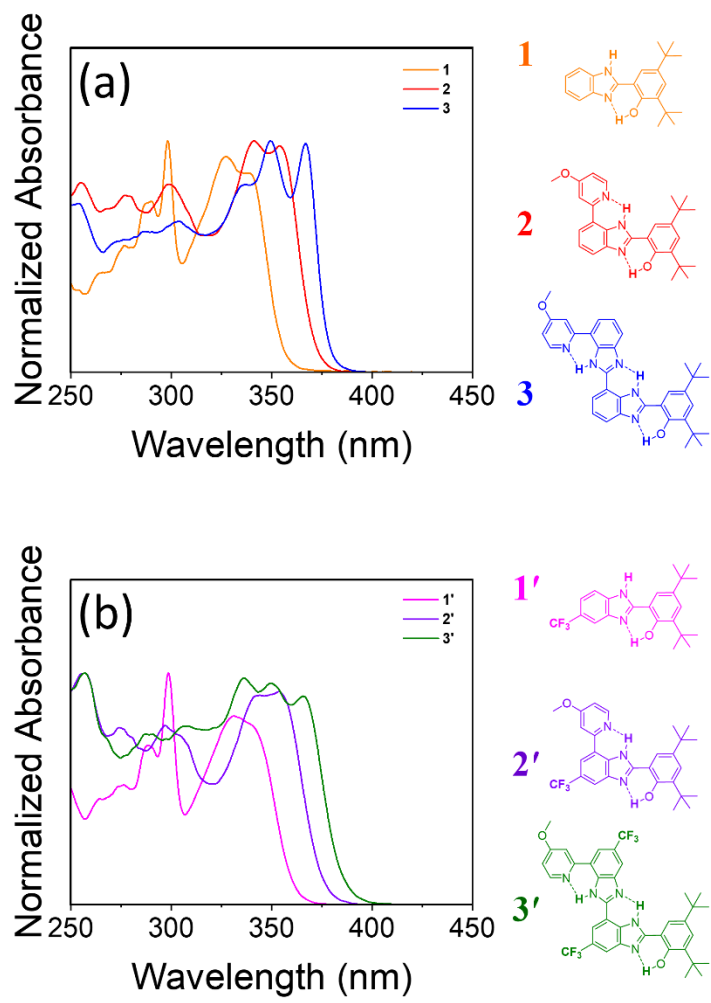
Figure 4.22 Steady-state absorption spectra of (a) **1-3** or (b) **1'-3** in CH_2Cl_2.

Table 4.4 Calculated Redox Potentials for Formation of E*n*PT Products in the Series **1-3** and **1'-3'** in CH_2Cl_2.[a]

Compound	E0PT	E1PT	E2PT	E3PT
1	1.50	1.11	N/A[b]	N/A[c]
1'	1.56	1.20	N/A[b]	N/A[c]
2	1.46	1.01	0.85	N/A[c]
2'	1.53	1.12	0.94[d]	N/A[c]
3	1.47	1.05	0.86	0.72
3'	1.59	1.23	1.04	0.82

[a] Redox potentials reported in V vs SCE.

[b] Compound cannot have an E2PT product.

[c] Compound cannot have an E3PT product.

[d] This redox potential was used as the reference and agrees with experiment by construction.

4.4 References

(1)   Connelly, N. G.; Geiger, W. E. Chemical Redox Agents for Organometallic Chemistry. *Chem. Rev.* **1996**, *96* (2), 877–910.

(2)   Briois, V.; Fonda, E.; Belin, S.; Barthe, L.; La Fontaine, C.; Langlois, F.; Ribbens, M.; Villain, F. SAMBA: The 4-40 KeV X-Ray Absorption Spectroscopy Beamline at SOLEIL. *UVX 2010* **2011**, 41–47.

(3)   Newville, M. EXAFS Analysis Using *FEFF* and *FEFFIT*. *J. Synchrotron Radiat.* **2001**, *8* (2), 96–100.

(4)   Khusnutdinova, D.; Beiler, A. M.; Wadsworth, B. L.; Jacob, S. I.; Moore, G. F. Metalloporphyrin-Modified Semiconductors for Solar Fuel Production. *Chem. Sci.* **2017**, *8* (1), 253–259.

(5)   Brennan, B. J.; Arero, J.; Liddell, P. A.; Moore, T. A.; Moore, A. L.; Gust, D. Selective Oxidative Synthesis of *Meso*-Beta Fused Porphyrin Dimers. *J. Porphyr. Phthalocyanines* **2013**, *17* (4), 247–251.

(6)   Oliver, T. A. A.; Lewis, N. H. C.; Fleming, G. R. Correlating the Motion of Electrons and Nuclei with Two-Dimensional Electronic-Vibrational Spectroscopy. *Proc. Natl. Acad. Sci. U.S.A.* **2014**, *111* (28), 10061–10066.

(7)   Myers, J. A.; Lewis, K. L. M.; Tekavec, P. F.; Ogilvie, J. P. Two-Color Two-Dimensional Fourier Transform Electronic Spectroscopy with a Pulse-Shaper. *Opt. Express* **2008**, *16* (22), 17420–17428.

(8)   Zhang, Z.; Wells, K. L.; Hyland, E. W. J.; Tan, H.-S. Phase-Cycling Schemes for Pump-Probe Beam Geometry Two-Dimensional Electronic Spectroscopy. *Chem. Phys. Lett.* **2012**, *550*, 156–161.

(9)   Wu, E. C.; Ge, Q.; Arsenault, E. A.; Lewis, N. H. C.; Gruenke, N. L.; Head-Gordon, M. J.; Fleming, G. R. Two-Dimensional Electronic-Vibrational Spectroscopic Study of Conical Intersection Dynamics: An Experimental and Electronic Structure Study. *Phys. Chem. Chem. Phys.* **2019**, *21* (26), 14153–14163.

(10)   Lewis, N. H. C.; Dong, H.; Oliver, T. A. A.; Fleming, G. R. Measuring Correlated Electronic and Vibrational Spectral Dynamics Using Line Shapes in Two-Dimensional Electronic-Vibrational Spectroscopy. *J. Chem. Phys.* **2015**, *142*, 174202.

(11)   Yoneda, Y.; Mora, S. J.; Shee, J.; Wadsworth, B. L.; Arsenault, E. A.; Hait, D.; Kodis, G.; Gust, D.; Moore, G. F.; Moore, A. L.; Head-Gordon, M.; Moore, T. A.; Fleming, G. R. Electron-Nuclear Dynamics Accompanying Proton-Coupled Electron Transfer. *J. Am. Chem. Soc.* **2021**, *143* (8), 3104–3112.

BIBLIOGRAPHY

(1)   Zeifman, L.; Hertog, S.; Kantorova, V.; Wilmoth, J. *A World of 8 Billion*; UN
        Department of Economic and Social Affair, **2022**.
        https://www.un.org/development/desa/dpad/publication/un-desa-policy-brief-no-
        140-a-world-of-8-billion/

(2)   Cozzi, L.; Gould, T. *World Energy Outlook 2022*; International Energy Agency,
        2022. https://www.iea.org/reports/world-energy-outlook-2022

(3)   National Oceanic and Atmospheric Administration. *Global Monitoring
        Laboratory - Carbon Cycle Greenhouse Gases*.

(4)   Lüthi, D.; Le Floch, M.; Bereiter, B.; Blunier, T.; Barnola, J. M.; Siegenthaler, U.;
        Raynaud, D.; Jouzel, J.; Fischer, H.; Kawamura, K.; Stocker, T. F. High-
        Resolution Carbon Dioxide Concentration Record 650,000-800,000 Years before
        Present. *Nature* **2008**, *453* (7193), 379–382.

(5)   Lewis, N. S.; Nocera, D. G. Powering the Planet: Chemical Challenges in Solar
        Energy Utilization. *Proc. Natl. Acad. Sci. U.S.A.* **2006**, *103* (43), 15729–15735.

(6)   Blankenship, R. E.; Tiede, D. M.; Barber, J.; Brudvig, G. W.; Fleming, G.;
        Ghirardi, M.; Gunner, M. R.; Junge, W.; Kramer, D. M.; Melis, A.; Moore, T. A.;
        Moser, C. C.; Nocera, D. G.; Nozik, A. J.; Ort, D. R.; Parson, W. W.; Prince, R.
        C.; Sayre, R. T. Comparing Photosynthetic and Photovoltaic Efficiencies and
        Recognizing the Potential for Improvement. *Science* **2011**, *332*, 805–809.

(7)   Gust, D.; Moore, T.; Moore, A. Solar Fuels via Artificial Photosynthesis. *Acc.
        Chem. Res.* **2009**, *42* (12), 1890–1898.

(8)   Listorti, A.; Durrant, J.; Barber, J. Artificial Photosynthesis: Solar to Fuel. *Nat.
        Mater.* **2009**, *8* (12), 929–930.

(9)   Faunce, T.; Styring, S.; Wasielewski, M. R.; Brudvig, G. W.; Rutherford, A. W.;
        Messinger, J.; Lee, A. F.; Hill, C. L.; Degroot, H.; Fontecave, M.; MacFarlane, D.
        R.; Hankamer, B.; Nocera, D. G.; Tiede, D. M.; Dau, H.; Hillier, W.; Wang, L.;
        Amal, R. Artificial Photosynthesis as a Frontier Technology for Energy
        Sustainability. *Energy Environ. Sci.* **2013**, *6* (4), 1074–1076.

(10)   Faunce, T. A.; Lubitz, W.; Rutherford, A. W.; MacFarlane, D.; Moore, G. F.;
        Yang, P.; Nocera, D. G.; Moore, T. A.; Gregory, D. H.; Fukuzumi, S.; Yoon, K.
        B.; Armstrong, F. A.; Wasielewski, M. R.; Styring, S. Energy and Environment
        Policy Case for a Global Project on Artificial Photosynthesis. *Energy Environ.
        Sci.* **2013**, *6* (3), 695–698.

(11)   Ardo, S.; Fernandez Rivas, D.; Modestino, M. A.; Schulze Greiving, V.; Abdi, F. F.; Alarcon Llado, E.; Artero, V.; Ayers, K.; Battaglia, C.; Becker, J. P.; Bederak, D.; Berger, A.; Buda, F.; Chinello, E.; Dam, B.; Di Palma, V.; Edvinsson, T.; Fujii, K.; Gardeniers, H.; Geerlings, H.; Hashemi, S. M.; Haussener, S.; Houle, F.; Huskens, J.; James, B. D.; Konrad, K.; Kudo, A.; Kunturu, P. P.; Lohse, D.; Mei, B.; Miller, E. L.; Moore, G. F.; Muller, J.; Orchard, K. L.; Rosser, T. E.; Saadi, F. H.; Schüttauf, J. W.; Seger, B.; Sheehan, S. W.; Smith, W. A.; Spurgeon, J.; Tang, M. H.; Van De Krol, R.; Vesborg, P. C. K.; Westerik, P. Pathways to Electrochemical Solar-Hydrogen Technologies. *Energy Environ. Sci.* **2018**, *11* (10), 2768–2783.

(12)   Archer, M. D.; Barber, J. *Series on Photoconversion of Solar Energy, Vol. 2: Molecular to Global Photosynthesis*; Imperial College Press: London, 2004.

(13)   120,000 TW Power of the Sun.

(14)   Fischer, W. W.; Hemp, J.; Johnson, J. E. Evolution of Oxygenic Photosynthesis. *Annu. Rev. Earth Planet. Sci.* **2016**, *44*, 647–683.

(15)   Gust, D.; Kramer, D.; Moore, A.; Moore, T. A.; Vermaas, W. Engineered and Artificial Photosynthesis: Human Ingenuity Enters the Game. *MRS Bull* **2008**, *33* (4), 383–387.

(16)   Faunce, T. Global Artificial Photosynthesis and Renewable Energy Storage and Policy for the Sustainocene. *Adv. Sustainable Syst.* **2018**, *2*, 1800035.

(17)   Tumas, B.; Dempsey, J. L.; Mallouk, T. E. *Basic Energy Sciences Roundtable on Liquid Solar Fuels*; 2019.

(18)   Thorp, H. H. Do Us a Favor. *Science* **2020**, *367* (6483), 1169.

(19)   Hemminger, J.; Fleming, G.; Ratner, M. *Directing Matter and Energy: Five Challenges for Science and the Imagination*; 2007.

(20)   Rutherford, A. W.; Moore, T. A. Mimicking Photosynthesis, but Just the Best Bits. *Nature* **2008**, *453* (7194), 449.

(21)   Green, B. R.; Parson, W. W. *Advances in Photosynthesis and Respiration, Vol. 13: Light-Harvesting Antennas in Photosynthesis*, 1st Ed.; Springer Netherlands: Dordrecht, 2003.

(22)   Moore, G. F.; Brudvig, G. W. Energy Conversion in Photosynthesis: A Paradigm for Solar Fuel Production. *Annu. Rev. Condens. Matter Phys.* **2011**, *2* (1), 303–327.

(23)   Blankenship, R. E. *Molecular Mechanisms of Photosynthesis*, 2nd Ed.; Wiley-Blackwell, 2014.

(24)   Long, S. P.; Humphries, S. Photoinhibition of Photosynthesis in Nature. *Annu. Rev. Plant Physiol. Plant Mol. Biol.* **1994**, *45*, 633–662.

(25)   Goh, C. H.; Ko, S. M.; Koh, S.; Kim, Y. J.; Bae, H. J. Photosynthesis and Environments: Photoinhibition and Repair Mechanisms in Plants. *J. Plant Biol.* **2012**, *55* (2), 93–101.

(26)   Durrant, J. R.; Giorgi, L. B.; Barber, J.; Klug, D. R.; Porter, G. Characterisation of Triplet States in Isolated Photosystem II Reaction Centres: Oxygen Quenching as a Mechanism for Photodamage. *Biochim. Biophys. Acta* **1990**, *1017* (2), 167–175.

(27)   Guergova-Kuras, M.; Boudreaux, B.; Joliot, A.; Joliot, P.; Redding, K. Evidence for Two Active Branches for Electron Transfer in Photosystem I. *Proc. Natl. Acad. Sci. U.S.A.* **2001**, *98* (8), 4437–4442.

(28)   Marcus, R. A.; Sutin, N. Electron Transfers in Chemistry and Biology. *Biochim Biophys Acta* **1985**, *811*, 265–322.

(29)   Moser, C. C.; Keske, J. M.; Warncke, K.; Farid, R. S.; Dutton, P. L. Nature of Biological Electron Transfer. *Nature* **1992**, *355*, 796–802.

(30)   Gray, H. B.; Winkler, J. R. Electron Transfer in Proteins. *Annu. Rev. Biochem.* **1996**, *65*, 537–561.

(31)   Bard, A. J.; Faulkner, L. R. *Electrochemical Methods: Fundamentals and Applications*, 2nd ed.; Wiley & Sons, 2001.

(32)   Savéant, J.-M.; Costentin, C. *Elements of Molecular and Biomolecular Electrochemistry: An Electrochemical Approach to Electron Transfer Chemistry*, 2nd Ed.; Wiley & Sons: Hoboken, 2019.

(33)   Ruben, S.; Randall, M.; Kamen, M.; Hyde, J. L. Heavy Oxygen (O[18]) as a Tracer in the Study of Photosynthesis. *J. Am. Chem. Soc.* **1941**, *63* (3), 877–879.

(34)   Gontero, B.; Lebreton, S.; Graciet, E. Multienzyme Complexes Involved in the Benson-Calvin Cycle and in Fatty Acid Metabolism. In *Annual Plant Reviews, Volume 7: Protein-Protein Interactions in Plant Biology*; McManus, M. T., Laing, W. A., Allan, A. C., Eds.; Sheffield Academic Press: Sheffield, 2002; pp 125–157.

(35)   Raines, C. A. The Calvin Cycle Revisited. *Photosynth. Res.* **2003**, *75*, 1–10.

(36)   Mitchell, P. Coupling of Phosphorylation to Electron and Hydrogen Transfer by a Chemi-Osmotic Type of Mechanism. *Nature* **1961**, *191* (4784), 144–148.

(37)   Mitchell, P. Chemiosmotic Coupling in Oxidative and Photosynthetic Phosphorylation. *Biochim. Biophys. Acta* **2011**, *1807* (12), 1507–1538.

(38)   Martin, J. L.; Ishmukhametov, R.; Hornung, T.; Ahmad, Z.; Frasch, W. D. Anatomy of F_1-ATPase Powered Rotation. *Proc. Natl. Acad. Sci. U.S.A.* **2014**, *111* (10), 3715–3720.

(39)   Junge, W.; Nelson, N. ATP Synthase. *Annu. Rev. Biochem.* **2015**, *84*, 631–657.

(40)   Cukier, R. I.; Nocera, D. G. Proton-Coupled Electron Transfer. *Annu. Rev. Phys. Chem.* **1998**, *49*, 337–369.

(41)   Mayer, J. M. Proton-Coupled Electron Transfer: A Reaction Chemist's View. *Annu. Rev. Phys. Chem.* **2004**, *55*, 363–390.

(42)   Huynh, M. H. V.; Meyer, T. J. Proton-Coupled Electron Transfer. *Chem. Rev.* **2007**, *107* (11), 5004–5064.

(43)   Hammarström, L.; Styring, S. Coupled Electron Transfers in Artificial Photosynthesis. *Philos. Trans. R. Soc. B: Biol. Sci.* **2008**, *363* (1494), 1283–1291.

(44)   Hammes-Schiffer, S. Theory of Proton-Coupled Electron Transfer in Energy Conversion Processes. *Acc. Chem. Res.* **2009**, *42* (12), 1881–1889.

(45)   Dempsey, J. L.; Winkler, J. R.; Gray, H. B. Proton-Coupled Electron Flow in Protein Redox Machines. *Chem. Rev.* **2010**, *110* (12), 7024–7039.

(46)   Hammarström, L.; Styring, S. Proton-Coupled Electron Transfer of Tyrosines in Photosystem II and Model Systems for Artificial Photosynthesis: The Role of a Redox-Active Link between Catalyst and Photosensitizer. *Energy Environ. Sci.* **2011**, *4* (7), 2379–2388.

(47)   Weinberg, D. R.; Gagliardi, C. J.; Hull, J. F.; Murphy, C. F.; Kent, C. A.; Westlake, B. C.; Paul, A.; Ess, D. H.; McCafferty, D. G.; Meyer, T. J. Proton-Coupled Electron Transfer. *Chem. Rev.* **2012**, *112* (7), 4016–4093.

(48)   Hammes-Schiffer, S. Proton-Coupled Electron Transfer: Moving Together and Charging Forward. *J. Am. Chem. Soc.* **2015**, *137* (28), 8860–8871.

(49)   Mora, S. J.; Odella, E.; Moore, G. F.; Gust, D.; Moore, T. A.; Moore, A. L. Proton-Coupled Electron Transfer in Artificial Photosynthetic Systems. *Acc. Chem. Res.* **2018**, *51* (2), 445–453.

(50)   Chen, H. Y.; Ardo, S. Direct Observation of Sequential Oxidations of a Titania-Bound Molecular Proxy Catalyst Generated through Illumination of Molecular Sensitizers. *Nat. Chem.* **2018**, *10* (1), 17–23.

(51)   Berardi, S.; Drouet, S.; Francàs, L.; Gimbert-Suriñach, C.; Guttentag, M.; Richmond, C.; Stoll, T.; Llobet, A. Molecular Artificial Photosynthesis. *Chem. Soc. Rev.* **2014**, *43* (22), 7501–7519.

(52)   Hammarström, L. Accumulative Charge Separation for Solar Fuels Production: Coupling Light-Induced Single Electron Transfer to Multielectron Catalysis. *Acc. Chem. Res.* **2015**, *48* (3), 840–850.

(53)   Lindley, B. M.; Appel, A. M.; Krogh-Jespersen, K.; Mayer, J. M.; Miller, A. J. M. Evaluating the Thermodynamics of Electrocatalytic N_2 Reduction in Acetonitrile. *ACS Energy Lett.* **2016**, *1* (4), 698–704.

(54)   Li, H.; Li, J.; Ai, Z.; Jia, F.; Zhang, L. Oxygen Vacancy-Mediated Photocatalysis of BiOCl: Reactivity, Selectivity, and Perspectives. *Angew. Chem. Int. Ed.* **2018**, *57* (1), 122–138.

(55)   Beiler, A. M.; Moore, G. F. Multi-Electron-Transfer Photochemistry: Caught in the Act. *Nat. Chem.* **2018**, *10* (1), 3–4.

(56)   Chen, X.; Li, N.; Kong, Z.; Ong, W. J.; Zhao, X. Photocatalytic Fixation of Nitrogen to Ammonia: State-of-the-Art Advancements and Future Prospects. *Mater. Horiz.* **2018**, *5* (1), 9–27.

(57)   Woodrow, I. E. Enzymatic Regulation Photosynthetic CO_2 Fixation in C_3 Plants. *Annu. Rev. Plant Physiol. Plant Mol. Biol.* **1988**, *39* (1009), 533–594.

(58)   Evans, D. J.; Pickett, C. J. Chemistry and the Hydrogenases. *Chem. Soc. Rev.* **2003**, *32* (5), 268–275.

(59)   Bachmeier, A.; Armstrong, F. A. Solar-Driven Proton and Carbon Dioxide Reduction to Fuels - Lessons from Metalloenzymes. *Curr. Opin. Chem. Biol.* **2015**, *25*, 141–151.

(60)   Del Barrio, M.; Sensi, M.; Orain, C.; Baffert, C.; Dementin, S.; Fourmond, V.; Léger, C. Electrochemical Investigations of Hydrogenases and Other Enzymes That Produce and Use Solar Fuels. *Acc. Chem. Res.* **2018**, *51* (3), 769–777.

(61)   Evans, R. M.; Siritanaratkul, B.; Megarity, C. F.; Pandey, K.; Esterle, T. F.; Badiani, S.; Armstrong, F. A. The Value of Enzymes in Solar Fuels Research -

Efficient Electrocatalysts through Evolution. *Chem. Soc. Rev.* **2019**, *48*, 2039–2052.

(62) Cracknell, J. A.; Vincent, K. A.; Armstrong, F. A. Enzymes as Working or Inspirational Electrocatalysts for Fuel Cells and Electrolysis. *Chem. Rev.* **2008**, *108* (7), 2439–2461.

(63) Armstrong, F. A.; Hirst, J. Reversibility and Efficiency in Electrocatalytic Energy Conversion and Lessons from Enzymes. *Proc. Natl. Acad. Sci. U.S.A.* **2011**, *108* (34), 14049–14051.

(64) Shaw, W. J. The Outer-Coordination Sphere: Incorporating Amino Acids and Peptides as Ligands for Homogeneous Catalysts to Mimic Enzyme Function. *Catal. Rev. Sci. Eng.* **2012**, *54* (4), 489–550.

(65) Zhao, M.; Wang, H. B.; Ji, L. N.; Mao, Z. W. Insights into Metalloenzyme Microenvironments: Biomimetic Metal Complexes with a Functional Second Coordination Sphere. *Chem. Soc. Rev.* **2013**, *42* (21), 8360–8375.

(66) Gunner, M. R.; Honig, B. Electrostatic Control of Midpoint Potentials in the Cytochrome Subunit of the *Rhodopseudomonas Viridis* Reaction Center. *Proc. Natl. Acad. Sci. U.S.A.* **1991**, *88* (20), 9151–9155.

(67) Mao, J.; Hauser, K.; Gunner, M. R. How Cytochromes with Different Folds Control Heme Redox Potentials. *Biochemistry* **2003**, *42* (33), 9829–9840.

(68) Gray, H. B.; Stiefel, E. I.; Valentine, J. S.; Bertini, I. *Biological Inorganic Chemistry Structure and Reactivity*, 1st Ed.; University Science Books, 2007.

(69) Zheng, Z.; Gunner, M. R. Analysis of the Electrochemistry of Hemes with E_ms Spanning 800 MV. *Proteins* **2009**, *75* (3), 719–734.

(70) Liu, J.; Chakraborty, S.; Hosseinzadeh, P.; Yu, Y.; Tian, S.; Petrik, I.; Bhagi, A.; Lu, Y. Metalloproteins Containing Cytochrome, Iron-Sulfur, or Copper Redox Centers. *Chem. Rev.* **2014**, *114* (8), 4366–4369.

(71) Zamost, B. L.; Nielsen, H. K.; Starnes, R. L. Thermostable Enzymes for Industrial Applications. *J. Ind. Microbiol. Biotechnol.* **1991**, *8*, 71–81.

(72) Tye, J. W.; Hall, M. B.; Darensbourg, M. Y. Better than Platinum? Fuel Cells Energized by Enzymes. *Proc. Natl. Acad. Sci. U.S.A.* **2005**, *102* (47), 16911–16912.

(73) Meredith, M. T.; Minteer, S. D. Biofuel Cells: Enhanced Enzymatic Bioelectrocatalysis. *Annu. Rev. Anal. Chem.* **2012**, *5*, 157–179.

(74) Woolerton, T. W.; Sheard, S.; Chaudhary, Y. S.; Armstrong, F. A. Enzymes and Bio-Inspired Electrocatalysts in Solar Fuel Devices. *Energy Environ. Sci.* **2012**, *5* (6), 7470–7490.

(75) Liese, A.; Hilterhaus, L. Evaluation of Immobilized Enzymes for Industrial Applications. *Chem. Soc. Rev.* **2013**, *42* (15), 6236–6249.

(76) Rasmussen, M.; Abdellaoui, S.; Minteer, S. D. Enzymatic Biofuel Cells: 30 Years of Critical Advancements. *Biosens. Bioelectron.* **2016**, *76*, 91–102.

(77) Porter, J. L.; Rusli, R. A.; Ollis, D. L. Directed Evolution of Enzymes for Industrial Biocatalysis. *ChemBioChem* **2016**, *17* (3), 197–203.

(78) Frey, M. Hydrogenases: Hydrogen-Activating Enzymes. *ChemBioChem* **2002**, *3*, 153–160.

(79) Cammack, R. Hydrogenase Sophistication. *Nature* **1999**, *397* (6716), 214–215.

(80) Lee, C. Y.; Park, H. S.; Fontecilla-Camps, J. C.; Reisner, E. Photoelectrochemical H_2 Evolution with a Hydrogenase Immobilized on a TiO_2-Protected Silicon Electrode. *Angew. Chem. Int. Ed.* **2016**, *55* (20), 5971–5974.

(81) Alfonta, L.; Zhang, Z.; Uryu, S.; Loo, J. A.; Schultz, P. G. Site-Specific Incorporation of a Redox-Active Amino Acid into Proteins. *J. Am. Chem. Soc.* **2003**, *125* (48), 14662–14663.

(82) Landwehr, M.; Carbone, M.; Otey, C. R.; Li, Y.; Arnold, F. H. Diversification of Catalytic Function in a Synthetic Family of Chimeric Cytochrome P450s. *Chem. Biol.* **2007**, *14* (3), 269–278.

(83) Jones, A. K.; Lichtenstein, B. R.; Dutta, A.; Gordon, G.; Dutton, P. L. Synthetic Hydrogenases: Incorporation of an Iron Carbonyl Thiolate into a Designed Peptide. *J. Am. Chem. Soc.* **2007**, *129*, 14844–14845.

(84) Ugwumba, I. N.; Ozawa, K.; Xu, Z. Q.; Ely, F.; Foo, J. L.; Herlt, A. J.; Coppin, C.; Brown, S.; Taylor, M. C.; Ollis, D. L.; Mander, L. N.; Schenk, G.; Dixon, N. E.; Otting, G.; Oakeshott, J. G.; Jackson, C. J. Improving a Natural Enzyme Activity through Incorporation of Unnatural Amino Acids. *J. Am. Chem. Soc.* **2011**, *133* (2), 326–333.

(85) Dong, Z.; Luo, Q.; Liu, J. Artificial Enzymes Based on Supramolecular Scaffolds. *Chem. Soc. Rev.* **2012**, *41* (23), 7890–7908.

(86)   Faiella, M.; Roy, A.; Sommer, D.; Ghirlanda, G. De Novo Design of Functional Proteins: Toward Artificial Hydrogenases. *Biopolymers* **2013**, *100* (6), 558–571.

(87)   Roy, S.; Nguyen, T. A. D.; Gan, L.; Jones, A. K. Biomimetic Peptide-Based Models of [FeFe]-Hydrogenases: Utilization of Phosphine-Containing Peptides. *Dalton Trans.* **2015**, *44* (33), 14865–14876.

(88)   Mak, W. S.; Tran, S.; Marcheschi, R.; Bertolani, S.; Thompson, J.; Baker, D.; Liao, J. C.; Siegel, J. B. Integrative Genomic Mining for Enzyme Function to Enable Engineering of a Non-Natural Biosynthetic Pathway. *Nat. Commun.* **2015**, *6*, 1–9.

(89)   Alcala-Torano, R.; Sommer, D. J.; Bahrami Dizicheh, Z.; Ghirlanda, G. Design Strategies for Redox Active Metalloenzymes: Applications in Hydrogen Production. In *Methods in Enzymology, Volume 580: Peptide, Protein and Enzyme Design*; Pecoraro, V. L., Ed.; Academic Press: Cambridge, 2016; pp 389–416.

(90)   Sakimoto, K. K.; Kornienko, N.; Yang, P. Cyborgian Material Design for Solar Fuel Production: The Emerging Photosynthetic Biohybrid Systems. *Acc. Chem. Res.* **2017**, *50* (3), 476–481.

(91)   Nocera, D. G. Solar Fuels and Solar Chemicals Industry. *Acc. Chem. Res.* **2017**, *50* (3), 616–619.

(92)   Berggren, G.; Adamska, A.; Lambertz, C.; Simmons, T. R.; Esselborn, J.; Atta, M.; Gambarelli, S.; Mouesca, J. M.; Reijerse, E.; Lubitz, W.; Happe, T.; Artero, V.; Fontecave, M. Biomimetic Assembly and Activation of [FeFe]-Hydrogenases. *Nature* **2013**, *499* (7456), 66–69.

(93)   Slater, J. W.; Marguet, S. C.; Monaco, H. A.; Shafaat, H. S. Going beyond Structure: Nickel-Substituted Rubredoxin as a Mechanistic Model for the [NiFe] Hydrogenases. *J. Am. Chem. Soc.* **2018**, *140* (32), 10250–10262.

(94)   Helm, M. L.; Stewart, M. P.; Bullock, R. M.; Rakowski DuBois, M.; DuBois, D. L. A Synthetic Nickel Electrocatalyst with a Turnover Frequency Above 100,000 s^{-1} for H$_2$ Production. *Science* **2011**, *333* (6044), 863–866.

(95)   Gross, M. A.; Reynal, A.; Durrant, J. R.; Reisner, E. Versatile Photocatalytic Systems for H$_2$ Generation in Water Based on an Efficient DuBois-Type Nickel Catalyst. *J. Am. Chem. Soc.* **2014**, *136*, 356–366.

(96)   Das, A. K.; Engelhard, M. H.; Bullock, R. M.; Roberts, J. A. S. A Hydrogen-Evolving Ni(P$_2$N$_2$)$_2$ Electrocatalyst Covalently Attached to a Glassy Carbon

Electrode: Preparation, Characterization, and Catalysis. Comparisons with the Homogeneous Analogue. *Inorg. Chem.* **2014**, *53* (13), 6875–6885.

(97)   Leung, J. J.; Warnan, J.; Nam, D. H.; Zhang, J. Z.; Willkomm, J.; Reisner, E. Photoelectrocatalytic H_2 Evolution in Water with Molecular Catalysts Immobilised on p-Si *via* a Stabilising Mesoporous TiO_2 Interlayer. *Chem. Sci.* **2017**, *8* (7), 5172–5180.

(98)   Jain, A.; Lense, S.; Linehan, J. C.; Raugei, S.; Cho, H.; Dubois, D. L.; Shaw, W. J. Incorporating Peptides in the Outer-Coordination Sphere of Bioinspired Electrocatalysts for Hydrogen Production. *Inorg. Chem.* **2011**, *50* (9), 4073–4085.

(99)   Jain, A.; Reback, M. L.; Lindstrom, M. Lou; Thogerson, C. E.; Helm, M. L.; Appel, A. M.; Shaw, W. J. Investigating the Role of the Outer-Coordination Sphere in $[Ni(P^{Ph}_2N^{Ph-R}_2)_2]^{2+}$ Hydrogenase Mimics. *Inorg. Chem.* **2012**, *51* (12), 6592–6602.

(100)   Reback, M. L.; Ginovska-Pangovska, B.; Ho, M. H.; Jain, A.; Squier, T. C.; Raugei, S.; Roberts, J. A. S.; Shaw, W. J. The Role of a Dipeptide Outer-Coordination Sphere on H_2-Production Catalysts: Influence on Catalytic Rates and Electron Transfer. *Chem. Eur. J.* **2013**, *19*, 1928–1941.

(101)   Ginovska-Pangovska, B.; Dutta, A.; Reback, M. L.; Linehan, J. C.; Shaw, W. J. Beyond the Active Site: The Impact of the Outer Coordination Sphere on Electrocatalysts for Hydrogen Production and Oxidation. *Acc. Chem. Res.* **2014**, *47* (8), 2621–2630.

(102)   Grunes, J.; Zhu, J.; Somorjai, G. A. Catalysis and Nanoscience. *Chem. Commun.* **2003**, *3* (18), 2257–2260.

(103)   Hambourger, M.; Moore, G. F.; Kramer, D. M.; Gust, D.; Moore, A. L.; Moore, T. A. Biology and Technology for Photochemical Fuel Production. *Chem. Soc. Rev.* **2009**, *38* (1), 25–35.

(104)   Benson, E. E.; Kubiak, C. P.; Sathrum, A. J.; Smieja, J. M. Electrocatalytic and Homogeneous Approaches to Conversion of CO_2 to Liquid Fuels. *Chem. Soc. Rev.* **2009**, *38* (1), 89–99.

(105)   Kamat, P. V.; Tvrdy, K.; Baker, D. R.; Radich, E. J. Beyond Photovoltaics: Semiconductor Nanoarchitectures for Liquid-Junction Solar Cells. *Chem. Rev.* **2010**, *110* (11), 6664–6688.

(106)   Kumar, B.; Llorente, M.; Froehlich, J.; Dang, T.; Sathrum, A.; Kubiak, C. P. Photochemical and Photoelectrochemical Reduction of CO_2. *Annu. Rev. Phys. Chem.* **2012**, *63*, 541–569.

(107) Koval, C. A.; Lercher, J.; Scott, S. L. *Basic Research Needs for Catalysis Science to Transform Energy Technologies*; Washington, DC, 2017.

(108) Ye, R.; Zhao, J.; Wickemeyer, B. B.; Toste, F. D.; Somorjai, G. A. Foundations and Strategies of the Construction of Hybrid Catalysts for Optimized Performances. *Nat. Catal.*. Nature Publishing Group May 1, 2018, pp 318–325.

(109) Mizuno, N.; Misono, M. Heterogeneous Catalysis. *Chem. Rev.* **1998**, *98* (1), 199–217.

(110) McKone, J. R.; Marinescu, S. C.; Brunschwig, B. S.; Winkler, J. R.; Gray, H. B. Earth-Abundant Hydrogen Evolution Electrocatalysts. *Chem. Sci.* **2014**, *5* (3), 865–878.

(111) Rakowski DuBois, M.; Du Bois, D. L. The Roles of the First and Second Coordination Spheres in the Design of Molecular Catalysts for H_2 Production and Oxidation. *Chem. Soc. Rev.* **2009**, *38* (1), 62–72.

(112) Araki, K.; Wagner, M. J.; Wrighton, M. S. Layer-by-Layer Growth of Electrostatically Assembled Multilayer Porphyrin Films. *Langmuir* **1996**, *12* (22), 5393–5398.

(113) Campbell, W. M.; Jolley, K. W.; Wagner, P.; Wagner, K.; Walsh, P. J.; Gordon, K. C.; Schmidt-Mende, L.; Nazeeruddin, M. K.; Wang, Q.; Grätzel, M.; Officer, D. L. Highly Efficient Porphyrin Sensitizers for Dye-Sensitized Solar Cells. *J. Phys. Chem. C* **2007**, *111* (32), 11760–11762.

(114) Moore, G. F.; Hambourger, M.; Gervaldo, M.; Poluektov, O. G.; Rajh, T.; Gust, D.; Moore, T. A.; Moore, A. L. A Bioinspired Construct That Mimics the Proton Coupled Electron Transfer between P680$^{\bullet+}$ and the Tyr$_z$-His190 Pair of Photosystem II. *J. Am. Chem. Soc.* **2008**, *130* (32), 10466–10467.

(115) Subbaiyan, N. K.; Wijesinghe, C. A.; D'Souza, F. Supramolecular Solar Cells: Surface Modification of Nanocrystalline TiO_2 with Coordinating Ligands to Immobilize Sensitizers and Dyads via Metal-Ligand Coordination for Enhanced Photocurrent Generation. *J. Am. Chem. Soc.* **2009**, *131* (41), 14646–14647.

(116) Lindsey, J. S.; Bocian, D. F. Molecules for Charge-Based Information Storage. *Acc. Chem. Res.* **2011**, *44* (8), 638–650.

(117) Moore, G. F.; Blakemore, J. D.; Milot, R. L.; Hull, J. F.; Song, H.; Cai, L.; Schmuttenmaer, C. A.; Crabtree, R. H.; Brudvig, G. W. A Visible Light Water-Splitting Cell with a Photoanode Formed by Codeposition of a High-Potential

Porphyrin and an Iridium Water-Oxidation Catalyst. *Energy Environ. Sci.* **2011**, *4* (7), 2389–2392.

(118) Ardo, S.; Achey, D.; Morris, A. J.; Abrahamsson, M.; Meyer, G. J. Non-Nernstian Two-Electron Transfer Photocatalysis at Metalloporphyrin- TiO_2 Interfaces. *J. Am. Chem. Soc.* **2011**, *133* (41), 16572–16580.

(119) Auwärter, W.; Écija, D.; Klappenberger, F.; Barth, J. V. Porphyrins at Interfaces. *Nat. Chem.* **2015**, *7* (2), 105–120.

(120) Swierk, J. R.; Méndez-Hernández, D. D.; McCool, N. S.; Liddell, P.; Terazono, Y.; Pahk, I.; Tomlin, J. J.; Oster, N. V.; Moore, T. A.; Moore, A. L.; Gust, D.; Mallouk, T. E. Metal-Free Organic Sensitizers for Use in Water-Splitting Dye-Sensitized Photoelectrochemical Cells. *Proc. Natl. Acad. Sci. U.S.A.* **2015**, *112* (6), 1681–1686.

(121) Civic, M. R.; Dinolfo, P. H. Electrochemical Rectification of Redox Mediators Using Porphyrin-Based Molecular Multilayered Films on ITO Electrodes. *ACS Appl. Mater. Interfaces* **2016**, *8* (31), 20465–20473.

(122) Collin, J. P.; Sauvage, J. P. Electrochemical Reduction of Carbon Dioxide Mediated by Molecular Catalysts. *Coord. Chem. Rev.* **1989**, *93*, 245–268.

(123) Bhugun, I.; Lexa, D.; Savéant, J.-M. Homogeneous Catalysis of Electrochemical Hydrogen Evolution by Iron(0) Porphyrins. *J. Am. Chem. Soc.* **1996**, *118* (16), 3982–3983.

(124) Dhanasekaran, T.; Grodkowski, J.; Neta, P.; Hambright, P.; Fujita, E. *P*-Terphenyl-Sensitized Photoreduction of CO_2 with Cobalt and Iron Porphyrins. Interaction between CO and Reduced Metalloporphyrins. *J. Phys. Chem. A* **1999**, *103* (38), 7742–7748.

(125) Savéant, J.-M. Molecular Catalysis of Electrochemical Reactions. Mechanistic Aspects. *Chem. Rev.* **2008**, *108* (7), 2348–2378.

(126) Morris, A. J.; Meyer, G. J.; Fujita, E. Molecular Approaches to the Photocatalytic Reduction of Carbon Dioxide for Solar Fuels. *Acc. Chem. Res.* **2009**, *42* (12), 1983–1994.

(127) Losse, S.; Vos, J. G.; Rau, S. Catalytic Hydrogen Production at Cobalt Centres. *Coord. Chem. Rev.* **2010**, *254*, 2492–2504.

(128) Lee, C. H.; Dogutan, D. K.; Nocera, D. G. Hydrogen Generation by Hangman Metalloporphyrins. *J. Am. Chem. Soc.* **2011**, *133* (23), 8775–8777.

(129) Roubelakis, M. M.; Bediako, D. K.; Dogutan, D. K.; Nocera, D. G. Proton-Coupled Electron Transfer Kinetics for the Hydrogen Evolution Reaction of Hangman Porphyrins. *Energy Environ. Sci.* **2012**, *5* (7), 7737–7740.

(130) Yao, S. A.; Ruther, R. E.; Zhang, L.; Franking, R. A.; Hamers, R. J.; Berry, J. F. Covalent Attachment of Catalyst Molecules to Conductive Diamond: CO_2 Reduction Using "Smart" Electrodes. *J. Am. Chem. Soc.* **2012**, *134* (38), 15632–15635.

(131) Costentin, C.; Drouet, S.; Robert, M.; Savéant, J.-M. A Local Proton Source Enhances CO_2 Electroreduction to CO by a Molecular Fe Catalyst. *Science* **2012**, *338* (6103), 90–94.

(132) Costentin, C.; Robert, M.; Savéant, J.-M. Catalysis of the Electrochemical Reduction of Carbon Dioxide. *Chem. Soc. Rev.* **2013**, *42* (6), 2423–2436.

(133) Costentin, C.; Robert, M.; Savéant, J.-M. Current Issues in Molecular Catalysis Illustrated by Iron Porphyrins as Catalysts of the CO_2-to-CO Electrochemical Conversion. *Acc. Chem. Res.* **2015**, *48* (12), 2996–3006.

(134) Hod, I.; Sampson, M. D.; Deria, P.; Kubiak, C. P.; Farha, O. K.; Hupp, J. T. Fe-Porphyrin-Based Metal-Organic Framework Films as High-Surface Concentration, Heterogeneous Catalysts for Electrochemical Reduction of CO_2. *ACS Catal.* **2015**, *5* (11), 6302–6309.

(135) Oveisi, A. R.; Zhang, K.; Khorramabadi-zad, A.; Farha, O. K.; Hupp, J. T. Stable and Catalytically Active Iron Porphyrin-Based Porous Organic Polymer: Activity as Both a Redox and Lewis Acid Catalyst. *Sci. Rep.* **2015**, *5*, 10621.

(136) Lin, S.; Diercks, C. S.; Zhang, Y.-B.; Kornienko, N.; Nichols, E. M.; Zhao, Y.; Paris, A. R.; Kim, D.; Yang, P.; Yaghi, O. M.; Chang, C. J. Covalent Organic Frameworks Comprising Cobalt Porphyrins for Catalytic CO_2 Reduction in Water. *Science* **2015**, *349* (6253), 1208–1213.

(137) Weng, Z.; Jiang, J.; Wu, Y.; Wu, Z.; Guo, X.; Materna, K. L.; Liu, W.; Batista, V. S.; Brudvig, G. W.; Wang, H. Electrochemical CO_2 Reduction to Hydrocarbons on a Heterogeneous Molecular Cu Catalyst in Aqueous Solution. *J. Am. Chem. Soc.* **2016**, *138* (26), 8076–8079.

(138) Azcarate, I.; Costentin, C.; Robert, M.; Savéant, J.-M. Through-Space Charge Interaction Substituent Effects in Molecular Catalysis Leading to the Design of the Most Efficient Catalyst of CO_2-to-CO Electrochemical Conversion. *J. Am. Chem. Soc.* **2016**, *138* (51), 16639–16644.

(139) Beiler, A. M.; Khusnutdinova, D.; Wadsworth, B. L.; Moore, G. F. Cobalt Porphyrin-Polypyridyl Surface Coatings for Photoelectrosynthetic Hydrogen Production. *Inorg. Chem.* **2017**, *56* (20), 12178–12185.

(140) Khusnutdinova, D.; Beiler, A. M.; Wadsworth, B. L.; Jacob, S. I.; Moore, G. F. Metalloporphyrin-Modified Semiconductors for Solar Fuel Production. *Chem. Sci.* **2017**, *8* (1), 253–259.

(141) Bullock, R. M.; Das, A. K.; Appel, A. M. Surface Immobilization of Molecular Electrocatalysts for Energy Conversion. *Chem. Eur. J.* **2017**, *23* (32), 7626–7641.

(142) Vesborg, P. C. K.; Jaramillo, T. F. Addressing the Terawatt Challenge: Scalability in the Supply of Chemical Elements for Renewable Energy. *RSC Adv.* **2012**, *2* (21), 7933–7947.

(143) Friedman, D.; Masciangioli, T.; Olson, S. *The Role of the Chemical Sciences in Finding Alternatives to Critical Resources: A Workshop Summary*; National Academies Press, 2012.

(144) Wiese, S.; Kilgore, U. J.; Ho, M.-H.; Raugei, S.; Dubois, D. L.; Bullock, R. M.; Helm, M. L. Hydrogen Production Using Nickel Electrocatalysts with Pendant Amines: Ligand Effects on Rates and Overpotentials. *ACS Catal.* **2013**, *3* (11), 2527–2535.

(145) Bacchi, M.; Berggren, G.; Niklas, J.; Veinberg, E.; Mara, M. W.; Shelby, M. L.; Poluektov, O. G.; Chen, L. X.; Tiede, D. M.; Cavazza, C.; Field, M. J.; Fontecave, M.; Artero, V. Cobaloxime-Based Artificial Hydrogenases. *Inorg. Chem.* **2014**, *53* (15), 8071–8082.

(146) Queyriaux, N.; Kaeffer, N.; Morozan, A.; Chavarot-Kerlidou, M.; Artero, V. Molecular Cathode and Photocathode Materials for Hydrogen Evolution in Photoelectrochemical Devices. *J. Photochem. Photobiol. C: Photochem. Rev.* **2015**, *25*, 90–105.

(147) Dutta, A.; Ginovska, B.; Raugei, S.; Roberts, J. A. S.; Shaw, W. J. Optimizing Conditions for Utilization of an H_2 Oxidation Catalyst with Outer Coordination Sphere Functionalities. *Dalton Trans.* **2016**, *45* (24), 9786–9793.

(148) Tsay, C.; Yang, J. Y. Electrocatalytic Hydrogen Evolution under Acidic Aqueous Conditions and Mechanistic Studies of a Highly Stable Molecular Catalyst. *J. Am. Chem. Soc.* **2016**, *138* (43), 14174–14177.

(149) Maher, A. G.; Passard, G.; Dogutan, D. K.; Halbach, R. L.; Anderson, B. L.; Gagliardi, C. J.; Taniguchi, M.; Lindsey, J. S.; Nocera, D. G. Hydrogen Evolution

Catalysis by a Sparsely Substituted Cobalt Chlorin. *ACS Catal.* **2017**, *7* (5), 3597–3606.

(150) Lin, V. S.-Y.; DiMagno, S. G.; Therien, M. J. Highly Conjugated, Acetylenyl Bridged Porphyrins: New Models for Light-Harvesting Antenna Systems. *Science* **1994**, *264* (5162), 1105–1111.

(151) Anderson, H. L. Building Molecular Wires from the Colours of Life: Conjugated Porphyrin Oligomers. *Chem. Commun.* **1999**, *23*, 2323–2330.

(152) Tsuda, A.; Furuta, H.; Osuka, A. Completely Fused Diporphyrins and Triporphyrin. *Angew. Chem.* **2000**, *112* (14), 2649–2652.

(153) Tsuda, A.; Osuka, A. Fully Conjugated Porphyrin Tapes with Electronic Absorption Bands That Reach into Infrared. *Science* **2001**, *293* (5527), 79–82.

(154) Kim, D.; Osuka, A. Photophysical Properties of Directly Linked Linear Porphyrin Arrays. *J. Phys. Chem. A* **2003**, *107* (42), 8791–8816.

(155) Cheng, F.; Zhang, S.; Adronov, A.; Echegoyen, L.; Diederich, F. Triply Fused Zn^{II}-Porphyrin Oligomers: Synthesis, Properties, and Supramolecular Interactions with Single-Walled Carbon Nanotubes (SWNTs). *Chem. Eur. J.* **2006**, *12* (23), 6062–6070.

(156) Tanaka, T.; Lee, B. S.; Aratani, N.; Yoon, M.-C.; Kim, D.; Osuka, A. Synthesis and Properties of Hybrid Porphyrin Tapes. *Chem. Eur. J.* **2011**, *17* (51), 14400–14412.

(157) Brennan, B. J.; Arero, J.; Liddell, P. A.; Moore, T. A.; Moore, A. L.; Gust, D. Selective Oxidative Synthesis of *Meso*-Beta Fused Porphyrin Dimers. *J. Porphyr. Phthalocyanines* **2013**, *17* (4), 247–251.

(158) Dimé, A. K. D.; Devillers, C. H.; Cattey, H.; Lucas, D. Versatile Redox Reactivity of Triaryl-*Meso*-Substituted Ni(II) Porphyrin. *Dalton Trans.* **2014**, *43* (39), 14554–14564.

(159) Feng, C.-M.; Zhu, Y.-Z.; Zhang, S.-C.; Zang, Y.; Zheng, J.-Y. Synthesis of Directly Fused Porphyrin Dimers through Fe(OTf)₃-Mediated Oxidative Coupling. *Org. Biomol. Chem.* **2015**, *13* (9), 2566–2569.

(160) Tanaka, T.; Osuka, A. Conjugated Porphyrin Arrays: Synthesis, Properties and Applications for Functional Materials. *Chem. Soc. Rev.* **2015**, *44* (4), 943–969.

(161) Pegis, M. L.; McKeown, B. A.; Kumar, N.; Lang, K.; Wasylenko, D. J.; Zhang, X. P.; Raugei, S.; Mayer, J. M. Homogenous Electrocatalytic Oxygen Reduction

Rates Correlate with Reaction Overpotential in Acidic Organic Solutions. *ACS Cent. Sci.* **2016**, *2* (11), 850–856.

(162) Costentin, C.; Savéant, J.-M. Towards an Intelligent Design of Molecular Electrocatalysis. *Nat. Rev. Chem.* **2017**, *1*, 0087.

(163) Barry, B. A.; Babcock, G. T. Tyrosine Radicals Are Involved in the Photosynthetic Oxygen-Evolving System. *Proc. Natl. Acad. Sci. U.S.A.* **1987**, *84* (20), 7099–7103.

(164) Tommos, C.; Babcock, G. T. Proton and Hydrogen Currents in Photosynthetic Water Oxidation. *Biochim Biophys Acta* **2000**, *1458* (1), 199–219.

(165) Vogt, L.; Vinyard, D. J.; Khan, S.; Brudvig, G. W. Oxygen-Evolving Complex of Photosystem II: An Analysis of Second-Shell Residues and Hydrogen-Bonding Networks. *Curr. Opin. Chem. Biol.* **2015**, *25*, 152–158.

(166) Hammarström, L.; Wasielewski, M. R. Biomimetic Approaches to Artificial Photosynthesis. *Energy Environ. Sci.* **2011**, *4* (7), 2339.

(167) Hammes-Schiffer, S. Theoretical Perspectives on Proton-Coupled Electron Transfer Reactions. *Acc. Chem. Res.* **2001**, *34* (4), 273–281.

(168) Stubbe, J.; Nocera, D. G.; Yee, C. S.; Chang, M. C. Y. Radical Initiation in the Class I Ribonucleotide Reductase: Long-Range Proton-Coupled Electron Transfer? *Chem. Rev.* **2003**, *103* (6), 2167–2201.

(169) Agmon, N. The Grotthuss Mechanism. *Chem. Phys. Lett.* **1995**, *244* (5–6), 456–462.

(170) Bondar, A.-N.; Dau, H. Extended Protein/Water H-Bond Networks in Photosynthetic Water Oxidation. *Biochim. Biophys. Acta.* **2012**, *1817* (8), 1177–1190.

(171) Burdinski, D.; Wieghardt, K.; Steenken, S. Intramolecular Electron Transfer from Mn or Ligand Phenolate to Photochemically Generated Ru^{III} in Multinuclear Ru/Mn Complexes. Laser Flash Photolysis and EPR Studies on Photosystem II Models. *J. Am. Chem. Soc.* **1999**, *121* (46), 10781–10787.

(172) Sjödin, M.; Styring, S.; Åkermark, B.; Sun, L.; Hammarström, L. Proton-Coupled Electron Transfer from Tyrosine in a Tyrosine-Ruthenium-Tris-Bipyridine Complex: Comparison with Tyrosine$_z$ Oxidation in Photosystem II. *J. Am. Chem. Soc.* **2000**, *122* (16), 3932–3936.

(173) Maki, T.; Araki, Y.; Ishida, Y.; Onomura, O.; Matsumura, Y. Construction of Persistent Phenoxyl Radical with Intramolecular Hydrogen Bonding. *J. Am. Chem. Soc.* **2001**, *123* (14), 3371–3372.

(174) Benisvy, L.; Bill, E.; Blake, A. J.; Collison, D.; Davies, E. S.; Garner, C. D.; Guindy, C. I.; McInnes, E. J. L.; McArdle, G.; McMaster, J.; Wilson, C.; Wolowska, J. Phenolate and Phenoxyl Radical Complexes of Co(II) and Co(III). *Dalton Trans.* **2004**, No. 21, 3647–3653.

(175) Rhile, I. J.; Mayer, J. M. One-Electron Oxidation of a Hydrogen-Bonded Phenol Occurs by Concerted Proton-Coupled Electron Transfer. *J. Am. Chem. Soc.* **2004**, *126* (40), 12718–12719.

(176) Lachaud, F.; Quaranta, A.; Pellegrin, Y.; Dorlet, P.; Charlot, M. F.; Un, S.; Leibl, W.; Aukaulo, A. A Biomimetic Model of the Electron Transfer between P$_{680}$ and the TyrZ-His190 Pair of PSII. *Angew. Chem. Int. Ed.* **2005**, *44* (10), 1536–1540.

(177) Costentin, C.; Robert, M.; Savéant, J.-M. Electrochemical and Homogeneous Proton-Coupled Electron Transfers: Concerted Pathways in the One-Electron Oxidation of a Phenol Coupled with an Intramolecular Amine-Driven Proton Transfer. *J. Am. Chem. Soc.* **2006**, *128* (14), 4552–4553.

(178) Rhile, I. J.; Markle, T. F.; Nagao, H.; DiPasquale, A. G.; Lam, O. P.; Lockwood, M. A.; Rotter, K.; Mayer, J. M. Concerted Proton-Electron Transfer in the Oxidation of Hydrogen-Bonded Phenols. *J. Am. Chem. Soc.* **2006**, *128* (18), 6075–6088.

(179) Lomoth, R.; Magnuson, A.; Sjödin, M.; Huang, P.; Styring, S.; Hammarström, L. Mimicking the Electron Donor Side of Photosystem II in Artificial Photosynthesis. *Photosynth. Res.* **2006**, *87*, 25–40.

(180) Costentin, C.; Louault, C.; Robert, M.; Savéant, J.-M. Evidence for Concerted Proton-Electron Transfer in the Electrochemical Oxidation of Phenols with Water as Proton Acceptor. Tri-*Tert*-Butylphenol. *J. Am. Chem. Soc.* **2008**, *130* (47), 15817–15819.

(181) Moore, G. F.; Hambourger, M.; Kodis, G.; Michl, W.; Gust, D.; Moore, T. A.; Moore, A. L. Effects of Protonation State on a Tyrosine-Histidine Bioinspired Redox Mediator. *J. Phys. Chem. B* **2010**, *114* (45), 14450–14457.

(182) Megiatto, J. D.; Antoniuk-Pablant, A.; Sherman, B. D.; Kodis, G.; Gervaldo, M.; Moore, T. A.; Moore, A. L.; Gust, D. Mimicking the Electron Transfer Chain in Photosystem II with a Molecular Triad Thermodynamically Capable of Water Oxidation. *Proc. Natl. Acad. Sci. U.S.A.* **2012**, *109* (39), 15578–15583.

(183) Megiatto, J. D.; Méndez-Hernández, D. D.; Tejeda-Ferrari, M. E.; Teillout, A.-L.; Llansola-Portolés, M. J.; Kodis, G.; Poluektov, O. G.; Rajh, T.; Mujica, V.; Groy, T. L.; Gust, D.; Moore, T. A.; Moore, A. L. A Bioinspired Redox Relay That Mimics Radical Interactions of the Tyr–His Pairs of Photosystem II. *Nat. Chem.* **2014**, *6*, 423–428.

(184) Ravensbergen, J.; Antoniuk-Pablant, A.; Sherman, B. D.; Kodis, G.; Megiatto, J. D.; Méndez-Hernández, D. D.; Frese, R. N.; Van Grondelle, R.; Moore, T. A.; Moore, A. L.; Gust, D.; Kennis, J. T. M. Spectroscopic Analysis of a Biomimetic Model of Tyr$_Z$ Function in PSII. *J. Phys. Chem. B* **2015**, *119* (37), 12156–12163.

(185) Odella, E.; Mora, S. J.; Wadsworth, B. L.; Huynh, M. T.; Goings, J. J.; Liddell, P. A.; Groy, T. L.; Gervaldo, M.; Sereno, L. E.; Gust, D.; Moore, T. A.; Moore, G. F.; Hammes-Schiffer, S.; Moore, A. L. Controlling Proton-Coupled Electron Transfer in Bioinspired Artificial Photosynthetic Relays. *J. Am. Chem. Soc.* **2018**, *140* (45), 15450–15460.

(186) Mora, S. J.; Heredia, D. A.; Odella, E.; Vrudhula, U.; Gust, D.; Moore, T. A.; Moore, A. L. Design and Synthesis of Benzimidazole Phenol-Porphyrin Dyads for the Study of Bioinspired Photoinduced Proton-Coupled Electron Transfer. *J. Porphyr. Phthalocyanines* **2019**, *23* (11n12), 1336–1345.

(187) Odella, E.; Wadsworth, B. L.; Mora, S. J.; Goings, J. J.; Huynh, M. T.; Gust, D.; Moore, T. A.; Moore, G. F.; Hammes-Schiffer, S.; Moore, A. L. Proton-Coupled Electron Transfer Drives Long-Range Proton Translocation in Bioinspired Systems. *J. Am. Chem. Soc.* **2019**, *141* (36), 14057–14061.

(188) Parada, G. A.; Goldsmith, Z. K.; Kolmar, S.; Pettersson Rimgard, B.; Mercado, B. Q.; Hammarström, L.; Hammes-Schiffer, S.; Mayer, J. M. Concerted Proton-Electron Transfer Reactions in the Marcus Inverted Region. *Science* **2019**, *364* (6439), 471–475.

(189) Wang, D.; Sampaio, R. N.; Troian-Gautier, L.; Marquard, S. L.; Farnum, B. H.; Sherman, B. D.; Sheridan, M. V.; Dares, C. J.; Meyer, G. J.; Meyer, T. J. Molecular Photoelectrode for Water Oxidation Inspired by Photosystem II. *J. Am. Chem. Soc.* **2019**, *141* (19), 7926–7933.

(190) Odella, E.; Mora, S. J.; Wadsworth, B. L.; Goings, J. J.; Gervaldo, M. A.; Sereno, L. E.; Groy, T. L.; Gust, D.; Moore, T. A.; Moore, G. F.; Hammes-Schiffer, S.; Moore, A. L. Proton-Coupled Electron Transfer across Benzimidazole Bridges in Bioinspired Proton Wires. *Chem. Sci.* **2020**, *11* (15), 3820–3828.

(191) Guerra, W. D.; Odella, E.; Secor, M.; Goings, J. J.; Urrutia, M. N.; Wadsworth, B. L.; Gervaldo, M.; Sereno, L. E.; Moore, T. A.; Moore, G. F.; Hammes-Schiffer,

S.; Moore, A. L. Role of Intact Hydrogen-Bond Networks in Multiproton-Coupled Electron Transfer. *J. Am. Chem. Soc.* **2020**, *142* (52), 21842–21851.

(192) Yoneda, Y.; Mora, S. J.; Shee, J.; Wadsworth, B. L.; Arsenault, E. A.; Hait, D.; Kodis, G.; Gust, D.; Moore, G. F.; Moore, A. L.; Head-Gordon, M.; Moore, T. A.; Fleming, G. R. Electron-Nuclear Dynamics Accompanying Proton-Coupled Electron Transfer. *J. Am. Chem. Soc.* **2021**, *143* (8), 3104–3112.

(193) Sayre, H.; Ripberger, H. H.; Odella, E.; Zieleniewska, A.; Heredia, D. A.; Rumbles, G.; Scholes, G. D.; Moore, T. A.; Moore, A. L.; Knowles, R. R. PCET-Based Ligand Limits Charge Recombination with an Ir(III) Photoredox Catalyst. *J. Am. Chem. Soc.* **2021**, *143* (33), 13034–13043.

(194) Odella, E.; Secor, M.; Elliott, M.; Groy, T. L.; Moore, T. A.; Hammes-Schiffer, S.; Moore, A. L. Multi PCET in Symmetrically Substituted Benzimidazoles. *Chem. Sci.* **2021**, *12* (38), 12667–12675.

(195) Guerra, W. D.; Odella, E.; Urrutia, M. N.; Liddell, P. A.; Moore, T. A.; Moore, A. L. Models to Study Photoinduced Multiple Proton Coupled Electron Transfer Processes. *J. Porphyr. Phthalocyanines* **2021**, *25* (07n08), 674–682.

(196) Huynh, M. T.; Mora, S. J.; Villalba, M.; Tejeda-Ferrari, M. E.; Liddell, P. A.; Cherry, B. R.; Teillout, A.-L.; Machan, C. W.; Kubiak, C. P.; Gust, D.; Moore, T. A.; Hammes-Schiffer, S.; Moore, A. L. Concerted One-Electron Two-Proton Transfer Processes in Models Inspired by the Tyr-His Couple of Photosystem II. *ACS Cent. Sci.* **2017**, *3* (5), 372–380.

(197) Zhang, W.; Lai, W.; Cao, R. Energy-Related Small Molecule Activation Reactions: Oxygen Reduction and Hydrogen and Oxygen Evolution Reactions Catalyzed by Porphyrin- and Corrole-Based Systems. *Chem. Rev.* **2017**, *117* (4), 3717–3797.

(198) Beyene, B. B.; Hung, C.-H. Recent Progress on Metalloporphyrin-Based Hydrogen Evolution Catalysis. *Coord. Chem. Rev.* **2020**, *410*, 213234.

(199) Gotico, P.; Halime, Z.; Aukauloo, A. Recent Advances in Metalloporphyrin-Based Catalyst Design towards Carbon Dioxide Reduction: From Bio-Inspired Second Coordination Sphere Modifications to Hierarchical Architectures. *Dalton Trans.* **2020**, *49* (8), 2381–2396.

(200) Costentin, C.; Limoges, B.; Robert, M.; Tard, C. A Pioneering Career in Electrochemistry: Jean-Michel Saveánt. *ACS Catal.* **2021**, *11* (6), 3224–3238.

(201) Hammouche, M.; Lexa, D.; Momenteau, M.; Savêant, J.-M. Chemical Catalysis of Electrochemical Reactions. Homogeneous Catalysis of the Electrochemical

Reduction of Carbon Dioxide by Iron("0") Porphyrins. Role of the Addition of Magnesium Cations. *J. Am. Chem. Soc.* **1991**, *113* (22), 8455–8466.

(202)   Bhugun, I.; Lexa, D.; Savéant, J.-M. Ultraefficient Selective Homogenous Catalysis of the Electrochemical Reduction of Carbon Dioxide by an Iron(0) Porphyrin Associated with a Weak Bronsted Acid Cocatalyst. *J. Am. Chem. Soc.* **1994**, *116* (11), 5015–5016.

(203)   Bhugun, I.; Lexa, D.; Savéant, J.-M. Catalysis of the Electrochemical Reduction of Carbon Dioxide by Iron(0) Porphyrins: Synergystic Effect of Weak Brönsted Acids. *J. Am. Chem. Soc.* **1996**, *118* (7), 1769–1776.

(204)   Bhugun, I.; Lexa, D.; Savéant, J.-M. Catalysis of the Electrochemical Reduction of Carbon Dioxide by Iron(0) Porphyrins. Synergistic Effect of Lewis Acid Cations. *J. Phys. Chem.* **1996**, *100* (51), 19981–19985.

(205)   Costentin, C.; Drouet, S.; Robert, M.; Savéant, J.-M. Turnover Numbers, Turnover Frequencies, and Overpotential in Molecular Catalysis of Electrochemical Reactions. Cyclic Voltammetry and Preparative-Scale Electrolysis. *J. Am. Chem. Soc.* **2012**, *134* (27), 11235–11242.

(206)   Costentin, C.; Drouet, S.; Passard, G.; Robert, M.; Savéant, J.-M. Proton-Coupled Electron Transfer Cleavage of Heavy-Atom Bonds in Electrocatalytic Processes. Cleavage of a C-O Bond in the Catalyzed Electrochemical Reduction of CO_2. *J. Am. Chem. Soc.* **2013**, *135* (24), 9023–9031.

(207)   Costentin, C.; Dridi, H.; Savéant, J.-M. Molecular Catalysis of H_2 Evolution: Diagnosing Heterolytic versus Homolytic Pathways. *J. Am. Chem. Soc.* **2014**, *136* (39), 13727–13734.

(208)   Costentin, C.; Passard, G.; Robert, M.; Savéant, J.-M. Pendant Acid-Base Groups in Molecular Catalysts: H-Bond Promoters or Proton Relays? Mechanisms of the Conversion of CO_2 to CO by Electrogenerated Iron(0)Porphyrins Bearing Prepositioned Phenol Functionalities. *J. Am. Chem. Soc.* **2014**, *136* (33), 11821–11829.

(209)   Costentin, C.; Robert, M.; Savéant, J.-M.; Tatin, A. Efficient and Selective Molecular Catalyst for the CO_2-to-CO Electrochemical Conversion in Water. *Proc. Natl. Acad. Sci. U.S.A.* **2015**, *112* (22), 6882–6886.

(210)   Costentin, C.; Passard, G.; Robert, M.; Savéant, J.-M. Ultraefficient Homogeneous Catalyst for the CO_2-to-CO Electrochemical Conversion. *Proc. Natl. Acad. Sci. U.S.A.* **2014**, *111* (42), 14990–14994.

(211) Costentin, C.; Savéant, J.-M. Multielectron, Multistep Molecular Catalysis of Electrochemical Reactions: Benchmarking of Homogeneous Catalysts. *ChemElectroChem* **2014**, *1* (7), 1226–1236.

(212) Costentin, C.; Savéant, J.-M. Heterogeneous Molecular Catalysis of Electrochemical Reactions: Volcano Plots and Catalytic Tafel Plots. *ACS Appl. Mater. Interfaces* **2017**, *9* (23), 19894–19899.

(213) Artero, V.; Savéant, J.-M. Toward the Rational Benchmarking of Homogeneous H_2-Evolving Catalysts. *Energy Environ. Sci.* **2014**, *7* (11), 3808–3814.

(214) Sugiura, K.; Matsumoto, T.; Ohkouchi, S.; Naitoh, Y.; Kawai, T.; Takai, Y.; Ushiroda, K.; Sakata, Y. Synthesis of the Porphyrin-Fused Porphyrin, [2]Porphyracene. *Chem. Commun.* **1999**, No. 19, 1957–1958.

(215) Khusnutdinova, D.; Wadsworth, B. L.; Flores, M.; Beiler, A. M.; Reyes Cruz, E. A.; Zenkov, Y.; Moore, G. F. Electrocatalytic Properties of Binuclear Cu(II) Fused Porphyrins for Hydrogen Evolution. *ACS Catal.* **2018**, *8* (10), 9888–9898.

(216) Huerta-Flores, A. M.; Bengasi, G.; Baba, K.; Boscher, N. D. Fused Porphyrin Thin Films as Heterogeneous Visible-Light Active Photocatalysts with Well-Defined Active Metal Sites for Hydrogen Generation. *ACS Appl. Energy Mater.* **2020**, *3* (10), 9848–9855.

(217) Liu, H.; Yu, C.; Gao, N.; Zhao, J. The Diversity of Electron-Transport Behaviors of Molecular Junctions: Correlation with the Electron-Transport Pathway. *ChemPhysChem* **2010**, *11* (9), 1895–1902.

(218) Lysenko, A. B.; Thamyongkit, P.; Schmidt, I.; Diers, J. R.; Bocian, D. F.; Lindsey, J. S. Diverse Porphyrin Dimers as Candidates for High-Density Charge-Storage Molecules. *J. Porphyr. Phthalocyanines* **2006**, *10* (1), 22–32.

(219) Tsuda, A.; Nakano, A.; Furuta, H.; Yamochi, H.; Osuka, A. Doubly *Meso*-β-Linked Diporphyrins from Oxidation of 5,10,15-Triaryl-Substituted Ni^{II}-and Pd^{II}-Porphyrins. *Angew. Chem. Int. Ed.* **2000**, *39* (3), 558–561.

(220) Ouyang, Q.; Zhu, Y.-Z.; Zhang, C.-H.; Yan, K.-Q.; Li, Y.-C.; Zheng, J.-Y. An Efficient PIFA-Mediated Synthesis of Fused Diporphyrin and Triply-Singly Interlacedly Linked Porphyrin Array. *Org. Lett.* **2009**, *11* (22), 5266–5269.

(221) Feng, C.-M.; Zhu, Y.-Z.; Zang, Y.; Tong, Y.-Z.; Zheng, J.-Y. Switchable Regioselectivity in the PIFA-BF_3·Et_2O Mediated Oxidative Coupling of *Meso*-Brominated Ni(II) Porphyrin. *Org. Biomol. Chem.* **2014**, *12* (36), 6990–6993.

(222) Osuka, A. Compound Having 2 To 4 Porphyrins Doubly Bonded (Condensed) By Each Meso-Beta Carbon-Carbon. JPA 2001-089490, 2001.

(223) Tsuda, A.; Furuta, H.; Osuka, A. Syntheses, Structural Characterizations, and Optical and Electrochemical Properties of Directly Fused Diporphyrins. *J. Am. Chem. Soc.* **2001**, *123* (42), 10304–10321.

(224) Tsuda, A.; Nakamura, Y.; Osuka, A. Synthesis of *Meso-β* Doubly Linked Porphyrin Tapes. *Chem. Commun.* **2003**, No. 9, 1096–1097.

(225) Kamo, M.; Tsuda, A.; Nakamura, Y.; Aratani, N.; Furukawa, K.; Kato, T.; Osuka, A. Metal-Dependent Regioselective Oxidative Coupling of 5,10,15-Triarylporphyrins with DDQ-Sc(OTf)$_3$ and Formation of an Oxo-Quinoidal Porphyrin. *Org. Lett.* **2003**, *5* (12), 2079–2082.

(226) Muranaka, A.; Yokoyama, M.; Matsumoto, Y.; Uchiyama, M.; Tsuda, A.; Osuka, A.; Kobayashi, N. Magnetic Circular Dichroism Study of Directly Fused Porphyrins. *ChemPhysChem* **2005**, *6* (1), 171–179.

(227) Kim, D. Y.; Ahn, T. K.; Kwon, J. H.; Kim, D.; Ikeue, T.; Aratani, N.; Osuka, A.; Shigeiwa, M.; Maeda, S. Large Two-Photon Absorption (TPA) Cross-Section of Directly Linked Fused Diporphyrins. *J. Phys. Chem. A* **2005**, *109* (13), 2996–2999.

(228) Sahoo, A. K.; Nakamura, Y.; Aratani, N.; Kim, K. S.; Noh, S. B.; Shinokubo, H.; Kim, D.; Osuka, A. Synthesis of Brominated Directly Fused Diporphyrins through Gold(III)-Mediated Oxidation. *Org. Lett.* **2006**, *8* (18), 4141–4144.

(229) Yoon, M.-C.; Noh, S. B.; Tsuda, A.; Nakamura, Y.; Osuka, A.; Kim, D. Photophysics of *Meso-β* Doubly Linked Ni(II) Porphyrin Arrays: Large Two-Photon Absorption Cross-Section and Fast Energy Relaxation Dynamics. *J. Am. Chem. Soc.* **2007**, *129* (33), 10080–10081.

(230) Brennan, B. J.; Kenney, M. J.; Liddell, P. A.; Cherry, B. R.; Li, J.; Moore, A. L.; Moore, T. A.; Gust, D. Oxidative Coupling of Porphyrins Using Copper(II) Salts. *Chem. Commun.* **2011**, *47* (36), 10034–10036.

(231) Ikeue, T.; Furukawa, K.; Hata, H.; Aratani, N.; Shinokubo, H.; Kato, T.; Osuka, A. The Importance of a β-β Bond for Long-Range Antiferromagnetic Coupling in Directly Linked Copper(II) and Silver(II) Diporphyrins. *Angew. Chem. Int. Ed.* **2005**, *44* (42), 6899–6901.

(232) Fendt, L.-A.; Fang, H.; Plonska-Brzezinska, M. E.; Zhang, S.; Cheng, F.; Braun, C.; Echegoyen, L.; Diederich, F. Meso,Meso-Linked and Triply Fused

Diporphyrins with Mixed-Metal Ions: Synthesis and Electrochemical Investigations. *Eur. J. Org. Chem.* **2007**, *2007* (28), 4659–4673.

(233) Cho, H. S.; Jeong, D. H.; Cho, S.; Kim, D.; Matsuzaki, Y.; Tanaka, K.; Tsuda, A.; Osuka, A. Photophysical Properties of Porphyrin Tapes. *J. Am. Chem. Soc.* **2002**, *124* (49), 14642–14654.

(234) Tsuda, A.; Osuka, A. Discrete Conjugated Porphyrin Tapes with an Exceptionally Small Bandgap. *Adv. Mater.* **2002**, *14* (1), 75–79.

(235) Nakamura, Y.; Aratani, N.; Tsuda, A.; Osuka, A.; Furukawa, K.; Kato, T. Oxidative Direct Coupling of Metalloporphyrins. *J. Porphyr. Phthalocyanines* **2003**, *7* (4), 264–269.

(236) Nalin De Silva, K. M. Meso-β Doubly Linked and Meso-Meso, β-β, β-β Triply Linked Oligoporphyrin Molecular Tapes as Potential Non Linear Optical (NLO) Materials: Quantum Chemical Calculations. *J. Mol. Struct.: THEOCHEM.* **2005**, *726* (1–3), 39–45.

(237) Zhang, X.-B.; Feng, J.-K.; Ren, A.-M.; Sun, C.-C. A Comparative Study of One- and Two-Photon Absorption Properties of *Meso-Meso* Singly, *Meso*-β Doubly and *Meso-Meso* β-β β-β Triply Linked Zn^{II}-Porphyrin Oligomers. *J. Mol. Struct.: THEOCHEM.* **2007**, *804* (1–3), 21–29.

(238) Ikeda, T.; Aratani, N.; Easwaramoorthi, S.; Kim, D.; Osuka, A. Meso-*β* Doubly Linked Zn(II) Porphyrin Trimers: Distinct *Anti*-versus-*Syn* Effects on Their Photophysical Properties. *Org. Lett.* **2009**, *11* (14), 3080–3083.

(239) Heo, J. H.; Ikeda, T.; Lim, J. M.; Aratani, N.; Osuka, A.; Kim, D. Molecular-Shape-Dependent Photophysical Properties of *Meso-β* Doubly Linked Zn(II) Porphyrin Arrays and Their Indene-Fused Analogues. *J. Phys. Chem. B* **2010**, *114* (45), 14528–14536.

(240) Mai, C.-L.; Huang, W.-K.; Lu, H.-P.; Lee, C.-W.; Chiu, C.-L.; Liang, Y.-R.; Diau, E. W.-G.; Yeh, C.-Y. Synthesis and Characterization of Diporphyrin Sensitizers for Dye-Sensitized Solar Cells. *Chem. Commun.* **2010**, *46* (5), 809–811.

(241) Diev, V. V.; Hanson, K.; Zimmerman, J. D.; Forrest, S. R.; Thompson, M. E. Fused Pyrene-Diporphyrins: Shifting Near-Infrared Absorption to 1.5 μm and Beyond. *Angew. Chem. Int. Ed.* **2010**, *49* (32), 5523–5526.

(242) Tokita, Y.; Suzuki, Y.; Morooka, M.; Noda, K. Dye Sensitized Photoelectric Conversion Device. JPA 2005-276410, 2005.

(243) Lee, S.; Yamashita, K.; Sakata, N.; Hirao, Y.; Ogawa, K.; Ogawa, T. Stable Singlet Biradicals of Rare-Earth-Fused Diporphyrin-Triple-Decker Complexes with Low Energy Gaps and Multi-Redox States. *Chem. Eur. J.* **2019**, *25* (13), 3240–3243.

(244) Boucher, L. J.; Katz, J. J. The Infrared Spectra of Metalloporphyrins (4000-160 Cm^{-1}). *J. Am. Chem. Soc.* **1967**, *89* (6), 1340–1345.

(245) Alben, J. O.; Choi, S. S.; Adler, A. D.; Caughey, W. S. Infrared Spectroscopy of Porphyrins. *Ann. N. Y. Acad. Sci.* **1973**, *206* (1), 278–295.

(246) Bar-Ilan, A.; Manassen, J. Heterogeneous and Homogeneous Catalysis by Substituted Cobalt Tetraphenylporphyrins, and Correlations with IR Spectra. *J. Catal.* **1974**, *33* (1), 68–73.

(247) Kincaid, J.; Nakamoto, K. Vibrational Spectra of Transition Metal Complexes of Tetraphenylporphine. *J. Inorg. Nucl. Chem.* **1975**, *37* (1), 85–89.

(248) Khusnutdinova, D.; Beiler, A. M.; Wadsworth, B. L.; Nanyangwe, S. K.; Moore, G. F. Vibrational Structure Analysis of Cobalt Fluoro-Porphyrin Surface Coatings on Gallium Phosphide. *J. Porphyr. Phthalocyanines* **2018**, *22* (6), 461–468.

(249) Khusnutdinova, D.; Flores, M.; Beiler, A. M.; Moore, G. F. Synthesis and Characterization of a Cobalt(II) Tetrakis(3-Fluorophenyl) Porphyrin with a Built-in 4-Vinylphenyl Surface Attachment Moiety. *Photosynthetica* **2018**, *56* (1), 67–74.

(250) Wadsworth, B. L.; Khusnutdinova, D.; Urbine, J. M.; Reyes, A. S.; Moore, G. F. Expanding the Redox Range of Surface-Immobilized Metallocomplexes Using Molecular Interfaces. *ACS Appl. Mater. Interfaces* **2020**, *12* (3), 3903–3911.

(251) Römelt, C.; Song, J.; Tarrago, M.; Rees, J. A.; Van Gastel, M.; Weyhermüller, T.; Debeer, S.; Bill, E.; Neese, F.; Ye, S. Electronic Structure of a Formal Iron(0) Porphyrin Complex Relevant to CO$_2$ Reduction. *Inorg. Chem.* **2017**, *56* (8), 4745–4750.

(252) Westre, T. E.; Kennepohl, P.; DeWitt, J. G.; Hedman, B.; Hodgson, K. O.; Solomon, E. I. A Multiplet Analysis of Fe K-Edge 1s → 3d Pre-Edge Features of Iron Complexes. *J. Am. Chem. Soc.* **1997**, *119* (27), 6297–6314.

(253) Lexa, D.; Momenteau, M.; Rentien, P.; Rytz, G.; Savéant, J.-M.; Xu, F. Molecular Environment Effects in Redox Chemistry. Electrochemistry of Ether-Linked Basket-Handle and Amine-Linked Basket-Handle and Picket-Fence Iron Porphyrins. *J. Am. Chem. Soc.* **1984**, *106* (17), 4755–1765.

(254) Mashiko, T.; Reed, C. A.; Scheidt, W. R. Nature of Iron (I) and Iron (0) Tetraphenylporphyrin Complexes. Synthesis and Molecular Structure of (Dibenzo-18-Crown-6)Bis(Tetrahydrofuran)Sodium (*Meso-*Tetraphenylporphinato)Ferrate and Bis[Tris(Tetrahydrofuran)Sodium] (*Meso-*Tetraphenylporphinato)Ferrate. *Inorg. Chem.* **1984**, *23* (20), 3192–3196.

(255) Trasatti, S. The Absolute Electrode Potential: An Explanatory Note. *J. Electroanal. Chem.* **1986**, *209*, 417–428.

(256) Lexa, D.; Mispelter, J.; Savéant, J.-M. Electroreductive Alkylation of Iron in Porphyrin Complexes. Electrochemical and Spectral Characteristics of σ-Alkyliron Porphyrins. *J. Am. Chem. Soc.* **1981**, *103* (23), 6806–6812.

(257) Lexa, D.; Savéant, J.-M.; Wang, D. L. Electroreductive Alkylation of Iron Porphyrins. Iron(III), Iron(II), and Iron(I) Alkyl Complexes from the Reaction of Doubly Reduced Iron(II) Porphyrins with Alkyl Halides. *Organometallics* **1986**, *5* (7), 1428–1434.

(258) Kadish, K. M.; Van Caemelbecke, E. Electrochemistry of Porphyrins and Related Macrocycles. . *J. Solid State Chem.* **2003**, *7* (5), 254–258.

(259) Sun, H.; Smirnov, V. V.; DiMagno, S. G. Slow Electron Transfer Rates for Fluorinated Cobalt Porphyrins: Electronic and Conformational Factors Modulating Metalloporphyrin ET. *Inorg. Chem.* **2003**, *42* (19), 6032–6040.

(260) Lyaskovskyy, V.; De Bruin, B. Redox Non-Innocent Ligands: Versatile New Tools to Control Catalytic Reactions. *ACS Catal.* **2012**, *2* (2), 270–279.

(261) Luca, O. R.; Crabtree, R. H. Redox-Active Ligands in Catalysis. *Chem. Soc. Rev.* **2013**, *42* (4), 1440–1459.

(262) Wu, Y.; Jiang, J.; Weng, Z.; Wang, M.; Broere, D. L. J.; Zhong, Y.; Brudvig, G. W.; Feng, Z.; Wang, H. Electroreduction of CO_2 Catalyzed by a Heterogenized Zn-Porphyrin Complex with a Redox-Innocent Metal Center. *ACS Cent. Sci.* **2017**, *3* (8), 847–852.

(263) Migliore, A.; Polizzi, N. F.; Therien, M. J.; Beratan, D. N. Biochemistry and Theory of Proton-Coupled Electron Transfer. *Chem. Rev.* **2014**, *114* (7), 3381–3465.

(264) Hammes-Schiffer, S.; Soudackov, A. V. Proton-Coupled Electron Transfer in Solution, Proteins, and Electrochemistry. *J. Phys. Chem. B* **2008**, *112* (45), 14108–14123.

(265) Cukierman, S. Et Tu, Grotthuss! And Other Unfinished Stories. *Biochim. Biophys. Acta* **2006**, *1757* (8), 876–885.

(266) Pavošević, F.; Culpitt, T.; Hammes-Schiffer, S. Multicomponent Quantum Chemistry: Integrating Electronic and Nuclear Quantum Effects via the Nuclear-Electronic Orbital Method. *Chem. Rev.* **2020**, *120* (9), 4222–4253.

(267) Barry, B. A. Reaction Dynamics and Proton Coupled Electron Transfer: Studies of Tyrosine-Based Charge Transfer in Natural and Biomimetic Systems. *Biochim. Biophys. Acta* **2015**, *1847* (1), 46–54.

(268) Meyer, T. J.; Huynh, M. H. V.; Thorp, H. H. The Possible Role of Proton-Coupled Electron Transfer (PCET) in Water Oxidation by Photosystem II. *Angew. Chem. Int. Ed.* **2007**, *46* (28), 5284–5304.

(269) Reece, S. Y.; Nocera, D. G. Proton-Coupled Electron Transfer in Biology: Results from Synergistic Studies in Natural and Model Systems. *Annu. Rev. Biochem.* **2009**, *78*, 673–699.

(270) Nagao, R.; Ueoka-Nakanishi, H.; Noguchi, T. D1-Asn-298 in Photosystem II Is Involved in a Hydrogen-Bond Network near the Redox-Active Tyrosine YZ for Proton Exit during Water Oxidation. *J. Biol. Chem.* **2017**, *292* (49), 20046–20057.

(271) Kawashima, K.; Saito, K.; Ishikita, H. Mechanism of Radical Formation in the H-Bond Network of D1-Asn298 in Photosystem II. *Biochemistry* **2018**, *57* (33), 4997–5004.

(272) Vinyard, D. J.; Brudvig, G. W. Progress Toward a Molecular Mechanism of Water Oxidation in Photosystem II. *Annu. Rev. Phys. Chem.* **2017**, *68*, 101–116.

(273) Saito, K.; Rutherford, A. W.; Ishikita, H. Energetics of Proton Release on the First Oxidation Step in the Water-Oxidizing Enzyme. *Nat. Commun.* **2015**, *6*, 8488.

(274) Long, S. P.; Marshall-Colon, A.; Zhu, X.-G. Meeting the Global Food Demand of the Future by Engineering Crop Photosynthesis and Yield Potential. *Cell* **2015**, *161* (1), 56–66.

(275) Ort, D. R.; Merchant, S. S.; Alric, J.; Barkan, A.; Blankenship, R. E.; Bock, R.; Croce, R.; Hanson, M. R.; Hibberd, J. M.; Long, S. P.; Moore, T. A.; Moroney, J.; Niyogi, K. K.; Parry, M. A. J.; Peralta-Yahya, P. P.; Prince, R. C.; Redding, K. E.; Spalding, M. H.; Van Wijk, K. J.; Vermaas, W. F. J.; Von Caemmerer, S.; Weber, A. P. M.; Yeates, T. O.; Yuan, J. S.; Zhu, X. G. Redesigning Photosynthesis to Sustainably Meet Global Food and Bioenergy Demand. *Proc. Natl. Acad. Sci. U.S.A.* **2015**, *112* (28), 8529–8536.

(276) Sayre, H. J.; Tian, L.; Son, M.; Hart, S. M.; Liu, X.; Arias-Rotondo, D. M.; Rand, B. P.; Schlau-Cohen, G. S.; Scholes, G. D. Solar Fuels and Feedstocks: The Quest for Renewable Black Gold. *Energy Environ. Sci.* **2021**, *14* (3), 1402–1419.

(277) Wu, X.; Hong, J. J.; Shin, W.; Ma, L.; Liu, T.; Bi, X.; Yuan, Y.; Qi, Y.; Surta, T. W.; Huang, W.; Neuefeind, J.; Wu, T.; Greaney, P. A.; Lu, J.; Ji, X. Diffusion-Free Grotthuss Topochemistry for High-Rate and Long-Life Proton Batteries. *Nat. Energy* **2019**, *4* (2), 123–130.

(278) Arsenault, E. A.; Bhattacharyya, P.; Yoneda, Y.; Fleming, G. R. Two-Dimensional Electronic-Vibrational Spectroscopy: Exploring the Interplay of Electrons and Nuclei in Excited State Molecular Dynamics. *J. Chem. Phys.* **2021**, *155* (2), 020901.

(279) Oliver, T. A. A.; Lewis, N. H. C.; Fleming, G. R. Correlating the Motion of Electrons and Nuclei with Two-Dimensional Electronic-Vibrational Spectroscopy. *Proc. Natl. Acad. Sci. U.S.A.* **2014**, *111* (28), 10061–10066.

(280) Goings, J. J.; Hammes-Schiffer, S. Nonequilibrium Dynamics of Proton-Coupled Electron Transfer in Proton Wires: Concerted but Asynchronous Mechanisms. *ACS Cent. Sci.* **2020**, *6* (9), 1594–1601.

(281) Cook, D. Vibrational Spectra Of Pyridinium Salts. *Can. J. Chem.* **1961**, *39* (10), 2009–2024.

(282) Glazunov, V. P.; Odinokov, S. E. Infrared Spectra of Pyridinium Salts in Solution - I. The Region of Middle Frequencies. *Spectrochim. Acta A* **1982**, *38* (4), 399–408.

(283) Cho, M.; Fleming, G. R. Two-Dimensional Electronic-Vibrational Spectroscopy Reveals Cross-Correlation between Solvation Dynamics and Vibrational Spectral Diffusion. *J. Phys. Chem. B* **2020**, *124* (49), 11222–11235.

(284) Arsenault, E. A.; Yoneda, Y.; Iwai, M.; Niyogi, K. K.; Fleming, G. R. Vibronic Mixing Enables Ultrafast Energy Flow in Light-Harvesting Complex II. *Nat. Commun.* **2020**, *11*, 1460.

(285) Wu, E. C.; Ge, Q.; Arsenault, E. A.; Lewis, N. H. C.; Gruenke, N. L.; Head-Gordon, M. J.; Fleming, G. R. Two-Dimensional Electronic-Vibrational Spectroscopic Study of Conical Intersection Dynamics: An Experimental and Electronic Structure Study. *Phys. Chem. Chem. Phys.* **2019**, *21* (26), 14153–14163.

(286) Roy, P. P.; Shee, J.; Arsenault, E. A.; Yoneda, Y.; Feuling, K.; Head-Gordon, M.; Fleming, G. R. Solvent Mediated Excited State Proton Transfer in Indigo Carmine. *J. Phys. Chem. Lett.* **2020**, *11* (10), 4156–4162.

(287) Arsenault, E. A.; Yoneda, Y.; Iwai, M.; Niyogi, K. K.; Fleming, G. R. The Role of Mixed Vibronic Q_y-Q_x States in Green Light Absorption of Light-Harvesting Complex II. *Nat. Commun.* **2020**, *11*, 6011.

(288) Hoganson, C. W.; Babcock, G. T. A Metalloradical Mechanism for the Generation of Oxygen from Water in Photosynthesis. *Science* **1997**, *277* (5334), 1953–1956.

(289) Faller, P.; Goussias, C.; Rutherford, A. W.; Un, S. Resolving Intermediates in Biological Proton-Coupled Electron Transfer: A Tyrosyl Radical Prior to Proton Movement. *Proc. Natl. Acad. Sci. U.S.A.* **2003**, *100* (15), 8732–8735.

(290) Markle, T. F.; Rhile, I. J.; DiPasquale, A. G.; Mayer, J. M. Probing Concerted Proton-Electron Transfer in Phenol-Imidazoles. *Proc. Natl. Acad. Sci. U.S.A.* **2008**, *105* (24), 8185–8190.

(291) Glazunov, V. P.; Odinokov, S. E. Infrared Spectra of Pyridinium Salts in Solution - II. Fermi Resonance and Structure of ν_{NH} Bands. *Spectrochim. Acta A* **1982**, *38* (4), 409–415.

(292) Odella, E.; Moore, T. A.; Moore, A. L. Tuning the Redox Potential of Tyrosine-Histidine Bioinspired Assemblies. *Photosynth. Res.* **2022**, *151*, 185–193.

(293) Connelly, N. G.; Geiger, W. E. Chemical Redox Agents for Organometallic Chemistry. *Chem. Rev.* **1996**, *96* (2), 877–910.

(294) Corrsin, L.; Fax, B. J.; Lord, R. C. The Vibrational Spectra of Pyridine and Pyridine-d$_5$. *J. Chem. Phys.* **1953**, *21* (7), 1170–1176.

(295) Wong, K. N.; Colson, S. D. The FT-IR Spectra of Pyridine and Pyridine-d$_5$. *J. Mol. Spectrosc.* **1984**, *104* (1), 129–151.

(296) Partal Ureña, F.; Fernández Gómez, M.; López González, J. J.; Martínez Torres, E. A New Insight into the Vibrational Analysis of Pyridine. *Spectrochim. Acta A* **2003**, *59* (12), 2815–2839.

(297) Briois, V.; Fonda, E.; Belin, S.; Barthe, L.; La Fontaine, C.; Langlois, F.; Ribbens, M.; Villain, F. SAMBA: The 4-40 KeV X-Ray Absorption Spectroscopy Beamline at SOLEIL. *UVX 2010* **2011**, 41–47.

(298)   Newville, M. EXAFS Analysis Using *FEFF* and *FEFFIT*. *J. Synchrotron Radiat.* **2001**, *8* (2), 96–100.

(299)   Myers, J. A.; Lewis, K. L. M.; Tekavec, P. F.; Ogilvie, J. P. Two-Color Two-Dimensional Fourier Transform Electronic Spectroscopy with a Pulse-Shaper. *Opt. Express* **2008**, *16* (22), 17420–17428.

(300)   Zhang, Z.; Wells, K. L.; Hyland, E. W. J.; Tan, H.-S. Phase-Cycling Schemes for Pump-Probe Beam Geometry Two-Dimensional Electronic Spectroscopy. *Chem. Phys. Lett.* **2012**, *550*, 156–161.

(301)   Lewis, N. H. C.; Dong, H.; Oliver, T. A. A.; Fleming, G. R. Measuring Correlated Electronic and Vibrational Spectral Dynamics Using Line Shapes in Two-Dimensional Electronic-Vibrational Spectroscopy. *J. Chem. Phys.* **2015**, *142*, 174202.

* Each chapter is referenced separately. This bibliography serves as a complete list of all

references included in this dissertation

APPENDIX A

ACKNOWLEDGEMENTS FOR PERMISSION TO REPRODUCE PORTIONS OF

CHAPTER 1 FROM CHEMICAL REVIEWS AND ACS CATALYSIS

Reprinted with permission from: Reyes Cruz, E. A.; Nishiori, D.; Wadsworth, B. L.; Nguyen, N. P.; Hensleigh, L. K.; Khusnutdinova, D.; Beiler, A. M.; Moore, G. F. Molecular-Modified Photocathodes for Applications in Artificial Photosynthesis and Solar-Fuel Technologies. *Chem. Rev.*, **2022**, *122* (21), 16051–16109. Copyright 2022 American Chemical Society.

Reprinted with permission from: Khusnutdinova, D.; Wadsworth, B. L.; Flores, M.; Beiler, A. M.; Reyes Cruz, E. A.; Zenkov, Y.; Moore, G. F. Electrocatalytic Properties of

Binuclear Cu(II) Fused Porphyrins for Hydrogen Evolution. *ACS Catal.*, **2018**, *8* (10), 9888–9898. Copyright 2018 Ameican Chemical Society.

APPENDIX B

ACKNOWLEDGEMENTS FOR PERMISSION TO REPRODUCE PORTIONS OF

CHAPTER 2 FROM CHEMELECTROCHEM

APPENDIX C

ACKNOWLEDGEMENTS FOR PERMISSION TO REPRODUCE PORTIONS OF

CHAPTER 3 FROM THE J. PHYS. CHEM. LETTERS AND JOURNAL OF

AMERICAN CHEMICAL SOCIETY

Adapted from "Concerted Electron-Nuclear Motion in Proton-Coupled Electron Transfer-Driven Grotthuss-Type Proton Translocation" by Arsenault, E. A.; Guerra, W. D.; Shee, J.; Reyes Cruz, E. A.; Yoneda, Y.; Wadsworth, B. L.; Odella, E.; Urrutia, M. N.; Kodis, G.; Moore, G. F.; Head-Gordon, M.; Moore, A. L.; Moore, T. A.; and Fleming, G. R. Licensed under a Creative Commons Attribution-NonCommercial-NoDerivatives 4.0 International License.

Reprinted with permission from: Odella, E.; Secor, M.; Reyes Cruz, E. A.; Guerra, W. D.; Urrutia, M. N.; Liddell, P. A.; Moore, T. A.; Moore, G. F.; Hammes-Schiffer, S.; Moore, A. L. Managing the Redox Potential of PCET in Grotthuss-Type Proton Wires. *J. Am. Chem. Soc.*, **2022**, *144* (34): 15672–15679. Copyright 2022 American Chemical Society.